The Dissertation Committee for Charles Joseph Collins Certifies that this is the approved version of the following dissertation:

Aluminum Gallium Nitride-based Solar-blind Ultraviolet Photodetectors

Committee:

Joe C. Campbell, Supervisor

Russell D. Dupuis

Archie L. Holmes

Dean P. Neikirk

Paul S. Ho

Aluminum Gallium Nitride-based Solar-blind Ultraviolet Photodetectors

by

Charles Joseph Collins, M.S. E.E.

Dissertation

Presented to the Faculty of the Graduate School of
The University of Texas at Austin
in Partial Fulfillment
of the Requirements
for the Degree of

Doctor of Philosophy

The University of Texas at Austin
August 2002

Dedication

To my parents, Gary and Carol, and to my loving girlfriend Connie.

Acknowledgements

I would like to express my gratitude to my supervising, Professor Joe C. Campbell, for showing me the exciting world of nitride-based optoelectronic devices. His wise advice and constant support has been the most important aspect of my research, inspiring all of the work I have accomplished. Joe Campbell cares a great deal for his students, for which I have the up most respect for him. He is a great scientist and I am honored to have been able to work for him and know him as a mentor.

I would also like to express my sincere thanks to Professor Russell D. Dupuis, who has provided me with the exceptional nitride crystal growth that has made all this work possible. It has been an honor to work with one of the most respected MOCVD growers in the world.

I would like to thank my fellow group members including Bo Yang, Ariane Beck, Shuling Wang, Feng Ma, Xiaoguang Zheng, Drs. Geoff Kinsey, Ru Li, Jeremy Schaub, Clint Schow, Ping Yuan, Ting Li and John Carrano. They have all been good friends who were willing to lend a helping hand whenever I had a problem. I would like to specifically thank Dr. Geoff Kinsey for all of our interesting conversations, for being a great friend, and for making me a better person. Dr. Jeremy Schaub, for showing me how to work on our computers, for helping me with LabView programming, and for making the lab an interesting place to work. Bo Yang and Ariane Beck for all the hard work and collaboration on solar-blind photodetectors. Shuling Wang, for her kindness and device discussions. Dr. Ting Li, for all of the nitride detector knowledge he has passed on to me, for teaching me external quantum efficiency measurements, and for his constant support in all my research. Most of all I would like to thank Dr. John Carrano, who taught me how to process and test our nitride devices, who brought me up to speed very quickly when I first arrived, and who helped me transition from undergraduate studies to graduate research.

I want to thank Uttiya Chowdhury, Mike Wong, Tinggang Zhu, Richard Heller, Drs. Chris Eiting, Bryan Shelton, and Damien Lambert from the MOCVD group for supplying material and helpful discussions. I would especially like to thank Dr. Damien Lambert for helping me understand the growth issues and for helping me form a close working relationship with the growers. I would also like to thank Uttiya Chowdhury and Mike Wong for their hard work in getting better crystal growth that has allowed this work to be possible. I need also to thank Richard Heller for being a constant source of support and friendship, and Oleg Shchekin who has shown me through example how to be a better researcher and a great friend.

Finally, I must thank my wonderful parents, who have supported me in all of my academic accomplishments. I also owe a lot to my girlfriend Connie Brown who has made my life a better place and has helped me finish my degree.

Aluminum Gallium Nitride-based Ultraviolet Photodetectors

Publication No._____________

Charles Joseph Collins, Ph.D.
The University of Texas at Austin, 2002

Supervisor: Joe C. Campbell

High performance $Al_xGa_{1-x}N$-based ultraviolet photodetectors were designed, fabricated, characterized, and modeled for use in commercial and military solar-blind sensing applications. Chronologically, the first device structure studied was a heterojunction $Al_xGa_{1-x}N$/GaN *p-i-n* photodiode. These devices achieved record low dark current densities and record high external quantum efficiencies of ~77% with a semi-transparent recessed window device structure. Selective-area regrowth of $Al_{0.30}Ga_{0.70}N$ epitaxial layers on top of GaN template layers was used to reduce the tensile-strain-induced cracking and move toward solar-blind devices. The zero bias external quantum efficiency peak was shifted 50 nm toward solar-blind with ~ 20% at $\lambda = 315$ nm. Our group's first back-illuminated solar-blind photodetectors were achieved with zero bias external quantum efficiencies of ~ 12% at λ = 278 nm and a large detectivity of D^* = 5.3 $\times 10^{13}$ cm·Hz$^{1/2}$·W^{-1}. These devices had the same percentage aluminum in both the *n* and *i*-regions. A new device structure was used to investigate the advantage of using a "window" $Al_{0.50}Ga_{0.50}N$ *n*-region to increase the external quantum efficiency. With an $Al_{0.41}Ga_{0.59}N$ absorption region, solar-blind photodetectors were fabricated with high zero-bias external quantum efficiencies of 26% at λ = 279 nm. Although the external quantum efficiency of the solar-blind detector was improved, the detectivity decreased to D^* = 5.30$\times 10^{12}$ cm·Hz$^{1/2}$·W^{-1} at λ = 279 nm. This was attributed to the large leakage current, which caused a significant decrease in the differential resistance. Finally, two improved solar-blind detectors were fabricated with an innovative $Al_{0.60}Ga_{0.40}N$ *n*-region. We report a zero bias external quantum efficiency of ~ 42% at λ = 269 nm for an $Al_{0.48}Ga_{0.52}N$ *i*-region device. By slightly increasing the aluminum percentage in the *i*-region, the zero bias external quantum efficiency was increased to ~ 53% at λ = 275 nm for an $Al_{0.45}Ga_{0.55}N$ *i*-region device. The low leakage currents of these devices leads to large differential resistances, which when combined with the high external quantum efficiency at zero bias, gives solar-blind detectivities of D^* = 1.9$\times 10^{14}$ cm-Hz$^{1/2}$-W^{-1} at λ = 269 nm and D^* = 3.2$\times 10^{14}$ cm-Hz$^{1/2}$-W^{-1} at λ = 275 nm for the $Al_{0.48}Ga_{0.52}N$ and $Al_{0.45}Ga_{0.55}N$ *i*-region devices, respectively.

Table of Contents

List of Tables

List of Figures

1. Introduction

1.1 SOLAR-BLIND SPECTRUM

The portion of the electromagnetic spectrum detected by the human eye is known as the visible spectrum, with wavelengths from λ = 400 to 900 nm. Numerous applications such as fiber optic transmission and imaging with focal plane arrays utilize the infrared spectrum, λ = 900 nm to 100 μm, is commonly used for 1.3 μm and 1.5 μm lasers in fiber communication systems. The much less known portion of the spectrum is the ultraviolet spectrum from λ = 100 to 400 nm. The sun emits most of the ultraviolet radiation that we encounter, although there are other sources such as welding arcs, some lamps, and power line discharges. The UV portion of the solar spectrum is less than 10% of the total energy output of the sun, but these wavelengths are believed to be a factor in skin cancer and thus have become a topic of concern as researchers find increasing ozone depletion.

The ultraviolet spectrum can be subdivided into three basic categories (Figure 1.1):

UVA (320-400 nm) is affected little by ozone and is needed by humans for the synthesis of vitamin-D. Wavelengths from 345 to 400 nm are used in blacklights, which cause fluorescent objects to glow. Shorter UVA wavelengths from 320 to 345 nm can contribute to tanning, skin aging, eye damage, and immune suppression [1,2].

UVB (280-320 nm) is strongly affected by ozone levels. Decreases in stratospheric ozone mean that more UVB radiation can reach the earth's surface, causing sunburns and an increase in a variety of skin problems including skin cancer and premature aging.

UVC (100-280 nm) is strongly scattered and absorbed by atmospheric oxygen, nitrogen and ozone, so that almost no UVC radiation reaches the earth's surface. Wavelengths in the 200 to 280 nm range are especially damaging to exposed cells and thus used for killing germs. Wavelengths below 200 nm are called "vacuum ultraviolet" since they are absorbed by air.

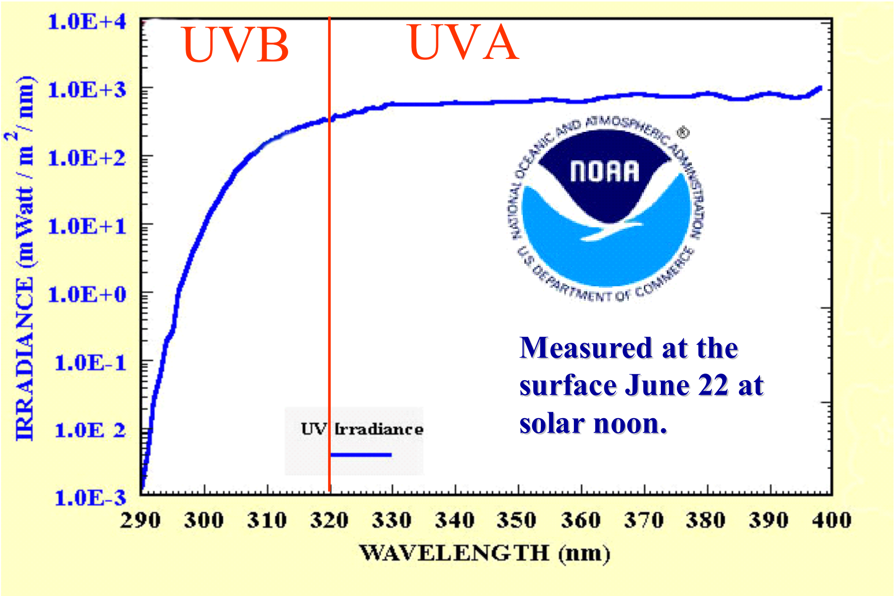

Measured at the surface June 22 at solar noon.

Figure 1.1: Irradiance of earth surface with ultraviolet light from the sun. The short wavelength drop is due to atmospheric absorption and reflection.

As can be seen in Figure 1.1, UVA light is almost completely transmitted by the atmosphere. In the UVB region the irradiance at the earth's surface drops off by over five orders of magnitude due to atmospheric absorption and reflection. Thus, in the UVC region of the ultraviolet spectrum almost no light from the sun reaches the earth's surface. The UVC region is also know as the "solar-blind" region because photodetectors working in this wavelength range can not see the sun. This allows for detection of other objects that emit ultraviolet radiation since the background radiation level is so low.

1.2 ULTRAVIOLET LIGHT DETECTION

Development of the $In_xAl_yGa_{1-x-y}N$ wide-band gap semiconductor system has led to the commercialization of bright blue, green, and white light-emitting diodes as well as blue laser diodes for display and data storage applications [3-5]. The advantages of this material system include chemical stability, high-temperature operation, wide-band gap, and high breakdown fields [6]. The desire for shorter-wavelength devices has drawn attention to $Al_xGa_{1-x}N$ devices, which absorb and emit in the ultraviolet spectrum. In particular, recent research has concentrated on the growth of $Al_xGa_{1-x}N$ layers for fabrication of ultraviolet photodetectors. These photodetectors have potential applications in chemical sensing, flame detection, ozone-hole sensing, short-range communication, and biological agent detection [7-9]. Targets of military interest emit ultraviolet radiation from either the plume of missiles or aircraft engines, or the bow shockwave of hypervelocity missiles. These ultraviolet emissions are usually very weak. Detectors that work in the solar-blind (UVC) region of the spectrum, sensitive to wavelengths < 280 nm, are "blind" to the sunlight reaching the earth's surface, giving them very low background radiation and the best potential to detect the weak ultraviolet signals [10, 11].

Photomultiplier tubes are the current mainstream technology for ultraviolet radiation detection. These photodetectors are capable of achieving large internal gains (> 10^7), high responsivities (> 600 A/W), and very low dark currents (<0.1 fA). However, photomultiplier tubes are bulky, require high voltages, and can easily be broken. In addition, they are not intrinsically solar-blind, requiring expensive external filters with associated insertion loss. However, photomultiplier tubes have very large gains, which allow for detection of very small signals.

The other common alternative for ultraviolet radiation detection is an ultraviolet enhanced silicon photodiode. These detectors are easily made with current silicon technology, are small and relatively sturdier than photomultiplier tubes, and have low operating voltages. Unfortunately, due to the small band-gap of Si, these photodetectors have relatively high currents, which lead to low detectivities, and require the same expensive external filters for solar-blind response.

The $Al_xGa_{1-x}N$ material system is well suited as a photodetector material in the ultraviolet spectrum because of its large direct band-gap energy (200 to 365 nm). The large band-gap provides low thermally generated dark current and good radiation hardness. Furthermore, its hardness, chemical stability, and high melting temperature make it suitable for a variety of harsh environments. In particular, the military is interested in imaging systems that can be fabricated by flip-chip mounting back-illuminated $Al_xGa_{1-x}N$ detector arrays to silicon readout circuitry. These systems need to be compact, rugged, and operate at low voltages. Therefore, the $Al_xGa_{1-x}N$ system can provide an attractive solid-state alternative to both photomultiplier tubes and silicon photodiodes.

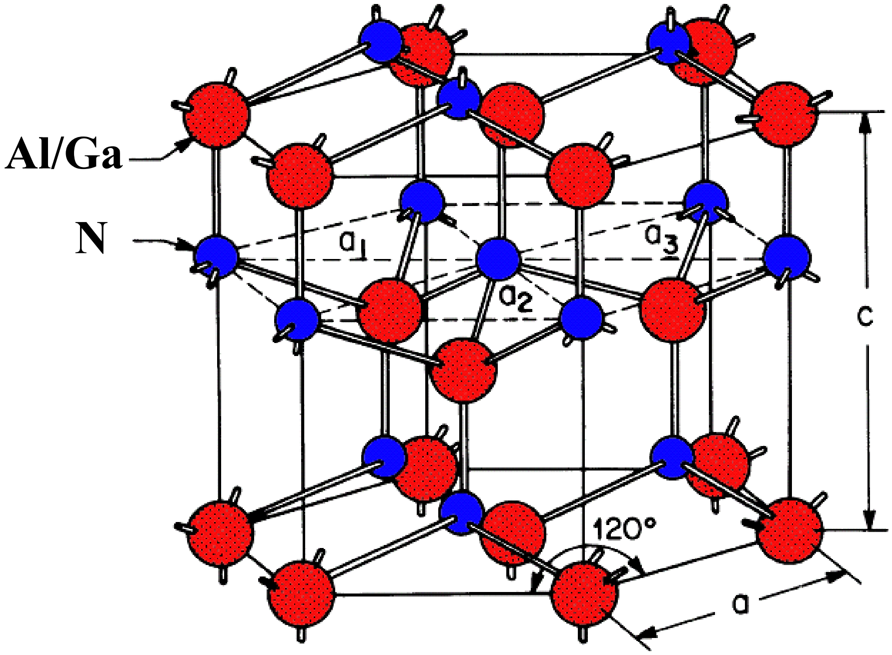

Figure 1.2: Representation of the wurtzite structure for $Al_xGa_{1-x}N$.

1.3 III-NITRIDE MATERIAL PROPERTIES

Group III-nitride semiconductors exist in both cubic (zinc blend) and hexagonal (wurtzite) crystalline forms. However, the wurtzite phase dominates at low pressures and is the phase used for our research efforts. The III-nitride wurtzite structure has a hexagonal unit cell with two lattice constants, *a* and *c*.

The unit cell contains six nitrogen atoms and six atoms from column III of the periodic table. As shown in Figure 1.2, the wurtzite structure consists of two interpenetrating hexagonal close-packed sublattices (one nitrogen and the other column III) offset along the *c*-axis by 3/8 of the cell height. Figure 1.2 shows the nitrogen face up (Ga atoms on the bottom), although growth is usually performed on the gallium face, which affects the crystal quality and subsequent device contacts. When discussing alloy-induced strain in this material system, the relevant parameter is the *a*-lattice constant. Figure 1.3 shows the band-gap energy versus the *a*-lattice constant for the $In_xAl_yGa_{1-x-y}N$ system. The $Al_xGa_{1-x}N$ line (between GaN and AlN) represents the ternary compound used for this research and the blue shaded area represents the solar-blind alloys.

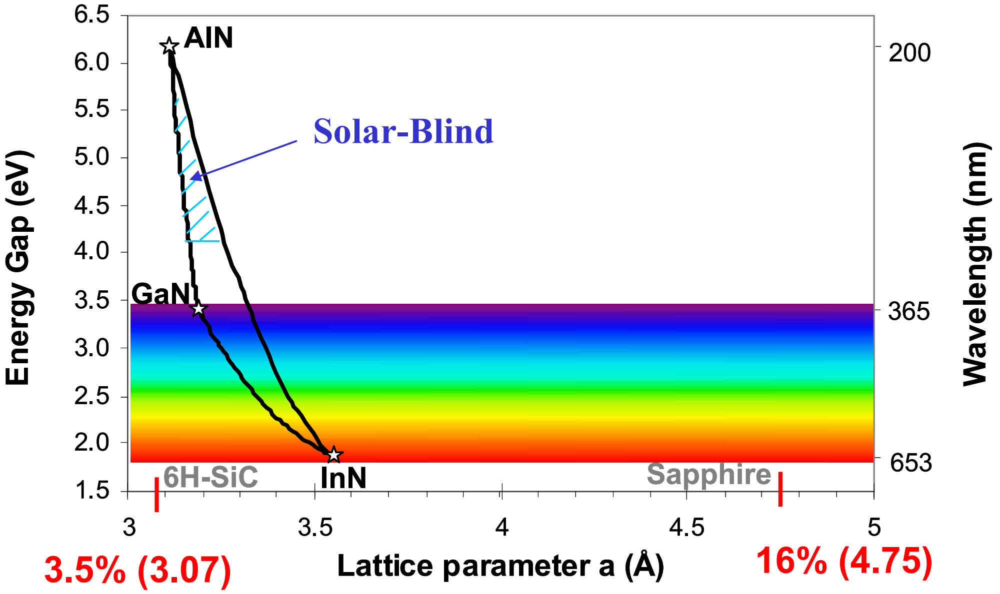

Figure 1.3: Bandgap versus *a*-lattice constant for the $In_xAl_yGa_{1-x-y}N$ system.

There are two main substrates of choice for growth of $Al_xGa_{1-x}N$, SiC (6H-SiC) and sapphire (Al_2O_3). The lattice constants of these substrates are shown in Figure 1.3. Both substrates are lattice mismatched, however, as discussed in Section 2.1, good material can still be grown on both. With the recent introduction of bulk substrates, it is hopeful that soon lattice matched substrates will provide reduced defect densities.

The parameters shown in Table 1.1 will be used in subsequent discussions of the $Al_xGa_{1-x}N$ devices. As mentioned above, the *a*-lattice parameter is needed for strain calculations, leading to a critical thickness discussed in Section 4.1. Most of the electrical and optical properties of a direct band-gap semiconductor derive from the energy gap (E_g) and the electron affinity (χ) of the material. In addition, the absorption coefficient (α) of different layers is very important for photodetector design. These parameters are used in Sections 6.5 to fit external quantum efficiency measurements.

	***a*(Å)**	**E_g @ 300K (eV)**	**λ @ 300K (nm)**	**χ (eV)**	**α (10^5 cm^{-1})**
GaN	3.19 [12]	3.40 [14]	365	3.3 [16]	8.03 [17]
AlN	3.11 [13]	6.20 [15]	200	-1.6 [16]	19.2 [18]

Table 1.1: Material parameters: *a*-lattice constant, room temperature bandgap (E_g), corresponding wavelength (λ), electron affinity (χ), and absorption coefficient (α) for GaN and AlN.

1.4 PHOTODETECTOR BACKGROUND AND DISSERTATION ORGANIZATION

The photoconductor was the first device structure used for $Al_xGa_{1-x}N$-based ultraviolet photodetectors [19-24]. These detectors can achieve high responsivities from their large photoconductive gain, but they suffer from slow speed response because of the photoconductive gain mechanism. Schottky-junction photodetectors [25-32] and back-to-back Schottky metal-semiconductor-metal (MSM) photodetectors [33-40] were developed on GaN and $Al_xGa_{1-x}N$ to achieve low dark currents (better signal to noise ratios) and faster speed response.

As material quality and doping improved, both *p-n* and *p-i-n* junction photodiodes [41-52] have been fabricated to achieve low dark current, low temperature-dependent degradation, fast speed response, and high detectivity. GaN and $Al_xGa_{1-x}N$ *p-i-n* photodiode arrays have also been fabricated to demonstrate device uniformity and for two-dimensional focal plane array applications [53, 54]. GaN avalanche photodiodes (APDs) have also been examined for their high sensitivity due to large impact ionization gain [55-58]. Section 3.1 shows the gain curve of one of the few GaN APDs that have been fabricate.

This dissertation is organized in chronological order, following the move from top-illuminated GaN *p-i-n* photodiodes to back-illuminated solar-blind *p-i-n* photodiodes. To achieve solar-blind photodiodes, the peak external quantum efficiency wavelength must be shifted from 365 nm (GaN) to 280 nm (solar-blind). For back-illumination, GaN template layers must be replaced by $Al_xGa_{1-x}N$ template layers with sufficient aluminum concentration to allow good transmission of desired wavelengths. Chapter 2 is a basic overview of material growth, processing, and device characterization. Chapters 3 and 4 discuss the peak external quantum efficiency for GaN devices, and the evolution toward a solar-blind response. The first back-illuminated solar-blind photodiodes are examined in Chapter 5. Improvements in external quantum efficiency and detectivity are shown in Chapters 6 and 7. Device characterization and simulation techniques are discussed in the chapters with the devices for which they were initially developed.

2. Growth, Processing, and Characterization

2.1 INTRODUCTION

Growth of Group III-nitride semiconductors has gained a lot of attention in the past decade for use in optoelectronic and power devices [3-11]. Devices have been fabricated despite the high defect densities associated with nitride material. Typically, semiconductors are grown on lattice matched substrates to minimize defects caused by lattice relaxation during crystal growth. Unfortunately, GaN and AlN substrates have not been available until recently due to problems with bulk cystal growth. Instead, the two substrates of choice have been basal-plane (c-plane) sapphire (Al_2O_3) and 6H-SiC. Both have hexagonal lattice structures and are stable at the high temperatures of MOCVD growth. As seen in Figure 1.3, the lattice mismatch between 6H-SiC and GaN is only 3.6% while that of sapphire is 16%. In addition, as seen in Table 2.1, the thermal expansion coefficients of 6H-SiC, AlN, and GaN are very close. Thus, growth on

	6H-SiC	**Al_2O_3**
Lattice Parameter, a (Å)	3.03	4.75
Thermal Expansion (10^{-6}/K)	4.9	0.5
Band Gap (ev)	3.03	7.30*
Substrate Cost ($)	~1000	~100

Table 2.1: Comparison of III-nitride growth substrates 6H-SiC and sapphire (Al_2O_3). * Estimated from transmission data.

6H-SiC should produce fewer dislocations due to relaxation, but 6H-SiC is significantly more expensive than sapphire. In addition, 6H-SiC is not transparent to solar-blind wavelengths and thus can not be used for back-illuminated solar-blind photodetectors. Sapphire, on the other hand, is transparent to wavelengths above 200nm, and is significantly cheaper than 6H-SiC. As a result of these characteristics, sapphire has been the substrate of choice for our device work. When growing back-illuminated devices it is necessary to buy substrates that are double-polished (polished on both sides). It should be noted that the quality of the sapphire surface polish will greatly affect the subsequent epitaxy quality.

2.2 MATERIAL GROWTH

Although films have been grown using molecular beam epitaxy (MBE), metal organic chemical vapor deposition (MOCVD) has emerged as the primary method for deposition of III-nitride semiconductors. The III-nitride material described in this work has been grown by low-pressure MOCVD in an EMCORE model D125 UTM rotating disk reactor. The MOCVD process involves the complex reaction of different gas precursors in a reaction chamber. The gases are locally brought to high temperatures (500-1100°C) in the chamber and react on the substrate to form the desired crystal along with volatile gas-phase byproducts. The column-III precursors used in this research are trimethylgallium (TMG), trimethylaluminum (TMA), and trimethylindium (TMI), while ammonia is used for the nitrogen source. The trimethyl precursors are commercially available in stainless-steel vessels (bubblers) that are mounted on the MOCVD reactor.

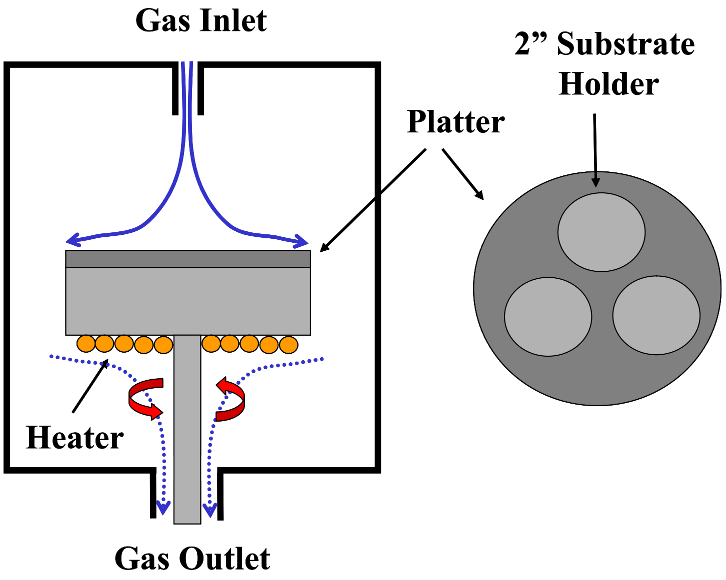

Figure 2.1: Schematic of UT-MOCVD chamber with multi-wafer platter. Platter holds three 2” substrates.

A carrier gas, in this case hydrogen, is bubbled though the source and carries the metalorganic precursors to the reaction chamber. The ammonia is kept in a separate high-pressure gas cylinder. Reaction occurs on platters that are designed to hold three 2-inch diameter wafers in pockets positioned symmetrically around the center. The platter can spin at high rotation rates (~1000 rpm) to help insure uniform crystal growth and is heated to growth temperature by two resistance heaters located directly under the platter. The variation in the growth occurs from the inner to the outer regions of the platter.

Growth begins with a low temperature AlN or GaN buffer layer that is grown directly on the sapphire substrate. This quasi-crystalline buffer layer, consisting of many three-dimensional growth islands, is grown to help eliminate the strain due to the large lattice mismatch between the material and the sapphire substrate. As the growth proceeds, the islands become bigger and coalesce, forming threading dislocations at the interface. On top of the buffer layer a thick, ~500-700 nm, GaN or $Al_xGa_{1-x}N$ template layer is grown to help reduce defects and as a fully relaxed bulk layer for device growth. Device layers are then grown as needed.

During growth of $Al_xGa_{1-x}N$ layers native defects and nitrogen vacancies are responsible for a high background free-electron concentration. Thus, even when no dopants are used, as-grown GaN is slightly *n*-type with a typical free-electron concentration of 5×10^{16} cm^{-3}. *N*-type doping is easily achieved by the incorporation of silicon during the epitaxial growth. The silicon precursor used is silane (SiH_4) and the Si dopants incorporate onto Ga sites and become electron donors. Diffusion of Si dopants during subsequent epitaxial growth is minimal due to their large size. Figure 2.2 shows the relative levels of possible dopants in GaN. For GaN the activation energy of Si is relatively small, 17 meV, and thus high *n*-type doping at room temperature is easily achieved. As aluminum is added, the Si level continues to get deeper and near the composition, $Al_{0.50}Ga_{0.50}N$, it is approximately 120 meV [59]. At this point it becomes difficult to dope *n*-type. This doping problem can not be explained by the increase of the Si level alone. It is discussed further in Chapter 7.

P-type doping of GaN is harder to achieve. Bis(cyclopentadienyl)-magnesium is used as the precursor for magnesium doping. The Mg atoms are incorporated onto Ga sites and become electron acceptors as seen in Figure 2.2. However, Mg acceptors are not easily ionized because of their relatively large activation energies of approximately 160 meV in GaN [60]. This level gets deeper by ~3.2 meV for each 1% increase of the Al content in the alloy [59]. Near $Al_{0.40}Ga_{0.60}N$, the activation energy is approximately 336 meV. As a consequence, at room temperature not enough of the dopants are activated to make the layer *p*-type. Also, due to the hydrogen-rich atmosphere, Mg atoms tend to form Mg-H neutral complexes during epitaxial growth. As a result, the as-grown GaN:Mg films turn out to be very resistive. To remove the hydrogen and activate the Mg dopant, a rapid thermal activation anneal is performed in an N_2 ambient [61]. This anneal breaks the Mg-H bonds that prevent the Mg atoms from behaving like acceptors, and promotes hydrogen diffusion from the crystal. Even after activation, only ~1% of the Mg dopants in GaN are activated at room temperature. Thus, for GaN Mg doping levels are in the $\sim 10^{20}$ cm^{-3} range in order to achieve low $\sim 10^{18}$ cm^{-3} activated dopants. Since the Mg level gets deeper as

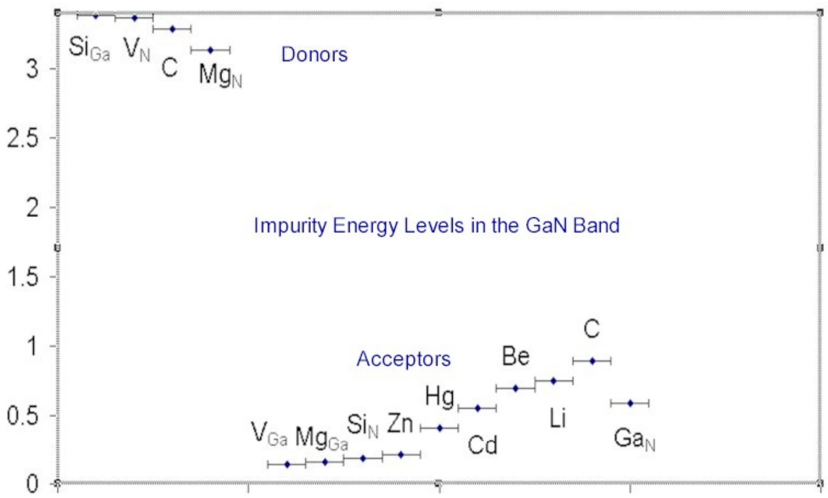

Figure 2.2: Dopant levels in GaN [54]

we increase the aluminum percentage, the percentage that is activated decreases from ~1% for GaN down to ~0.007% for $Al_{0.40}Ga_{0.60}N$.

2.3 DEVICE FABRICATION

Upon removal from the growth chamber the 2-inch sapphire substrates with the epitaxial layers are cleaved into four equal quarters. The quarters are labeled Q1, Q2, Q3, and Q4, with Q1 and Q2 being the inner quarters and Q3 and Q4 the outer. As mentioned earlier in this section, the variation in growth occurs from the inner to the outer of the wafer. We observe spatial variation in device performance, especially if the composition variation is large, depending on which part of the wafer is selected for processing. Usually the first quarter processed is Q2, which is cleaved into smaller samples for device fabrication. The samples are identified by a number such as M2510Q2-1; where M2510 identifies the growth run, Q2 identifies the quarter, and -1 identifies the piece processed (-2 would be the second piece processed).

Processing begins by cleaning the sample. It is first placed in a beaker of acetone in an ultrasonic bath for two minutes. It is then rinsed using a standard clean consisting of an acetone flush, an isopropal alchohol flush, and deionized (DI) water rinse. The sample is then blown dry and placed in a furnace at 150°C for 2 minutes to bake off any remaining water. Then AZ 5214 photoresist is spun at two thousand r.p.m. for 40 sec. and soft-baked at 90°C for 10 minutes to remove any bubbles and to set the photoresist in order to eliminate any sticking to the photomask. The sample is then placed on the mask aligner and, using the photomask "mesa" layer, is exposed for 1.2 minutes. Developing in AZ 425 developer for 45 seconds reveals the mesa pattern. After inspection to insure adequate development time, the samples are placed in anoven at 120°C for one hour to hard-bake the photoresist, preparing it for mesa etching.

AlGaN is very difficult to etch, and no standard chemical etch has a fast enough etch rate to be appropriate for mesa definition. This material requires a physical/chemical etch in a plasma etching system. Reactive ion etching (RIE) consists of flowing reactive gases into a chamber between an anode plate and acathode plate. Between the plates an RF power supply excites a capacitively-coupled plasma. This plasma consists of ions and reactive byproducts. The sample is placed on the anode and a DC bias is applied across the plates to accelerate ions toward the sample. These ions physically etch the sample while the plasma byproducts chemically etch the sample. For RIE etching of AlGaN a mixture of boron trichloride (BCl_3) and silicon tetrachloride ($SiCl_4$) is used. The different sized B and Si ions ensure a smoother physical etch while Cl_2 byproducts are used as the chemical etch. Etch recipes vary for desired etch rates, but the most common etch used in this work consists of flowing 8 sccm of BCl_3 and 8 sccm of $SiCl_4$ at a chamber pressure of 40 mTorr. The plasma is then arced using an RF power of 100 W to produce an etch rate of ~ 140 Å/min.

The patterned samples are etched in the RIE for the appropriate amount of time to etch into the *n*-region of the *p-i-n*. They are then removed and the remaining photoresist is stripped off using acetone. The sample is then placed in a rapid thermal annealer (RTA) at 850°C for 10 min. to active the Mg dopants by driving out hydrogen [62,63]. This anneal is performed after the mesa etch so that it can also be used to “heal” RIE etch damage on the sidewalls of the mesas that can be a source of leakage current. The samples are then cleaned in ammonia hydroxide to remove any RIE byproducts that are left on the sidewalls which are another source of leakage current. A plasma enhanced chemical vapor deposition system (PECVD) is then used to deposit silicon dioxide (SiO_2) on the samples as a passivation layer. The PECVD uses silane (SiH_4) and nitrour oxide (N_2O) gases to arc a plasma and deposit SiO_2. After SiO_2 deposition, a standard clean is used and photoresist is spun at four thousand r.p.m. for 40 sec. This higher spin rate results in a thinner photoresit that is suitable for contact metal lift-off. After soft-baking at 90°C for ten minutes and exposing for 40 seconds using the “*n*-metal” mask, the samples are developed for 30 seconds. Then they are dipped in buffer oxide etchant (BOE) for 55 seconds to remove the SiO_2 for metal deposition by e-beam evaporation. After metal deposition the samples are rinsed in acetone to lift off the unwanted metal and leave the desired contact. The *n*-contact is then annealed at 850°C for 30 sec. This process is then repeated with the “*p*-metal” mask. After lift-off the samples are ready to be removed from the clean-room for device characterization.

2.4 OHMIC CONTACTS

Forming good ohmic contacts is crucial in device fabrication. Making ohmic contact to *n*-type GaN and AlGaN has been investigated by many groups [64-67]. It has been found that a multi-metal contact gives the lowest contact resistance. Some common *n*-contacts are Ti/Al, Ti/Al/Ti/Au, Ti/Al/Pt/Au, and more recently, Ti/Al/Mo/Au. In this work we use Ti/Al/Ti/Au for the *n*-contact.

Annealing the *n*-contact at 850°C for 30 seconds gives the lowest contact resistance. It should be noted that the *n*-contact is annealed before *p*-contact deposition. Devices that were annealed at 850°C after *p*-contact deposition were "shorts" due to the *p*-contact diffusing across the *p-i-n* junction.

P-contacts are much harder to form on GaN and they are especially difficult for AlGaN. Due to the large bang-gap of $Al_xGa_{1-x}N$, the contact metal must have as large a work function as possible. Ni (5.15 eV) and Pd (5.12 eV) are two of the best choices. In this work we have used both Ni/Au and Pd/Au contacts [68-73]. The Ni/Au contacts are annealed at 675°C for two minutes to lower the contact resistance. The Pd/Au contacts are not annealed. It can be seen from contact resistance measurements, that even our best *p*-contacts are not completely ohmic, but show a Schottky-like characteristic.

2.5 DEVICE CHARACTERIZATION

In order to determine the contact resistance (R_C) of a particular contact scheme, and the series resistance (R_S) of the epitaxial layer, we utilize a transmission line model (TLM) [74]. Square metal contacts are deposited with increasing separation (l) onto an isolated strip of material (Figure 2.3). The resistance from one square to the next (R_T) is extracted from a current-voltage curve. The R_T values are then plotted vs. the contact separation and fit using a linear curve fit (Figure 2.4). The gradient of this curve fit is equal to R_S divided by the contact width (W), while the y-intercept is equal to $2R_C$. Extrapolation of the linear fit to the x-intercept, shown by the red line in Figure 2.4, yields the transfer length (L_T). From L_T and R_S the specific contact resistance (ρ_c) can be calculated using Equation 2.1.

$$L_T = \sqrt{\rho_c / R_S} \qquad 2.1$$

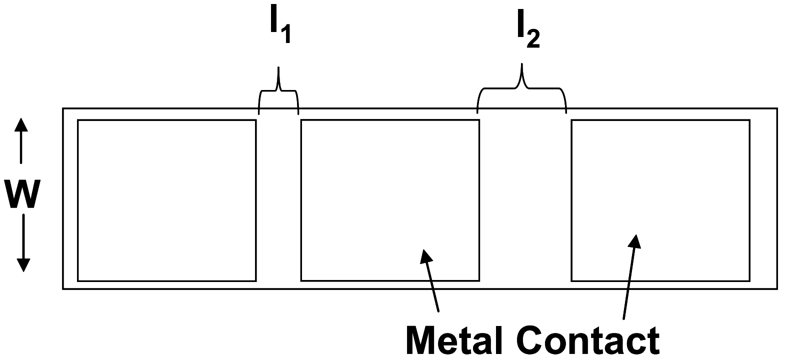

Figure 2.3: Schematic diagram of the contact scheme for the transmission line model

Current-voltage (I-V) curves with no illumination (dark current) and illuminated by a broad-band UV light source are obtained using a HP 4145B parameter analyzer. For back-illuminated devices the light is incident through the sapphire substrate. It is desirable to have as low a dark current as possible and still have a strong forward turn-on. Devices that are very resistive may show low dark currents, but they also have poor forward I-V curves. It has been a challenge, as we increase the Al percentage, to keep the $Al_xGa_{1-x}N$ conducting due to the doping problems discussed earlier. Diodes with high leakage currents are a sign of either poor processing or poor material quality. The ideality factor,

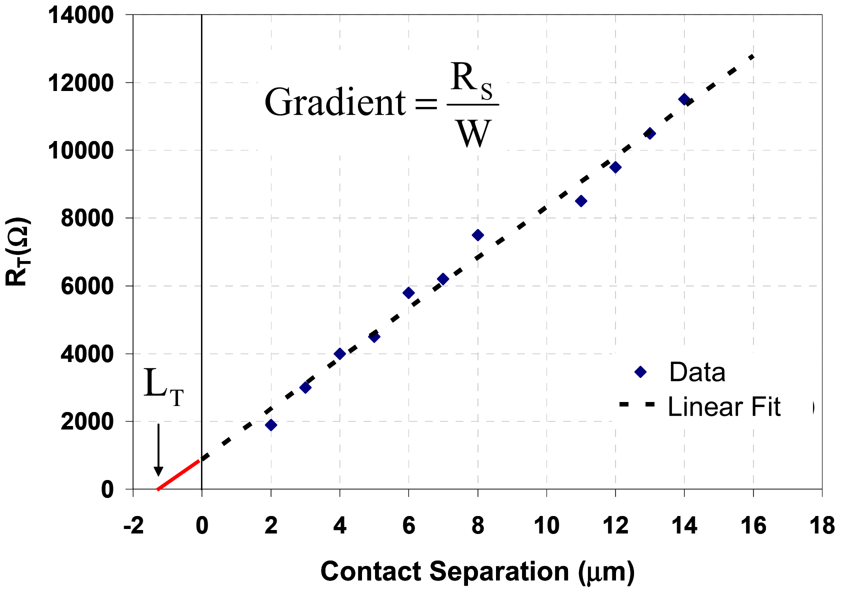

Figure 2.4: Experimental data for Ni/Au to *p*-GaN annealed at 675°C for two minutes. Linear fit is used to extrapolate R_S, R_C, L_T, and ρ_c.

n, of a diode can be determined by fitting the low-level injection regime of the forward current. In general this number is between 1 and 2 and is an indication of how close the device is to an "ideal" diode. For AlGaN devices this number is usually larger than 2; it depends, to a great extent, on the *p*-contact quality. Fitting the high-level injection region of the forward I-V allows one to extract the series resistance (R_S) of the device. This procedure is discussed in depth in Section 3.4.

The external quantum efficiency (EQE) is measured versus the wavelength of incident light. A 1 kW Xenon lamp is used as the optical source.

The broad-band UV emission of the lamp is coupled into a Spex 1/8 meter monochromator with the output slits set to a narrow band-pass. A portion of the light output is focused on a UV-grade fiber using a 10x UV-objective. The output of the fiber is collimated with a UV-objective. After passing through a chopper, the UV signal is focused with a 20x objective onto the sample. A lock-in amplifier is used, with the chopping reference, for low-noise current measurements. The incident optical power is normalized as a function of wavelength using a calibrated UV-enhanced silicon photodetector. Often the external quantum efficiency is converted to responsivity using:

$$R_{\lambda} = \frac{\eta_e \lambda(nm)}{1240} \tag{2.2}$$

where η_e is the external quantum efficiency at the wavelength λ in nanometers. This responsivity is frequently plotted on a semi-log plot in order to reveal the degree of below band-gap rejection. This drop is important because of the rise, by six orders of magnitude, in background radiation from 280-320 nm (as discussed in Chapter 1).

2.6 SUMMARY

This chapter serves as an overview of the problems and challenges that are encountered while growing, processing, and testing AlGaN photodetectors. It is important to understand these problems so that one can intelligently design photodetectors in this material system. The following chapters will discuss improvements in device design, growth, and processing.

3. Top-Illuminated $Al_xGa_{1-x}N$/GaN *p-i-n* Photodetectors

3.1 INTRODUCTION

GaN is well suited as the absorption region for ultraviolet (UV) photodetectors. As mentioned in Chapter 1, these devices are useful for missile tracking and intercept, biological agent detection, covert communications and flame detection. GaN device work at the University of Texas started with former group members Dr. John Carrano and Dr. Ting Li. Initially metal-semiconductor-metal (MSM) devices were fabricated and showed low dark currents of ~30 nA/cm^2 and external quantum efficiencies of ~50% at -10 V [35-37, 39]. These devices also showed high-speed operation with a bandwidth of ~15 GHz [36].

To achieve lower dark currents and high zero bias external quantum efficiency, GaN homojunction *p-i-n* photodetectors were investigated. Osinsky et. al.[45] and W. Yang et. al. [52] reported GaN *p-i-n* photodetectors with low dark current densities of ~ 25 nA/cm^2 and ~ 5 nA/cm^2, respectively, at 5 V reverse bias. Dr. Carrano and Dr. Li demonstrated GaN *p-i-n* photodetectors with low dark current densities of ~ 3 nA/cm^2 at 5 V reverse bias [38]. Some of my initial work was with Dr. Carrano on fabricating avalanche photodiodes from low dark current material [56,57]. We had only limited success due to the large defect density inherent to GaN growth on sapphire substrates. To “find” an APD hundreds of small diameter (~ 25 µm) devices were fabricated and tested to find one short-lived device. Figure 3.1 shows the IV characteristics for a GaN APD and its gain curve.

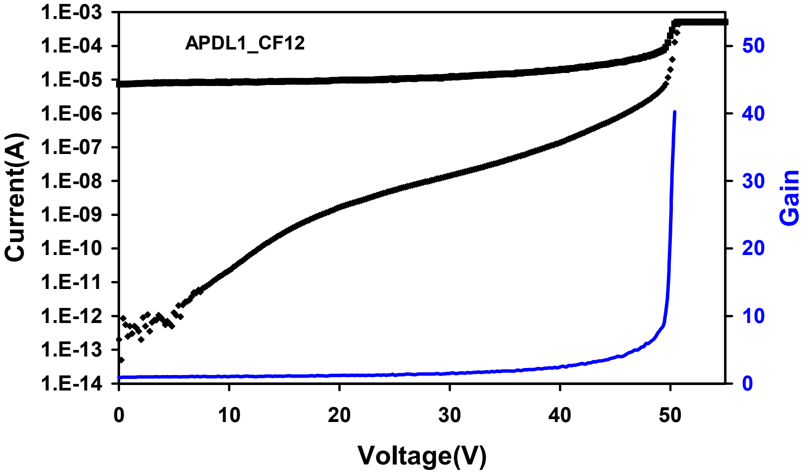

Figure 3.1: I-V characteristics of a GaN APD with gain curve.

Limiting the dark current of a device is only beneficial if the device also exhibits large zero bias external quantum efficiency. Osinsky et. al.[45] reported homojunction GaN *p-i-n* photodetectors with zero bias external quantum efficiencies of ~ 35%. Dr. Carrano and Dr. Li also demonstrated homojunction GaN *p-i-n* photodiodes with zero bias external quantum efficiencies of ~30% [42]. These photodiodes had 200 nm-thick *p*-regions and were top-illuminated devices. GaN has a high absorption coefficient of > 10^5 cm^{-1} [75], and thus the majority of the incident radiation is absorbed in the *p*-region. In addition, the diffusion length of GaN, ~0.1 μm, is short relative to the *p*-region thickness. This results in the loss of the majority of the incident light to recombination. To avoid these problems, the incident light must pass to within a depletion length of the high-field *i*-region before it is absorbed. Dr. Li used a recessed window structure

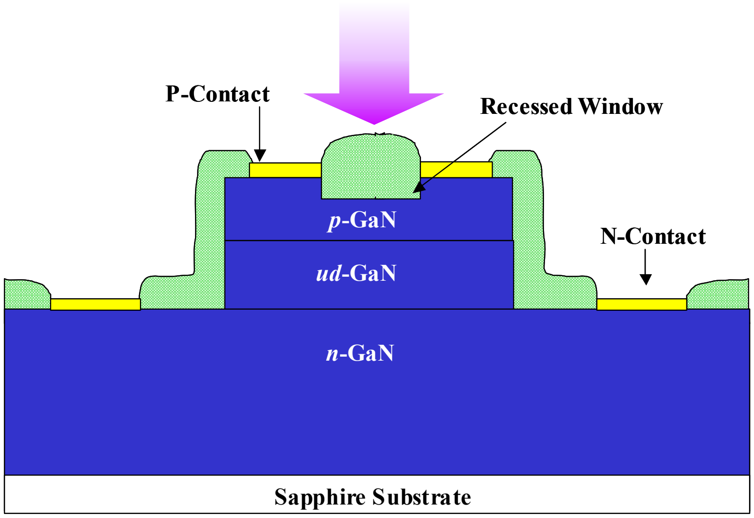

Figure 3.2: Schematic cross section of a GaN homojunction *p-i-n* with a recessed window structure.

to thin the *p*-region in the middle of the ring contact, thus decreasing the length between the absorption region and the depletion region (Figure 3.2). It was found that this increased the external quantum efficiency from ~30% to ~ 60% at 360 nm as seen in Figure 3.3. Although the external quantum efficiency was improved, these devices still suffered from an optical “dead space” existing near the *p*-GaN surface. It has been suggested by Ting et. al.[49] that this “dead space” is caused by both a Schottky-like *p*-contact, and native surface contamination (carbon and oxygen), creating band bending near the surface which induces an internal electric field of opposite polarity to the applied bias. It has been estimated that within the first ~0.14 µm of *p*-GaN almost all of the photoexcited electrons are lost to recombination [49]. To avoid this surface

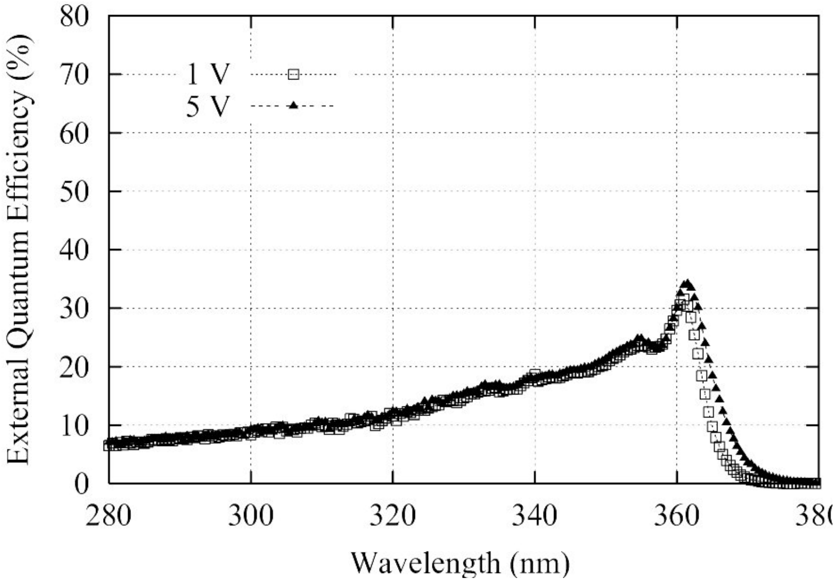

(a)

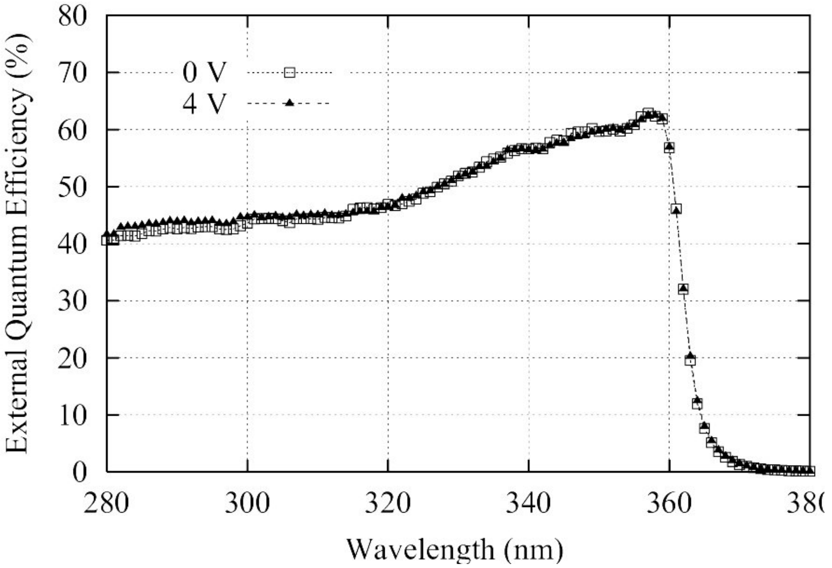

(b)

Figure 3.3: External quantum efficiency for GaN homojunction *p-i-n* photodiodes,(a) no recessed window, (b) 0.14 μm recessed window.

related problem, and further increase the external quantum efficiency, a new design was needed to avoid absorption near the surface of the *p*-GaN.

3.2 RECESSED WINDOW $AL_XGA_{1-X}N$/GAN *P-I-N* PHOTODIODE

As the growth of low aluminum percentage *p*-$Al_xGa_{1-x}N$ epitaxial layers matured, attempts were made to incorporate them into our device design. To eliminate the effect of the optical "dead space", and absorb light with-in a diffusion length of the *i*-region, a *p*-$Al_{0.13}Ga_{0.87}N$ "window" layer was used in the design of our photodiodes. By performing transmission line measurement contact studies of Ni/Au contacts on *p*-$Al_{0.13}Ga_{0.87}N$ we found that the contacts were Schottky-like. To improve the contact, a *p*-GaN cap-layer was grown on top of the *p*-$Al_{0.13}Ga_{0.87}N$ "window" layer. Most of the light absorbed in the *p*-GaN cap-layer would be lost to the optical "dead space", and thus a recessed window was used to etch through this cap-layer and reveal the window *p*-layer.

The *p*-$Al_{0.13}Ga_{0.87}N$ layer was found to be very resistive, which lead to crowding of the electric field underneath the ring *p*-contact and a spatial non-uniformity of the photoresponse. This can be seen in the two raster scans shown in Figure 3.4. The raster scan setup consisted of an argon laser at λ= 351 and 363 nm focused down to a ~5 μm spot diameter. This diameter was the limiting factor in the spatial resolution. A Newport MM3000 motion controller was used with two Newport 850G DC actuators to replace the manual motion control of then x-y translation stage that held the UV focusing objective. A LabView program was written to control the MM3000 and automate x-y position control, while also reading current measurements from a lock-in amplifier. The automated scan moved the spot on the device from left to right in 2 µm steps by moving the objective, with a total length (set by the user) to cover the device mesa. The program then returned the spot to the left and moved it down 2 µm, scanning again from left to right. This process was repeated until a second preset distance was covered.

The 250 µm-diameter mesa device of Figure 3.4(a) (with no recessed window) shows a spatially uniform photoresponse across the exposed *p*-GaN surface with the ring-shaped trough mapping out the *p*-type metal contact. The gap in the trough is due to shadowing by the metal probe tip. In contrast, Figure 3.4(b) shows a strong spatial non-uniformity in photoresponse across the device with a recessed window. While the inner rim region, within ~20 µm of the inside of the ring *p*-contact, exhibits an enhanced photocurrent, the central region shows a diminished photoresponse. This can be explained by the electric field "crowding" underneath the *p*-contacts due to the poor field spreading in the *p*-$Al_{0.13}Ga_{0.87}N$ layer. The poor electric field spreading was a result of a large lateral resistance in this layer. Most likely the large resistance was caused by the low room temperature activation of Mg in $Al_xGa_{1-x}N$ discussed in Section 2.2.

3.3 SEMI-TRANSPARENT *P*-CONTACT

In order to improve the spatial non-uniformity in the photoresponse seen in Figure 3.4(b), a uniform electric field was needed across the recessed window area. To achieve this we used a semi-transparent *p*-contact in addition to the normal ring *p*-contact [76]. Figure 3.5 shows a schematic drawing of the top-

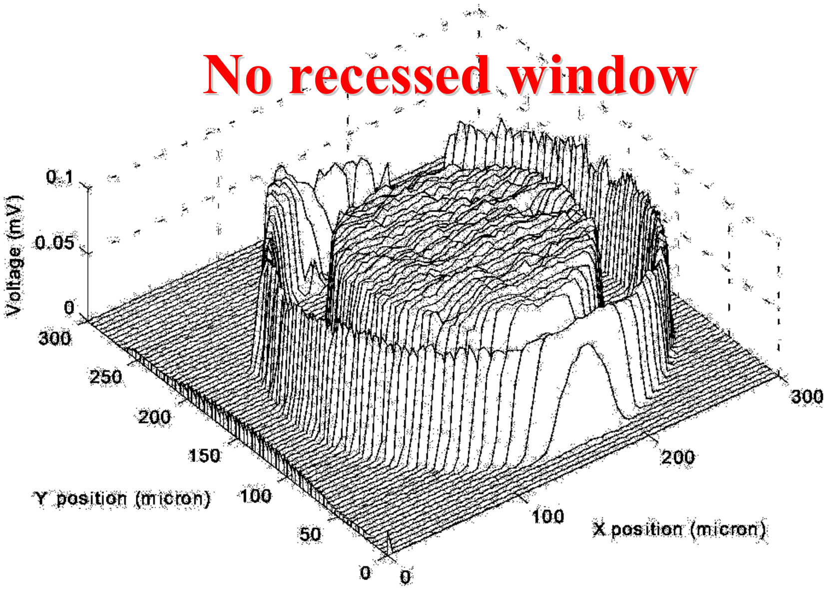

(a)

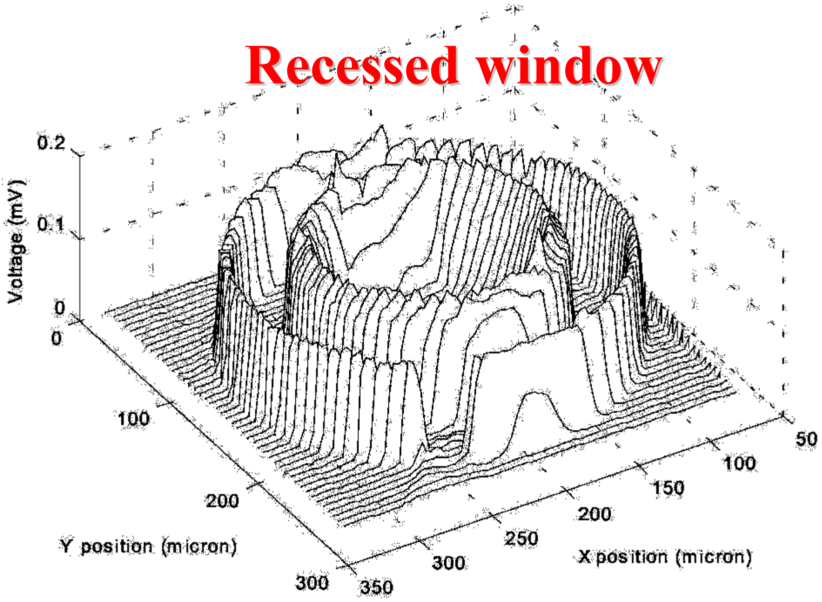

(b)

Figure 3.4: Raster scan photocurrent measurements on 250 μm-diameter AlGaN/GaN p-i-n devices: (a) no recessed window (b) 0.14 μm recessed window depth.

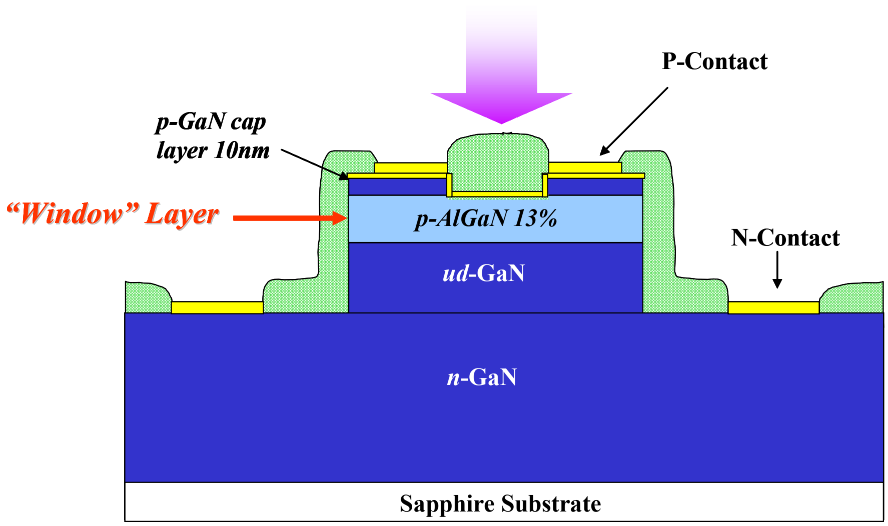

Figure 3.5: Schematic cross section of an $Al_{0.13}Ga_{0.87}N$/GaN window *p*-region device with a recessed window and a semi-transparent *p*-contact.

illuminated device. The structure consisted of four epitaxial layers grown on basal-plane single-polished sapphire substrate using a low-temperature GaN nucleation layer. The first layer grown was a 3.6 µm-thick, Si-doped ($N_d \sim 10^{19}$ cm^{-3}) *n*-GaN layer. This was followed by a 0.8 µm-thick, unintentionally-doped ($N_d \sim 10^{16}$ cm^{-3}) absorption region. The next layer was a 0.5 µm-thick Mg-doped *p*-$Al_{0.13}Ga_{0.87}N$ window layer. The wafer was capped with a 100 Å, Mg-doped *p*-GaN layer to reduce the contact resistance. Hall effect measurements indicate that the Mg-dopant activation resulted in a free hole concentration of $p \sim 3\times10^{17}$ cm^{-3}. Standard processing, as described in Section 2.3, was used to define mesas and activate the Mg. Photoresist was then patterned with holes to open the recessed windows in the RIE. This hard-baked photoresist was then removed, and a thin layer of photoresist was spun on and patterned to cover the mesas (and recessed windows) with a semi-transparent contact, consisting of 30 Å Ni followed by 50 Å Au. The standard procedure was then used to deposit SiO_2 and the Ti/Al/Ti/Au *n*-contacts. Ring Ni/Au *p*-contacts were then deposited on top of the semi-transparent contact.

3.4 ELECTRICAL CHARACTERIZATION

Standard I-V measurements were performed using an HP4145. Figure 3.6(a) shows the reverse bias dark current and ultraviolet (UV) photoresponse. The device was illuminated from the top with a broad-band UV light source that covered an area > 10 times the device area. The dark current density was a low value of ~0.3 nA/cm^2 at a reverse bias of 10V, and there was a strong, flat UV photoresponse. The low leakage current density implies well-passivated mesa sidewalls and high-quality junction interfaces. Figure 3.6(b) shows a typical forward I-V characteristic for these diodes. The forward current was > 10 mA at a bias of 5 V with a strong turn on voltage at ~3 V, as expected for a high-quality GaN *pn* junction. High forward bias current at low voltage suggests that these

$$\frac{dV}{dI} I = R_S I + \frac{nkT}{q} \qquad 3.1$$

devices had low series resistance. Rearranging the diode equation, as shown in Equation 3.1, allows for the determination of the series resistance, R_S, from the slope of a linear curve fit. Figure 3.7 shows a plot of I dV/dV vs. I for a typical

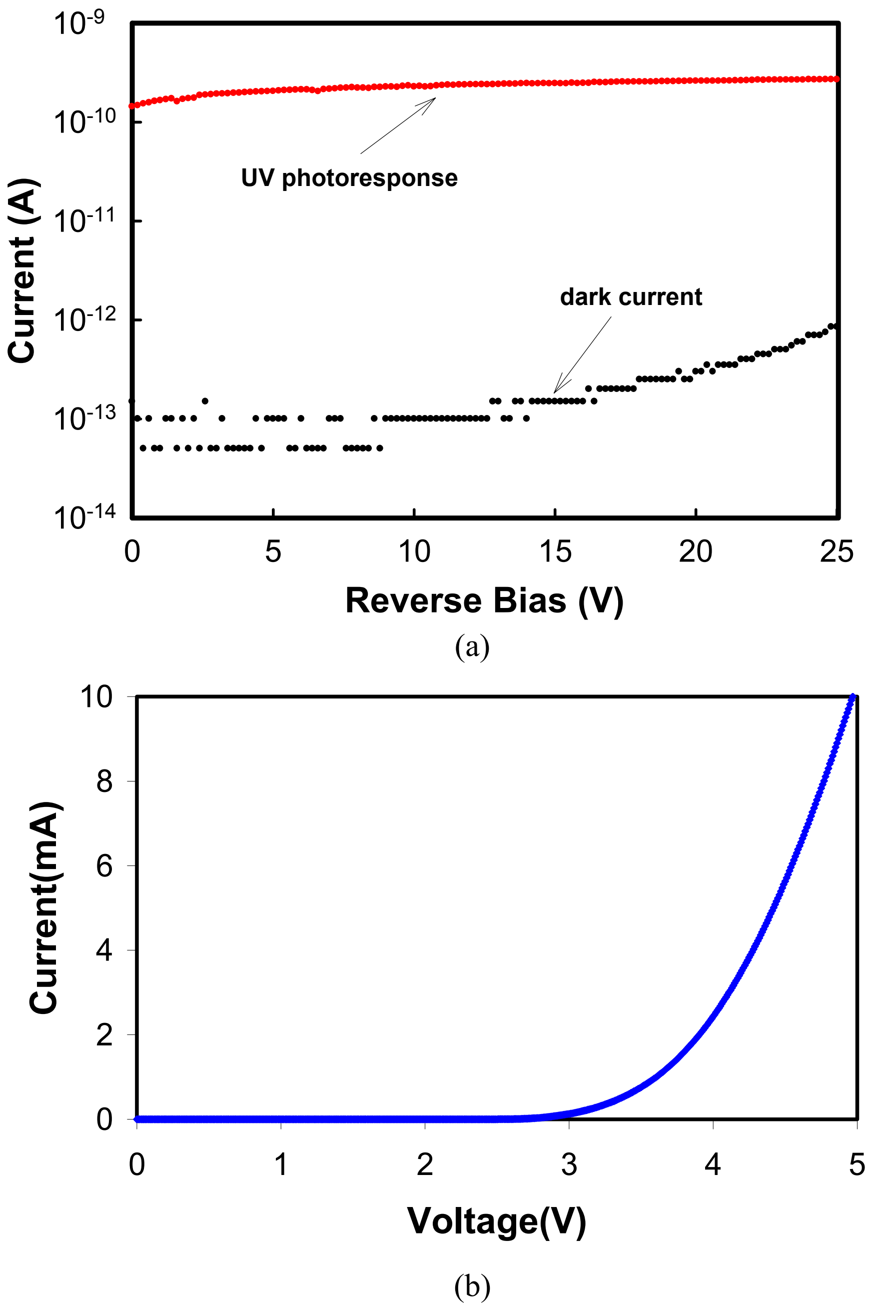

Figure 3.6: (a) Reverse I-V characteristics under dark and UV illumination. (b) Forward I-V characteristics showing a large forward current of >10 mA at 5 V bias.

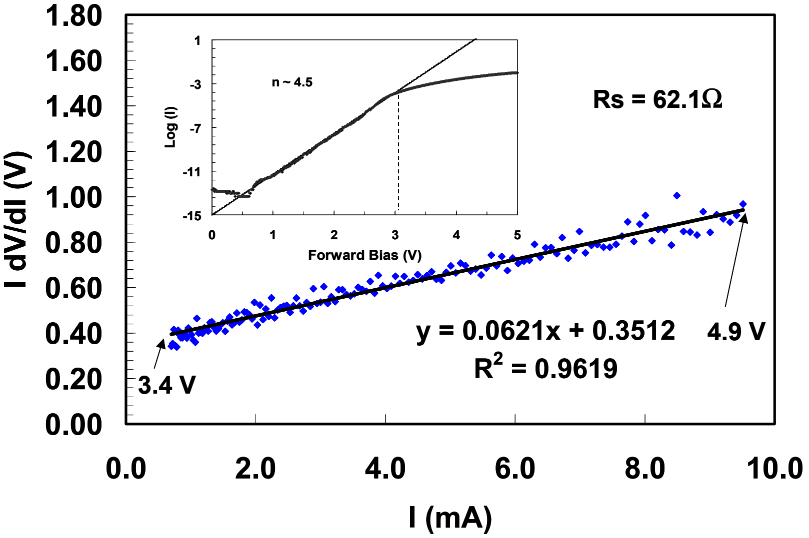

Figure 3.7: Plot of I·dV/dI vs I. The slope of the linear curve fit gives a series resistance of ~62 Ω for a 250 μm device.

diode. The slope of the linear fit yielded a series resistance of 62.1 Ω for a 250 μm-diameter device. The inset of Figure 3.7 shows a Log(I)-V plot of the forward current where the low-level injection regime was fit to obtain an ideality factor n = 4.5.

3.5 QUANTUM EFFICIENCY AND TIME RESPONSE

Ring contact devices were used for top-illuminated external quantum efficiency measurements using a procedure described in Section 2.5. Figure 3.8 shows the external quantum efficiency for a typical 250 μm-diameter photodetector. The zero bias external quantum efficiency peak was ~77% at 357 nm and showed no bias dependence. The external quantum efficiency remained relatively constant at lower wavelengths until the window *p*-region begins to absorb, at which point there was a sharp drop-off. This short wavelength response was bias dependent due to the absorption region extending into the window *p*-region at higher bias. The low external quantum efficiency at short wavelengths is due to the short diffusion length of electrons, and the large absorption coefficient of $Al_{0.13}Ga_{0.87}N$ layers for $\lambda \leq 340$ nm. The same optical "dead space" effects described earlier in this chapter applies for wavelengths that the "window" *p*-layer absorbs.

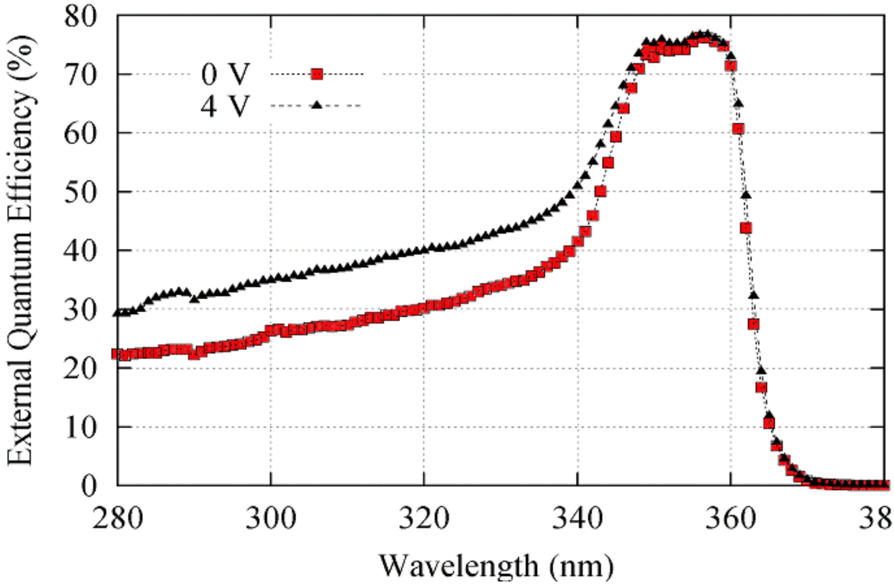

Figure 3.7: External quantum efficiency of a typical semi-transparent p-contact device showing a zero bias peak of 77% at 357 nm.

Another important characteristic of a photodiode is its temporal response. Dr. Carrano measured the temporal response of the photodiodes using a modelocked Ti:sapphire laser pumped by an argon laser. The infrared output (λ = 800 nm) of the Ti:sapphire was directed to the input of a CSK tripler to produce a UV signal (λ = 267 nm). The beam was then focused onto the device under test using a UV grade microscope objective. A high-speed bias-tee was used to provide DC reverse bias and capacitively couple the AC signal out to a 20 GHz digital oscilloscope. An ammeter was used to monitor the DC photocurrent at all times.

At a wavelength of λ = 310 nm, a narrow full width at half maximum (FWHM) of ~ 80 ps at -20 V was obtained, as seen in Figure 3.9. Note the symmetric pulse response and almost negligible slow-component tail which disappears completely after ~300 ps. A calculated RC-limited bandwidth in excess of 5 GHz, along with the absence of a pronounced slow component tail, lead us to believe that these devices were not RC limited.

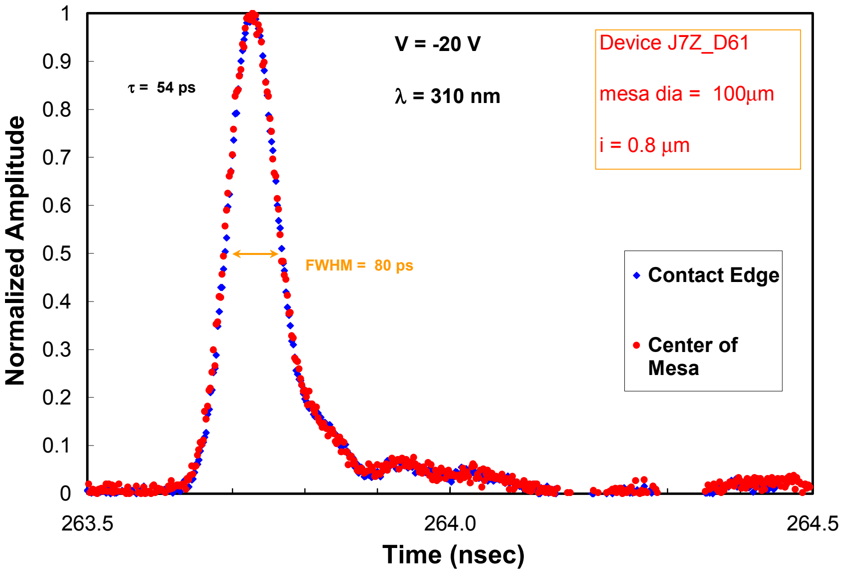

Figure 3.8: Time response curves measured at λ = 310 nm. The time response showed no spatial dependence.

Previously we had investigated the spatial dependence of the time response for the GaN homojunction devices with only a thick ring *p*-contact (no semi-transparent layer). There was a considerable increase in the FWHM as the illumination was moved away from the edge of the *p*-contact. Furthermore, at the center of the mesa there was no measurable signal. Figure 3.9 shows the response for the semi-transparent devices near the *p*-contact and at the center of the mesa. The temporal response for these devices was independent of beam spot position. The absence of spatial dependence in the time response is directly correlated with the uniform electric field created by the improved *p*-contact. Photogenerated carriers in the center of the mesa experience a high field and are quickly swept out. This is consistent with the Gaussian shape and diminished slow (diffusion) component of the time response.

3.6 SUMMARY

Dr. Carrano's and Dr. Li's recessed window GaN homojunction devices achieved zero bias external quantum efficiecies of ~60% at 360 nm. We incorporated a "window" AlGaN *p*-region with the recessed window structure in an attempt to reduce *p*-region absorption. It was found that the *p*-AlGaN layer was very resistive and caused current crowding underneath the ring contacts. To avoid this, we deposited a thin Ni/Au semi-transparent *p*-contact over the entire mesa. This resulted in record zero bias external quantum efficiencies of ~77% at 360 nm, and a temporal response that showed a uniform electric field profile. These devices, however, were not solar-blind. From here we needed to push the peak external quantum efficiency toward the solar-blind by adding aluminum to the absorption layer. This zero bias external quantum efficiency of ~77% will be used as a standard for what we want to achieve with our back-illuminated solar-blind detectors.

4. Selective-area Regrowth of $Al_{0.3}Ga_{0.7}N$ *p-i-n*

4.1 INTRODUCTION

We have demonstrated top-illuminated photodiodes with GaN absorption regions having high external quantum efficiency (~77%) and low dark currents. Our goal, however, was to move to the solar-blind (see Chapter 1) portion of the spectrum. To do this, we needed to increase the amount of aluminum in the absorption region, and get the carriers to within a diffusion length of it. We were still confined to using GaN buffer and template layers for top-illuminated devices because the $Al_xGa_{1-x}N$ template layers were still being perfected. Thus, we started to grow $Al_xGa_{1-x}N$ epitaxial device layers on top of these high quality GaN template layers. We felt that we could reliably grow both *n*-type and *p*-type $Al_{0.30}Ga_{0.70}N$ and thus utilize this composition as a first step toward achieving solar-blind devices. As stated earlier, when the aluminum concentration of the epitaxial layers increase, the lattice mismatch between the GaN template layers and the $Al_xGa_{1-x}N$ device layers also increase. This introduces tensile strain into the crystal, which eventually leads to cracking at a critical thickness [77-80]. It has been suggested that upon cooling from the high growth temperatures, the differences in the thermal expansion coefficients of the GaN template layer and the $Al_xGa_{1-x}N$ epitaxial layers results in additional tensile strain [78], however, the lattice mismatch seems to be the dominant factor [80,81]. The critical thickness is dependent on both the template layer and the composition of the device layer. This thickness can be calculated using equation 4.1:

$$t_{crit} = 2 \cdot nm \cdot \frac{a_{oAl} \cdot x + a_{oGaN} \cdot (1 - x)}{x \cdot (a_{oGaN} - a_{oAlN})} \tag{4.1}$$

where a_{oAlN} = 3.1106 Å and a_{oGaN} = 3.1892 Å are the "a" lattice parameters for AlN and GaN, respectively, and x is the aluminum concentration of the $Al_xGa_{1-x}N$ layer[82]. Thus, it should not be possible to grow an $Al_{0.30}Ga_{0.70}N$ layer to ~270-nm-thickness on bulk GaN without cracking. This imposes a limit on the total thickness for the device layers. It was found, however, that as the $Al_{0.30}Ga_{0.70}N$ thickness approached this critical thickness, cracking was so severe that there was not sufficient space between the cracks to fabricate a photodectector.

To overcome this cracking problem selective-area regrowth was investigated. It had been shown previously that selective-area regrowth of strips of $Al_xGa_{1-x}N$ on GaN template layers can relieve strain at the regrowth sidewalls [83]. With that as motivation we fabricated photodiodes for which the mesa was defined by selective-area regrowth instead of reactive-ion etching. By using this regrowth technique, and keeping the layers as thin as possible, we anticipated that cracking could be eliminated or greatly reduced.

4.2 MATERIAL GROWTH AND PROCESSING

Figure 4.1 shows a schematic cross section of the selective-area regrowth devices. The structure consists of five epitaxial $Al_{0.3}Ga_{0.7}N$ layers and two epitaxial GaN layers grown by low-pressure metalorganic chemical-vapor deposition on a 2-in.-diameter *c*-plane (0001) single-polished sapphire substrate. Growth began with a thin, low-temperature GaN nucleation layer followed by a

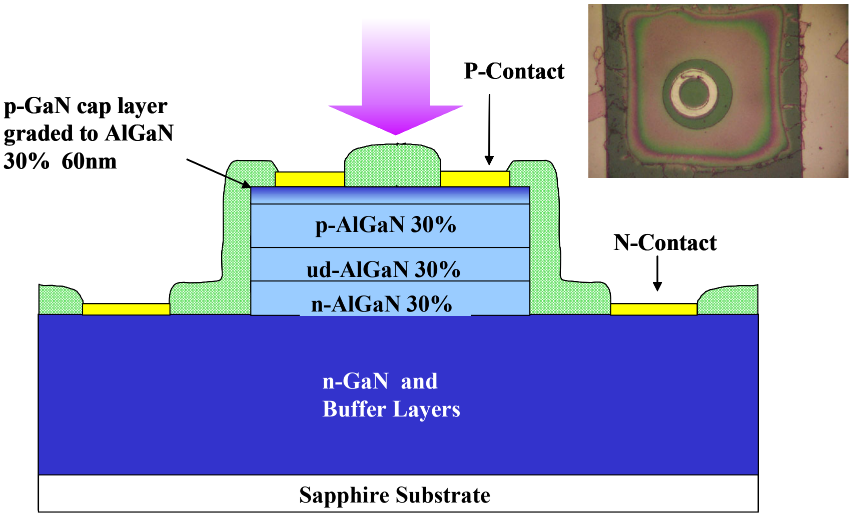

Figure 4.1: Schematic cross section of a typical selective regrown AlGaN/GaN device.

thick, high-temperature GaN buffer layer that was designed to improve the subsequent device layers by limiting the defect density. An n^+-GaN layer was then grown to insure good *n*-contacts. The wafer was then cooled and removed from the growth chamber. To perform selective-area regrowth a mask is needed to define the regrowth area. We deposited a 300 nm-thick SiO_2 layer in the PECVD chamber and used photoresist and an “inverted mesa” mask layer (where the dark and clear areas were opposite from the normal mesa mask layer) to define the regrowth openings. Buffered oxide etchant was then used to remove the SiO_2 inside the openings and the photoresist was removed. After the growth mask was formed, the wafer was cleaned with solvents and returned to the growth chamber where it was slightly etched to insure removal of surface contamination.

Selective-area regrowth of the $Al_{0.30}Ga_{0.70}N$ *p-i-n* structure was performed in the mask openings. To insure a good *p*-contact without cracking, a thin graded layer from the $Al_{0.30}Ga_{0.70}N$ to GaN was grown along with a GaN cap layer.

It should be noted that to make sure that the substrate did not fall off the rotating platter during material growth in the MOCVD chamber, the substrate was required to be at least a quarter of a 2-in. wafer. Thus, the above growth and subsequent regrowth were done on a quarter wafer. After removal from the chamber, the quarter wafer was cleaved into smaller samples to finish the processing. In this case the 850°C/10 min. Mg activation anneal was not performed because the device layers were thin and we did not want to risk the Mg diffusing across the junction. *N*-contacts and *p*-contacts were deposited as usual. The inset of Figure 4.1 is a top-view of a finished device. The jagged SiO_2 around the mesa was due to difficulties in removing the SiO_2 for *n*-contact deposition. The SiO_2 mask was placed in the growth chamber and brought to high temperatures during regrowth (~1100 °C). This hardened the SiO_2, and possibly changed its structure, leading to difficulties in removing it with the standard buffered oxide etch. The sample had to be submersed in the buffered oxide etch and placed in an ultrasonic bath to remove the SiO_2 for *n*-contact deposition.

The regrown $Al_{0.30}Ga_{0.70}N$ device layers had a spatial thickness variation. Growth occurred only inside the mask openings, and not on the SiO_2 mask. The reactants that hit the SiO_2 mask had a high surface mobility at the growth temperature, and thus moved around freely until they found a mask opening.

Thus, the reactant flux from the edge of the circular opening was much larger than the center flux and a saddle shaped regrowth occurred. Figure 4.2 shows a sketch of this non-uniform regrowth with reactant motion. The thickness of the center of the regrown mesas varied depending on the mesa opening diameter. Larger devices had a thinner center thickness than smaller devices. For these samples the thickness varied from ~1500 Å for a 74 µm-diameter device, to 800 Å for a 250 µm-diameter device. It was found that for this regrowth thickness devices with regrown mesa diameters greater than 74 µm exhibited cracking, while those with diameters equal to or less than 74 µm did not, even though the larger diameter devices had thinner regrown layers. From the standard critical thickness model, one would expect thicker layers to crack before thinner layers due to the build up of lattice mismatch strain, however, this was not observed to be the case for the regrown layers. This was seen previously in the growth of GaN strips [83], where the reduction in the amount of cracking in narrow strips was attributed to the

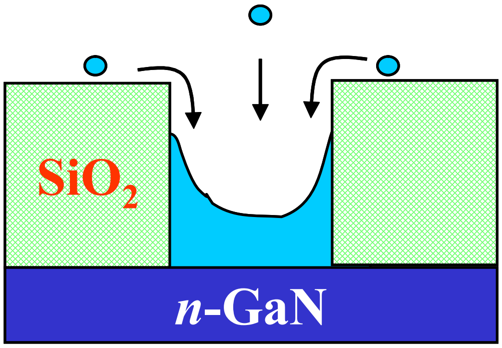

Figure 4.2: Schematic cross section of non-uniform selective-area regrowth.

relaxation of excess strain at the mesa edges. Devices with larger perimeter to area ratios should, therefore, exhibit less cracking.

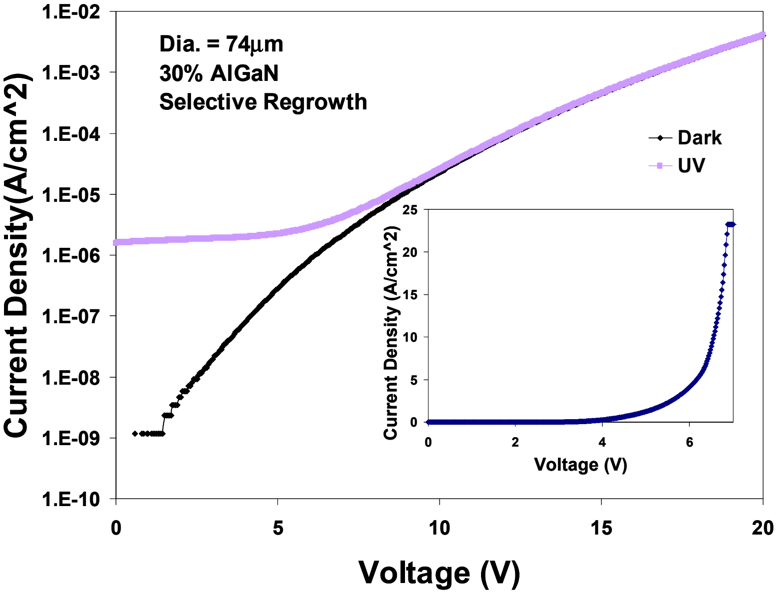

Figure 4.3: Reverse I-V characteristics of the dark current and the ultraviolet photoresponse of a typical photodetector. Inset is the forward I-V curve.

4.3 ELECTRICAL CHARACTERIZATION

Only crack-free devices were characterized in detail. Devices with cracks behaved like shorted junctions, which is consistent with an earlier result [77]. The data presented in this chapter were obtained from a 74 μm-diameter device from section G of the mask layout (see appendix A). The devices exhibited low dark current densities of ~5 ×10^{-8} A/cm^2 at a reverse bias of 5V. Figure 4.3 shows the dark current density and UV photoresponse for a typical device. The devices were top-illuminated with a broad-band UV light source, and showed a strong, flat photoresonse. The inset of Figure 4.3 shows the forward-bias current density with a strong turn-on current of ~25 A/cm^2 at 7 V.

4.4 EXTERNAL QUANTUM EFFICENCY

Ring contact devices were used for top-illuminated external quantum efficiency measurements using a procedure described in Section 2.5. Figure 4.4 shows the external quantum efficiency [84]. The zero bias external quantum efficiency peaked at $\lambda = 314$ nm with a value greater than 20%. This peak was shifted 50 nm toward the solar-blind region compared to that of the GaN absorption region devices discussed in Chapter 3. The long wavelength response is due to absorption in the GaN *n*-region. The $Al_{0.30}Ga_{0.70}N$ device layers allow

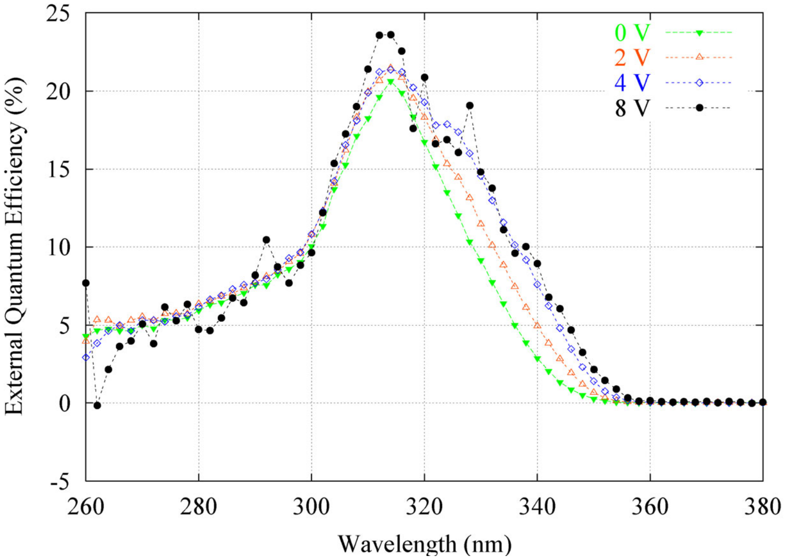

Figure 4.4: External quantum efficiency of a 74 mm diameter device. The zero bias external quantum efficiency was greater than 20%.

longer wavelength light to pass to the GaN *n*-region where it is absorbed. A small amount of the resulting photo-induced carriers diffuse back into the deletion region and are collected by the device. In addition, the short wavelength drop-off is due to the optical dead space discussed in Chapter 3. This device structure was the first step in moving the absorption peak to solar-blind wavelengths. By further increasing the aluminum percentage of the absorption region, the external quantum efficiency peak should shift further toward the solar-blind goal.

4.5 CURVE FIT CALCULATION OF DETECTIVITY

Operation of these UV photodiodes in the photovoltaic mode would allow us to take advantage of the low dark current resulting in large detectivity [9]. To further examine the dark current of these devices near zero bias, an HP 4156B parameter analyzer was used with low-noise Kelvin probes that are capable of measuring currents as low as 10 fA. To get accurate low noise measurements, the integration time on the HP 4156B was set to "high", and the I-V data was taken with 0.01 V steps. The absolute value of the current is plotted on a log plot in Figure 4.5(a). Curve fitting was performed using exponential fits to both the forward and reverse bias curves. The constants obtained from curve fitting were then used in the following equation:

$$I = a(e^{b \cdot V} - 1) + c(e^{d \cdot V} - 1) \qquad 4.2$$

where a and b are the coefficients from the reverse bias fit (a = -1.1 $\times 10^{-15}$ A, b = -2.6 V^{-1}) and c and d are the coefficients from the forward bias fit (c = 5.2 $\times 10^{-21}$ A, d = 25.9 V^{-1}). Equation 4.2 was then plotted with the experimental data as seen in Figure 4.5(b). A good fit to the experimental data was achieved using this method. An important value when calculating the detectivity for these devices is the differential resistance, R_O, which is the inverse derivative of the I-V curve at zero bias. Since the dark current is below the noise floor of our I-V measurement setup near zero bias, we use the curve fit equation to estimate the differential resistance:

$$\frac{1}{R_O} = \left.\frac{dI}{dV}\right|_{V=0}, \qquad R_O = \frac{1}{ab+cd} \tag{4.3}$$

For this fit, $R_O = 3.46 \times 10^{14}\ \Omega$ and, taking the device diameter to be 74 μm, $R_OA = 1.33 \times 10^{10}\ \Omega\cdot\text{cm}^2$. To calculate the detectivity we first assume that these photodiodes were thermal noise limited. This is a good assumption for wide bandgap semiconductors near zero bias [9]. In this case the noise current spectral density, S_n, is given by:

$$S_n = \frac{4kT}{R_O} \tag{4.4}$$

The R_OA value from above was then used along with the zero bias responsivity (R_λ), to estimate the device detectivity, D^*, using:

$$D^* = R_\lambda \sqrt{\frac{R_O A}{4kT}} \tag{4.5}$$

where *k* is Boltzmann's constant and T is the device temperature. This yielded a detectivity of $D^* = 4.85 \times 10^{13}\ \text{cm}\cdot\text{Hz}^{1/2}\cdot\text{W}^{-1}$. This method of exponential fitting is

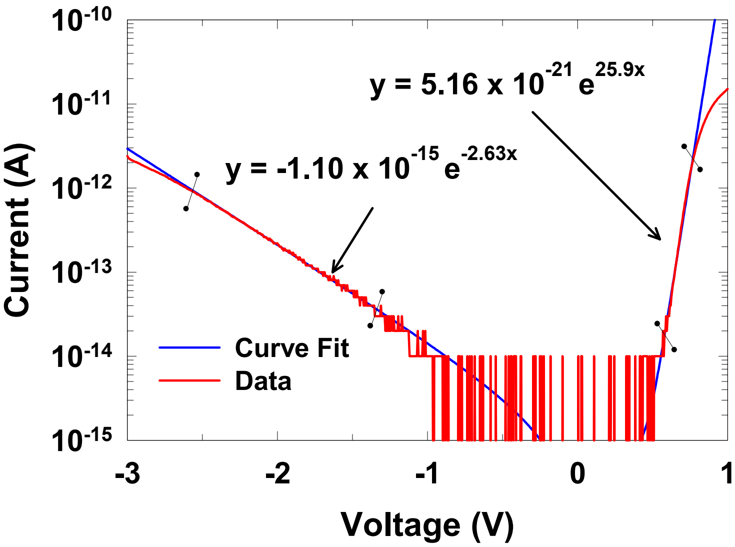

(a)

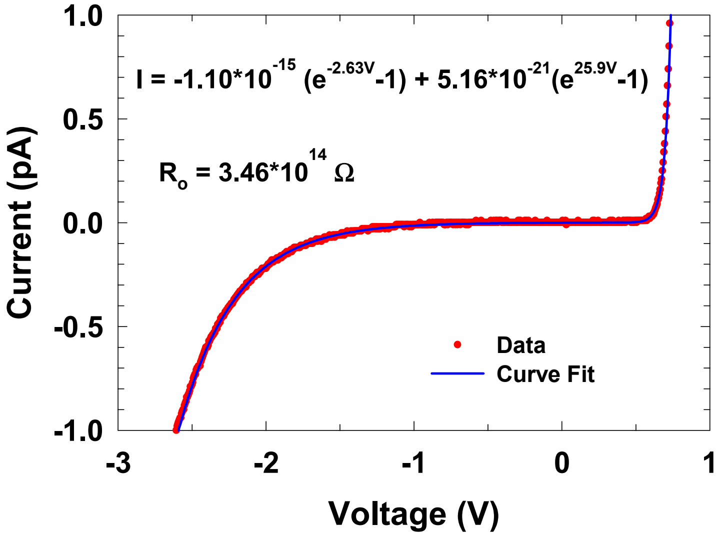

(b)

Figure 4.5: (a) Log plot of the absolute value of I-V data close to 0 V with exponential fit. Curve fitting was performed between the vertical bars. (b) Linear plot of I-V data and exponential fit.

superior to the standard polynomial fits due to its ability to approximate asymmetric junctions accurately. In addition, we found that small variations in the polynomial fit parameters could give many orders of magnitude change in D^*, even though the fits were almost identical when plotted with the experimental data.

4.6 SUMMARY

We have used a selective regrowth technique to reduce the effects of tensile-strain-induced cracking which is often observed when growing high-aluminum concentration $Al_xGa_{1-x}N$ layers on GaN. We were able to achieve low dark current, a flat photoresponse, and a strong forward turn-on current. The zero bias external quantum efficiency peak was shifted 50 nm toward solar-blind with a peak value of ~20% at 315 nm. To reach our goal of solar-blind photodetectors, even more aluminum must be added to the *i*-region.

5. Back-Illuminated Solar-Blind $Al_xGa_{1-x}N$ *p-i-n*

5.1 INTRODUCTION

As the AlN buffer layers and $Al_xGa_{1-x}N$ material quality improved, devices were designed with “window” template and buffer layers. This allowed us to move to a back-illuminated device design to facilitate flip-chip mounting. Figure 5.1 shows a diagram of an $Al_xGa_{1-x}N$ photodetector array flip-chip mounted to a silicon readout circuit. By using this flip-chip method, the amplifier and other support circuitry can be designed in CMOS silicon and bonded to the photodetector array to produce the final imager package [53].

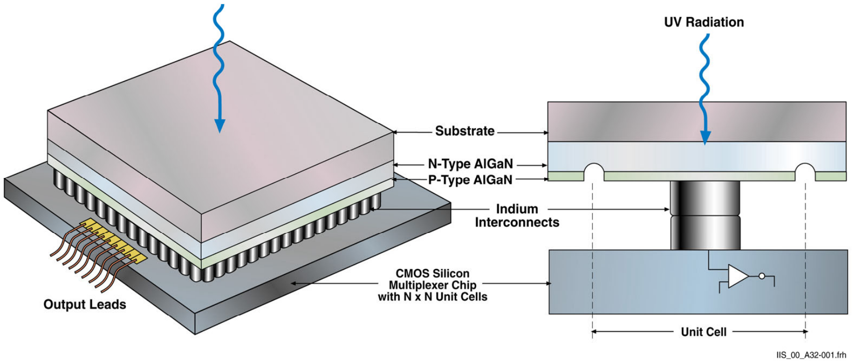

Figure 5.1: Flip-chip bonding of $Al_xGa_{1-x}N$ photodetector arrays to silicon read-out circuits. Light is shined through the double-polished sapphire substrate.

In this chapter we report the growth, fabrication, and characterization of back-illuminated solar-blind *p-i-n* photodetectors with $Al_{0.60}Ga_{0.40}N$ as a “window” template layer and $Al_{0.40}Ga_{0.60}N$ as active layers. The main difficulty in growing such devices is cracking due to the substantial lattice mismatches between $Al_{0.60}Ga_{0.40}N$, $Al_{0.40}Ga_{0.60}N$, and GaN [88]. There is also a *p*-type doping problem, as discussed in Section 2.2, which results from the large activation energy for Mg acceptors in high Al-content $Al_xGa_{1-x}N$ alloys. In addition, there is an *n*-type doping problem, where the activated density of donors drops sharply with increasing aluminum percentage above ~ 40%. Thus, the devices were designed with $Al_{0.40}Ga_{0.60}N$ active layers as seen in the schematic diagram of Figure 5.2. The realization of a back-illuminated scheme has the advantage of avoiding transmission through the *p*-GaN and *p*-$Al_xGa_{1-x}N$ layers that are believed to have significant band-bending near the surface, which causes an optical "dead space" (Section 3.1) at the surface that leads to reduced external quantum efficiency [48]. In addition, the *p*-contact can cover the entire mesa, avoiding any current crowding problems (Section 3.2).

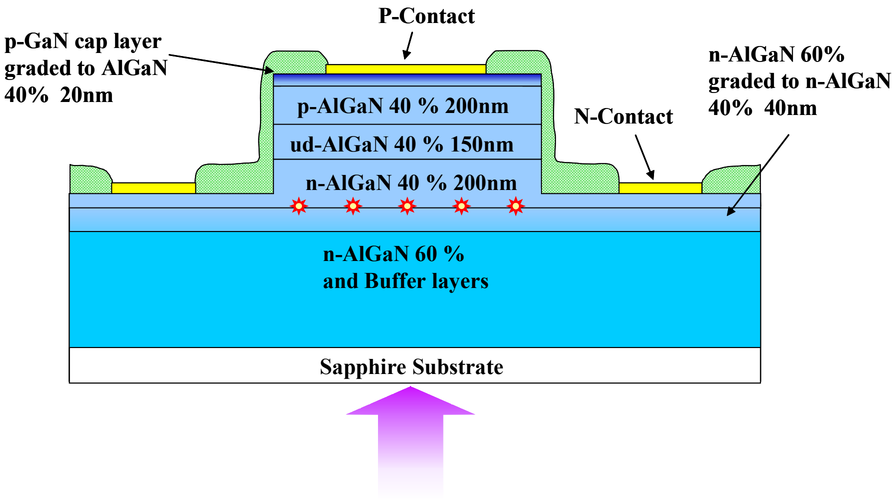

Figure 5.2: Schematic diagram of a back-illuminated solar-blind $Al_xGa_{1-x}N$ *p-i-n* photodetector device structure.

5.2 MATERIAL GROWTH AND DEVICE FABRICATION

The back-illuminated solar-blind heterostructures described in this chapter were grown by low-pressure metalorganic chemical vapor deposition (MOCVD) on two-inch diameter *c*-plane (0001) double-polished sapphire substrates. For back-illuminated devices, a low temperature (~ 550°C), pseudomorphic ~20 nm-thick AlN buffer layer was developed to replace the GaN buffer layer that was used for top-illuminated structures. Then the temperature was ramped to ~ 1100°C for growth of an undoped ~ 700 nm-thick $Al_{0.60}Ga_{0.40}N$ template layer to improve the material quality for the subsequent device layers by reducing the defect density. In addition, both the AlN buffer layer and the $Al_{0.60}Ga_{0.40}N$ template layer are used as an optical window for radiation $\lambda > 240$ nm. After the thick $Al_{0.60}Ga_{0.40}N$ template layer, the Al composition was graded from 60% to 40% over a 36 nm-thick epitaxial region to help reduce the strain induced cracking in the subsequent $Al_{0.40}Ga_{0.60}N$ device layers. First, a 200 nm-thick *n*+-$Al_{0.40}Ga_{0.60}N$ epitaxial layer was grown. This was followed by a 150 nm-thick $Al_{0.40}Ga_{0.60}N$ unintentionally doped layer (*i*-layer) and a 200 nm-thick *p*-$Al_{0.40}Ga_{0.60}N$ layer. Finally, the Al composition was graded from 40% to 0% over a 10 nm-thick epitaxial region to allow for the growth of a crack-free 10 nm-thick *p*+-GaN contact layer. Contacts made directly on the *p*-$Al_{0.40}Ga_{0.60}N$ layer were found to be Schottky-like; the GaN contact layer was used to improve the *p*-contact. In-situ monitoring of the reflectivity of the wafer versus time with an Epimetric system was used to determine an $Al_{0.60}Ga_{0.40}N$ growth rate of ~ 74 Å/min. and an $Al_{0.40}Ga_{0.60}N$ growth rate of ~ 100 Å/min. The devices were fabricated using the standard processing discussed in Section 2.3. Ohmic contacts were made using Ti/Al/Ti/Au *n*-contacts, annealed at 850°C for 30 sec., and Ni/Au *p*-contacts, annealed at 675°C for 2 min.

As discussed in Section 2.2, as the concentration of aluminum was increased in the $Al_xGa_{1-x}N$ layers, the activation energy for ionization of Mg acceptors was found to increase. For *p*- $Al_{0.40}Ga_{0.60}N$ it is estimated that only ~ 0.007% of Mg acceptors are ionized at 300K. Therefore, the *p*-$Al_{0.40}Ga_{0.60}N$ is grown with 10^{20} Mg atoms/cm^3 in order to obtain lightly doped *p*-type material with a free hole concentration of $p \sim 7\times10^{15}$ cm^{-3} at 300K. This layer will only be *p*-type if the donor-like native defects and N vacancies of the material do not fully compensate this low hole concentration. The high Mg impurity level can be seen

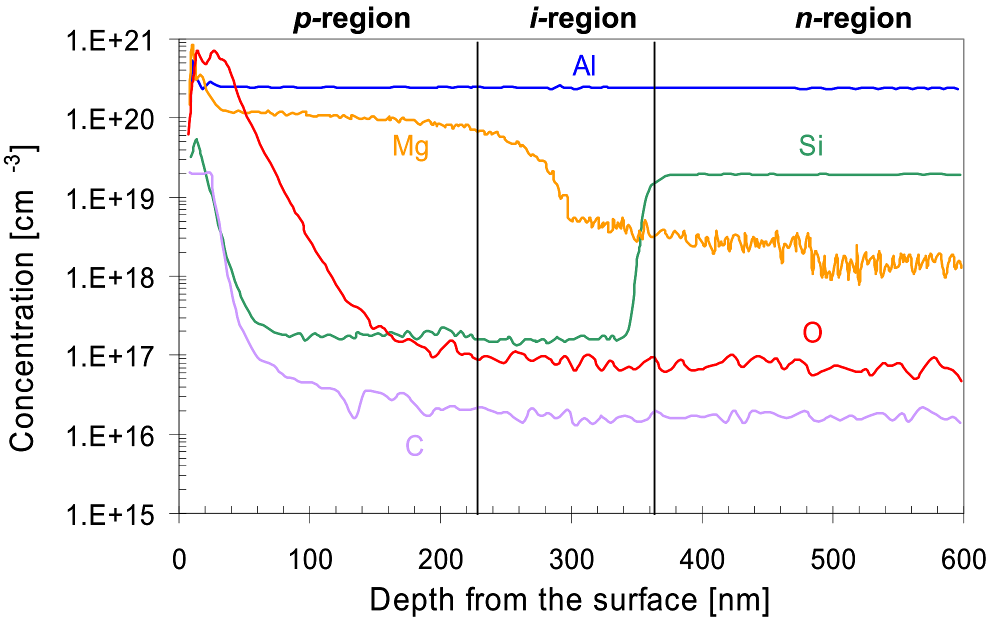

Figure 5.3: SIMS data for the $Al_{0.40}Ga_{0.60}N$ active layers showing the dopant and impurity concentration profile versus depth.

in the SIMS data of Figure 5.3. The small size and large concentration of Mg atoms and the relatively high density of defects in the $Al_xGa_{1-x}N$ films are probably responsible for the back-diffusion of Mg atoms into the unintentionally doped *i*-layer. This effect seems to be dependent on the *p*-layer thickness, with thicker layers taking longer to grow at the high growth temperature, thus increasing the amount of Mg diffusion. This effect made it difficult to grow abrupt *p-i* junctions and may account for the bias dependence seen in external quantum efficiency measurements. Si atoms, which are used for *n*-type doping, are larger and thus did not diffuse as much as Mg atoms. The Al concentration in the SIMS data is constant since all the active layers of the device are $Al_{0.40}Ga_{0.60}N$, and the depth of the measurement did not reach the $Al_{0.60}Ga_{0.40}N$ buffer layer.

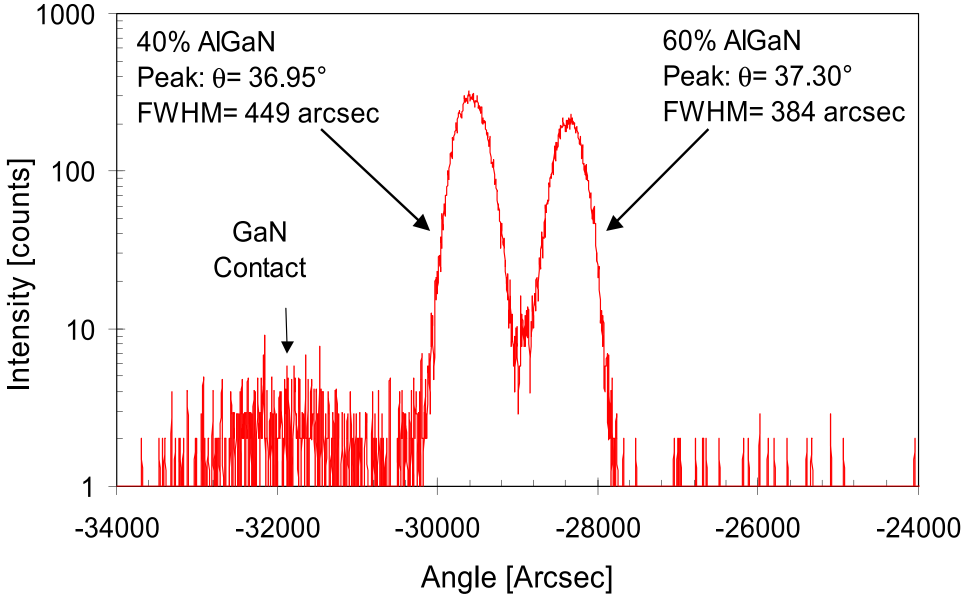

Figure 5.4: (004) ω-2θ X-ray scan of the $Al_xGa_{1-x}N$ solar-blind detector wafer.

The (0004) ω-2θ X-ray scan of the as-grown solar-blind photodetector device structure, shown in Figure 5.4, indicates that $Al_xGa_{1-x}N$ material quality is relatively good. The (004) full width at half maximum (FWHM) for the $Al_{0.40}Ga_{0.60}N$ device layers is ~ 449 arcsec and the FWHM for the $Al_{0.60}Ga_{0.40}N$ buffer layer is ~384 arcsec. The alloy composition for the $Al_xGa_{1-x}N$ films were estimated from the (004) peak positions located at θ = 36.95° for $Al_{0.40}Ga_{0.60}N$ and θ = 37.30° for $Al_{0.60}Ga_{0.40}N$. These peaks were compared to the (0012) Al_2O_3 reference peak, located at θ = 45.18°, to calculate the alloy composition.

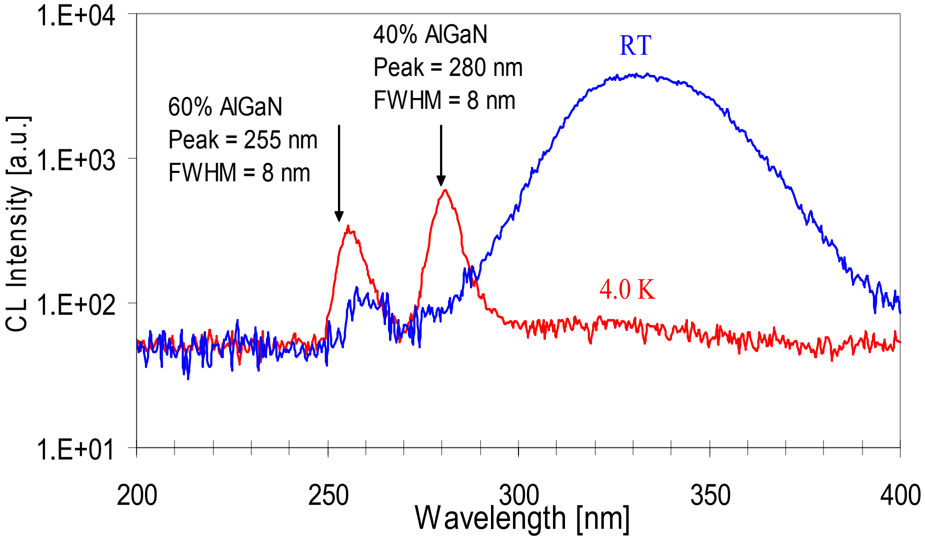

Figure 5.5: Cathodoluminescence data of the $Al_xGa_{1-x}N$ solar-blind wafer at room temperature and 4.0 K.

The cathodoluminescence (CL) for this wafer, shown in Figure 5.5, was measured with an Oxford Instruments MONOCL2 cathodoluminescence system. In the room-temperature CL data the band-edge of both the $Al_{0.40}Ga_{0.60}N$ and the$Al_{0.60}Ga_{0.40}N$ are barely discernible. The large tail that is seen instead indicates that carrier recombination occurs preferentially through deep levels in the material. To resolve the $Al_xGa_{1-x}N$ peaks, the sample was cooled to T = 4 K, freezing out the traps and allowing band-to-band recombination to dominate. The $Al_{0.60}Ga_{0.40}N$ peak at λ = 255 nm and the $Al_{0.40}Ga_{0.60}N$ peak at λ = 280 nm show narrow FWHM of ~ 8 nm. These low temperature peaks were compared to X-ray data to confirm the Al composition of the $Al_xGa_{1-x}N$ layers.

5.3 ELECTRICAL CHARACTERIZATION

These solar-blind detectors showed improved I-V characteristics. The dark current and UV photoresponse, generated by a broad-band UV light source, for a 250 μm-diameter device are shown in Figure 5.6. In reverse bias, the dark current density had a low value of ~ 5 nA/cm^2 at -10 V, and only increased to ~ 20 nm/cm^2 at -20 V. The strong UV photoresponse was relatively flat. A forward current density of ~ 0.3 A/cm^2 was achieved at 10 V. These diodes exhibited a high series resistance of R_S ~ 5 kΩ, calculated using equation 3.1 and the forward bias current data. However, these devices still showed ~ 8 decades difference in the current density from -10 V to 10 V, suggesting a high quality *p-n* junction. These diodes had better I-V characteristics than many previous back-illuminated solar-blind growth runs. This was most likely due to the improved material quality of this run (particularly in this section of the wafer).

Since the contacts were not ohmic, and the material was too resistive to give reliable data, no Hall measurements could be made on the *p*- $Al_{0.40}Ga_{0.60}N$ bulk material. In order to verify that the diodes were *p-i-n* junctions, and not

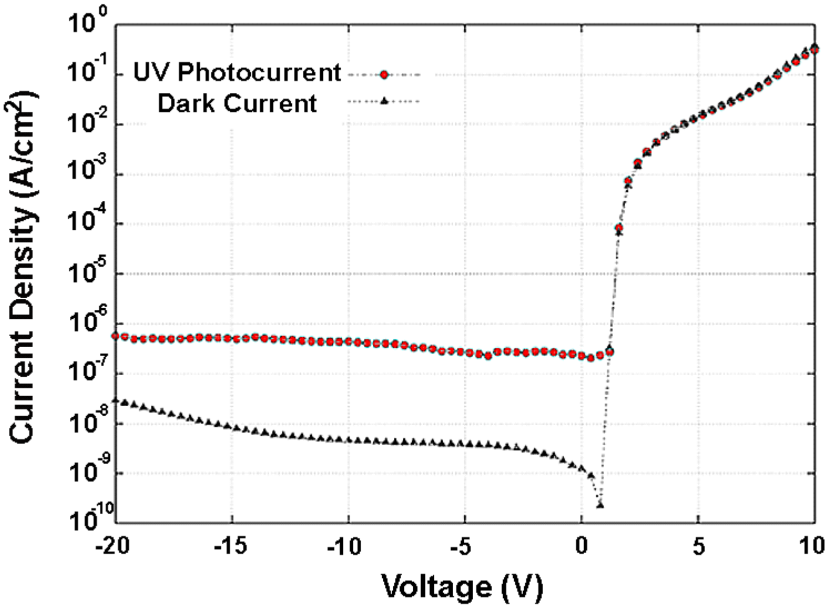

Figure 5.6: I-V characteristics showing the dark current and UV photoresponse of the a back-illuminated solar-blind photodetector.

Schottky diodes, Dr. Li measured the capacitance of nine devices of different mesa diameter and *p*-metal contact geometries. The capacitance data obtained was normalized first to the mesa cross-sectional area, and then to the *p*-metal contact area, to obtain the unit area capacitance values of Figure 5.7. The results indicate that the photodiodes were not simply Schottky diodes, because the capacitance did not scale with the area of the *p*-metal contact. On the other hand, the data scaled relatively well with the area of the mesas, suggesting that the fabricated devices were *p-i-n* junction diodes. At the time, this was taken to mean that the *p*- $Al_{0.40}Ga_{0.60}N$ layer showed *p*-type behavior forming the *p-i-n* junction.

Since this time, it was realized that the *p*-$Al_{0.40}Ga_{0.60}N$ layer was insulating, and instead it was the 20 nm-thick *p*-GaN and grading layers that were responsible for the *p-i-n* junction formation.

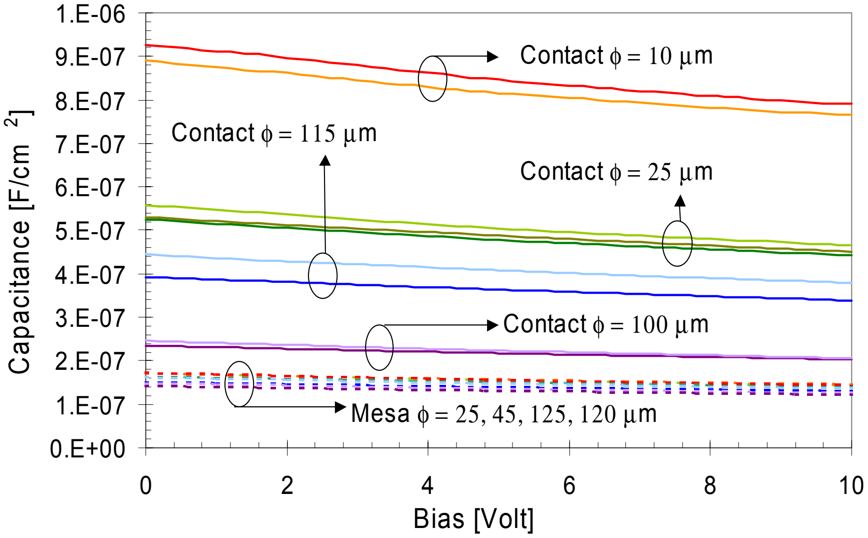

Figure 5.7: Unit area capacitance data for nine solar-blind $Al_xGa_{1-x}N$ photodetectors compared to the mesa areas and *p*-metal contact areas.

5.3 EXTERNAL QUANTUM EFFICIENCY

Moving from top-illuminated to back-illuminated device structures required a change in the external quantum efficiency setup. The light path was altered to focus the incident UV signal onto the back of a sample mounted with double-sided copper tape to a vertical aluminum sample holder. The holder was positioned so that probes could be brought in from either side to make top contact to the device. Figure 5.8 shows a ~ 25 μm-diameter beam spot illuminated through the back of the double-polished sapphire substrate onto the device. The device diameter was ~ 250 µm and had a ring *p*-contact configuration.

Figure 5.9(a) shows the external quantum efficiency of a ~ 250 µm-diameter solar-blind photodiode. The diode was biased in 10 V increments from 0 V to 60 V. The long wavelength fall-off at ~ 280 nm was due to the band gap of the $Al_{0.40}Ga_{0.60}N$ active layers. The slow roll-off on the shorter wavelength side (from 278 to 250 nm) was caused by absorption of the photons in the *n*-$Al_{0.40}Ga_{0.60}N$ region. The absorption coefficient of $Al_{0.40}Ga_{0.60}N$ is large, resulting in a large number of photons, which were transmitted through the "window" template layer, to be absorbed near the bottom of the *n*- $Al_{0.40}Ga_{0.60}N$ region. Most of the photo-induced carriers were not able to diffuse to the high-field *i*-region because the *n*- $Al_{0.40}Ga_{0.60}N$ thickness was much larger than the hole

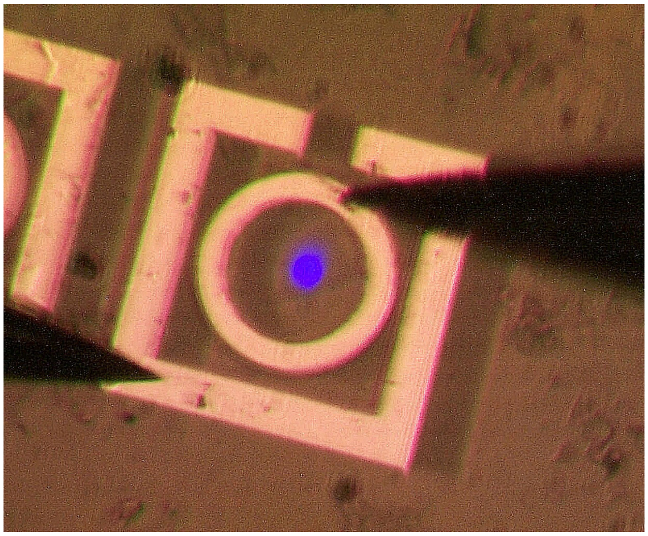

Figure 5.8: A digital photograph taken trough an optical microscope of a back-illuminated device under test on the external quantum efficiency setup.

diffusion length in $Al_{0.40}Ga_{0.60}N$. Only light that made it through the *n*-$Al_{0.40}Ga_{0.60}N$ region and was absorbed within a diffusion length of the *i*-$Al_{0.40}Ga_{0.60}N$ region was seen in the external quantum efficiency measurement. At zero bias (photo-voltaic mode), the external quantum efficiency peaked at ~ 278 nm at a value of 12%. As the device was reverse biased, and the depletion region extended into the *n*-$Al_{0.40}Ga_{0.60}N$ layer, the external quantum efficiency increased due to the absorption of more light inside the depletion region. The external quantum efficiency increased to 35% at ~ 280 nm with a 60 V reverse-bias. This number is low compared to the top-illuminated $Al_xGa_{1-x}N/GaN$ heterojunction *p-i-n* devices of Chapter 3, because a significant amount of the incident light was lost to recombination in the *n*-$Al_{0.40}Ga_{0.60}N$ layer. Figure 5.9(b) shows the corresponding responsivity data, with a peak value of 27 mA/W at 0 V and 79 mA/W at 60 V. A 3-decade UV-to-visible rejection by 400 nm is seen for all bias conditions.

It can be seen in Figure 5.9(a) that the external quantum efficiency peak red-shifts with increased bias, which is attributed to the Franz-Keldysh effect [89,90]. The wavelength dependence in the absorption coefficient (α) for direct allowed transitions and photon energy $h\nu < E_g$ is given by [89]:

$$\alpha \propto \exp\left[-\frac{4(2m_r)^{1/2}(E_g - h\nu)^{3/2}}{3\hbar e\varepsilon}\right] \tag{5.1}$$

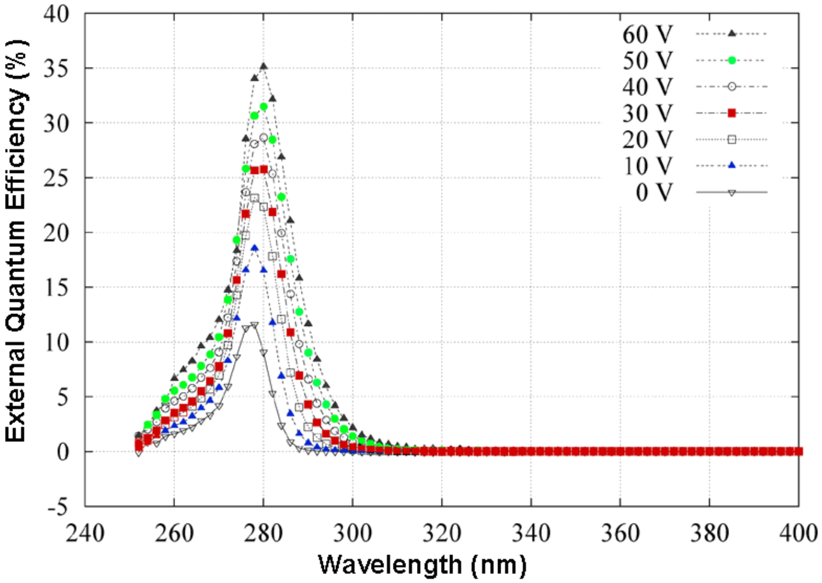

(a)

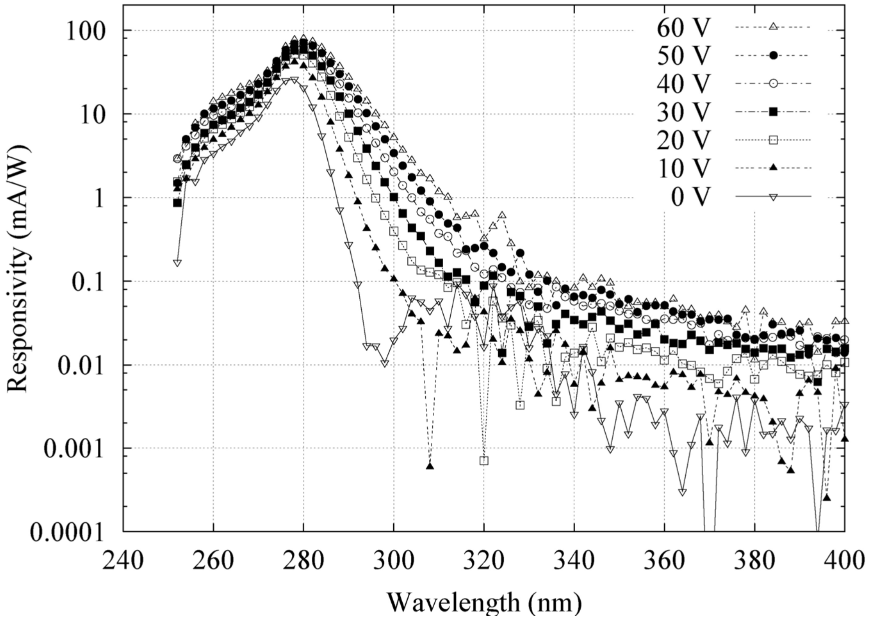

(b)

Figure 5.9: (a) Linear plot of external quantum efficiency vs. wavelength for a back-illuminated solar-blind photodiode, (b) Corresponding responsivity data on a semi-log scale.

where m_r is the reduced mass of the electron-hole pair, and ε is the electric field. In addition, there is an exponential decay in the long wavelength fall-off that is usually referred to as an Urbach tail. This below band gap response is associated with defect states in the band-gap and variations in the local material composition [91,92]. It should also be noted that there was a response from the *p*-GaN layer if the beam spot was positioned underneath the ring *p*-contact. The origin of this response is discussed in detail in Chapter 7.

5.4 NOISE AND DETECTIVITY

Characterization of noise is needed to ascertain how small of a signal the device can detect. Dr. Li used a digital signal processing (DSP) lock-in amplifier, along with a low-current Kelvin probe station, to measure the low-frequency (1 Hz to 1 kHz) noise of these photodetectors. The background noise of the system was ~ 3 ×10^{-28} A^2/Hz. The bias was varied from 0 V to -63.2 V. Figure 5.10 shows the experimental results for various reverse bias voltages. The noise spectrum at zero bias was below the noise floor of the measurement system. Least-square fits to the measured noise data showed 1/f noise characteristics:

$$S_n = {}^{S_0}\!\big/_{f^{\gamma}} \qquad (5.2)$$

where S_n is the spectral density of the noise current, S_0 is its value at 1 Hz, *f* is the frequency, and γ is a fitting parameter. The value of γ was found to vary from 0.9 to 1.2.

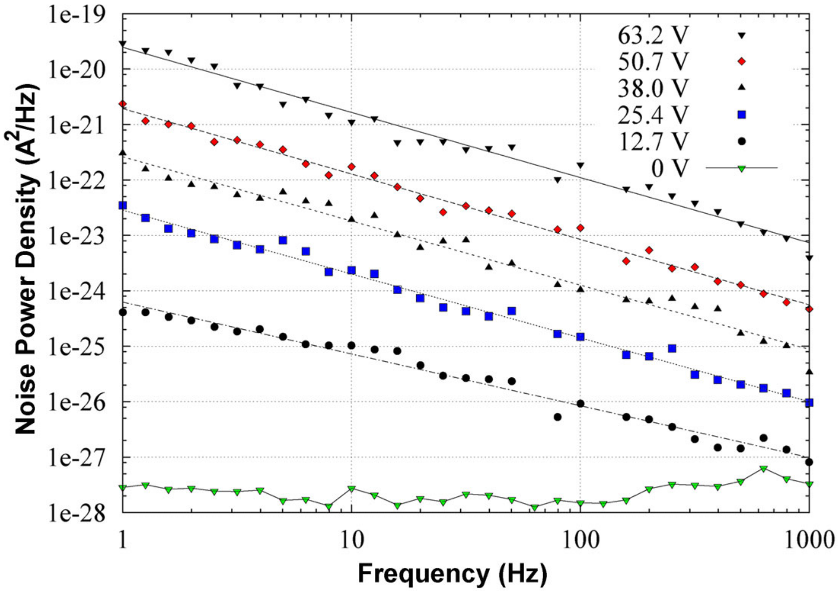

Figure 5.10: Measured low-frequency dark current noise spectra of a solar-blind $Al_xGa_{1-x}N$ photodetector at various reverse bias conditions with the corresponding 1/f fit lines.

The total squared noise current is usually estimated by integrating over the frequency range from 0 to the measured bandwidth B:

$$\left\langle i_n^{\,2} \right\rangle = \int_0^B S_n df = \int_0^1 S_0 + \int_0^B \frac{S_0}{f} df = S_0\left[\ln(B)+1\right] \tag{5.3}$$

Then the noise equivalent power (NEP) is given by:

$$NEP = \frac{\sqrt{\left\langle i_n^{\,2} \right\rangle}}{R} \tag{5.4}$$

and the Jones detectivity D^* is obtained from:

$$D^* = \frac{\sqrt{A_D B}}{NEP} = \frac{R\sqrt{A_D B}}{\sqrt{\left\langle i_n{}^2 \right\rangle}} \tag{5.5}$$

where A_D is the cross-sectional area and R is the responsivity of the photodetector.

It is advantageous to operate the photodetector close to zero bias, because with increasing bias, S_n increases much faster than R, resulting in lower D^*. An estimate for D^* near zero bias was determined by extrapolating the 1/f fits back to zero bias giving a value of ~ 1.3×10^{-28} A^2/Hz for S_0. This yields a value of 1.2×10^{-12} W for the NEP and a lower-bound of $D^* = 4.2 \times 10^{11}$ cm·Hz$^{1/2}$·W^{-1}. On the

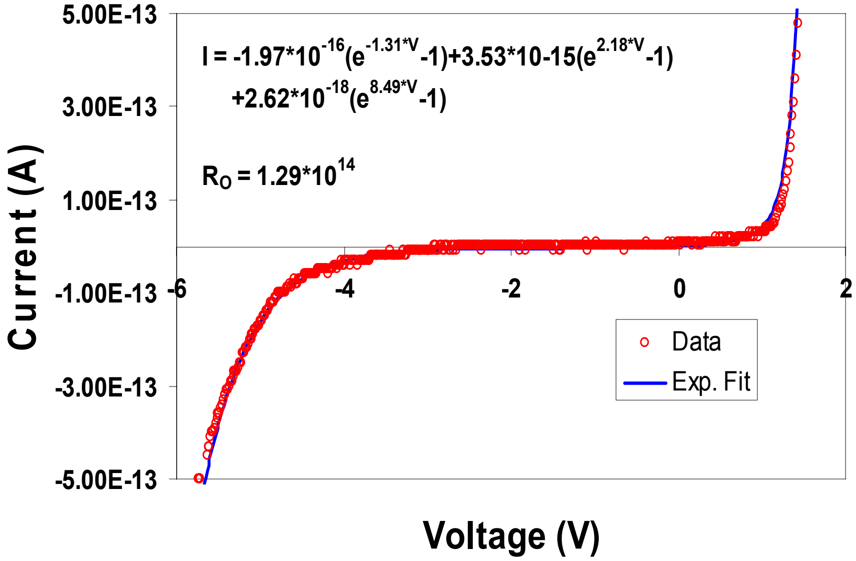

Figure 5.11: Low voltage I-V data for a 250 µm-diameter solar-blind photodetector and the curve-fitting used to extract R_0.

other hand, an upper-bound of D^* can be estimated assuming that the device is shot noise limited at zero bias and using the curve fitting method described in Section 4.5. Figure 5.12 shows the I-V data near zero bias and the curve-fitting used to estimate $R_0 = 1.29 \times 10^{14}\ \Omega$. The upper-bound of D^* was estimated to be 5.3×10^{13} cm·Hz$^{1/2}$·W^{-1}. Since S_n at zero bias was below the noise floor of any currently-available measurement apparatus, it was impossible to determine whether 1/f noise or shot noise was the dominant noise mechanism at zero bias. In the subsequent chapters we assume the devices are shot noise limited and use the curve-fitting method to calculate D^*.

5.5 SPEED

Dr. Li developed a new speed setup to measure these devices. A frequency quadrupled Nd:YAG laser with a ~ 500 ps pulse width at 266 nm was used as the excitation source for the temporal response measurements. Due to the test setup, a front-side illumination configuration was used with a ~ 10 μm beam spot. Neutral density filters were used to decrease the laser beam intensity to ~ 10 nJ/pulse. The photo-induced electrical pulse was coupled through a high bandwidth bias-tee to a 500 MHz oscilloscope with a 50 Ω input impedance.

The pulse response data indicates that the speed of the measured devices is RC-time limited. The slow ring in the tail was confirmed to be a result of the measurement circuit. As seen in Figure 5.12, these devices showed a strong dependence on the spatial position of the light source. The photoresponse becomes slower when the laser beam is moved from near the ring *p*-contact to the center of the mesa, even though the DC photocurrent is insensitive to the beam position. This is attributed to the large lateral resistivity of high Al percentage *p*-type $Al_xGa_{1-x}N$ layers.

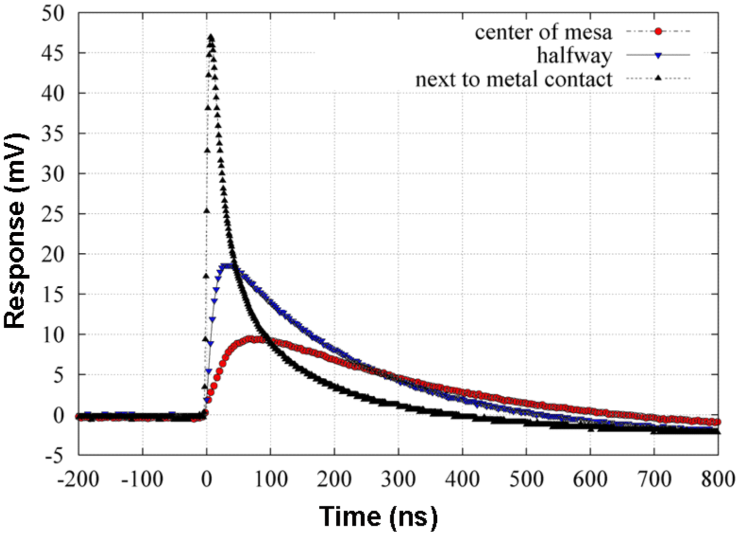

Figure 5.12: Pulse-response data at -15 V for a solar-blind photodetector with varied beam position compared to ring contact.

5.6 SUMMARY

The group's first back-illuminated solar-blind $Al_xGa_{1-x}N$ photodetectors were designed, fabricated, and characterized. These devices showed low dark current densities, ~ 5 nA/cm^2 at -10 V, and high forward bias currents, ~ 0.3 A/cm^2 at 10 V. The peak external quantum efficiency at zero bias was ~ 12% at λ = 278 nm (R = 27 mA/W). This resulted in a thermal noise limited detectivity of $D^* = 5.3 \times 10^{13}$ cm·Hz$^{1/2}$·W^{-1}. New device designs were needed to increase the zero bias external quantum efficiency, and thus, increase the overall detectivity.

6. “Window” *n*-region $Al_xGa_{1-x}N$ *p-i-n* photodetectors

6.1 INTRODUCTION

In Chapter 5 the first solar-blind photodetectors are discussed. The design consisted of a *p-i-n* $Al_{0.40}Ga_{0.60}N$ homojunction photodetector. The high absorption coefficient ($>10^5$) of the *n*-$Al_{0.40}Ga_{0.60}N$ layer, resulted in significant absorption of the incident light that was transmitted through the template layer. Since the diffusion length of holes in *n*-$Al_{0.40}Ga_{0.60}N$ is very short compared to the *n*-$Al_{0.40}Ga_{0.60}N$ layer thickness, most of the photo-induced carriers are lost to recombination. Only the small percentage of photons that reach the high-field *i*-region are collected and seen in the external quantum efficiency. To improve the external quantum efficiency, the intensity of light reaching the *i*-region must be increased. To achieve this, the *n*-$Al_{0.40}Ga_{0.60}N$ layer thickness can be reduced in an attempt to limit the amount of absorption in this layer. The problem with this approach is that reducing the thickness greatly increases the lateral resistance, which creates a non-uniform electric field and reduces the collection efficiency of the photodetector. In addition, with such a large absorption coefficient for $Al_{0.40}Ga_{0.60}N$, a significant percentage of the incident light will be absorbed even with a very thin layer. Another approach to increase the intensity of light reaching the high-field *i*-region is to increase the percentage of aluminum in the *n*-region, creating a “window” for the wavelengths of interest. Like the “window” template layer, if the aluminum percentage in the *n*-region is increased compared to the percentage in the *i*-region, certain wavelengths of light will be transmitted to the *i*-region with minimal absorption in the *n*-region. In fact, ideally the *n*-region should have the same aluminum percentage as the template layer, thus extending the "window" region from the substrate to the *i*-region.

The problem with growing a good "window" *n*-region arises when attempting to dope the high aluminum percentage *n*-regions with Si. As discussed in Section 2.2, the Si dopant level gets deeper as the aluminum percentage is increased, thus decreasing the amount of activated carriers at room temperature. This effect alone cannot explain the sudden drop in activated Si dopants as the aluminum composition approaches 50%. Hall measurements of $Al_xGa_{1-x}N$ layers, with x in the range 0.40 to 0.55, showed a large drop in free carriers at approximately x ~ 0.50. By increasing x to 0.55, attempts to do Hall measurements failed, which suggests that the layers were insulating even with 10^{20} Si dopants incorporated into the layer. This limited the amount of aluminum that could be used in the *n*-regions to 50%. Although this doping problem is not well understood, an explanation is proposed in Section 7.1.

The "window" *n*-region of the solar-blind photodetector was limited to 50% aluminum concentration as discussed above. To investigate the effect of the *n*-region aluminum composition compared to the *i*-region aluminum concentration, two device structures were designed. The first was a solar-blind structure, with an $Al_{0.41}Ga_{0.59}N$ *i*-region, and an $Al_{0.50}Ga_{0.50}N$ "window" *n*-region to try and increase the external quantum efficiency. The second was a visible-blind device, with an $Al_{0.27}Ga_{0.73}N$ *i*-region, and an $Al_{0.50}Ga_{0.50}N$ "window" *n*-region. The visible-blind device had a significant difference in the aluminum percentage between the *i*-region and *n*-region in order to further investigate the properties of the "window" *n*-region.

By using a back-illuminated photodiode design, the problem of the "optical dead space" region, in which photogenerated carriers near the surface of a typical top-illuminated structure recombine before they can be collected, is eliminated [93]. In addition, we use a dot *p*-contact that covers most of the mesa to achieve lower contact resistance and avoid the field-crowding problem previously reported for ring devices [76]. For these devices a *p*-GaN cap layer was used to improve our *p*-contact. These devices showed no response from this thin GaN region. It is assumed that the band offset between the *p*-GaN cap layer and the *p*-AlGaN layer effectively blocked the diffusion of photogenerated carriers from the GaN layer [94].

6.2 MATERIAL GROWTH AND DEVICE FABRICATION

A schematic cross-section of the two devices is depicted in Figure 6.1. The *p-i-n* structure consisted of $Al_xGa_{1-x}N$ device layers grown by low-pressure metalorganic chemical vapor deposition (MOCVD) in an EMCORE Model D125 UTM rotating disk reactor on two-inch diameter c-plane (0001) double-polished sapphire substrates. Growth begins with an AlN buffer layer followed by a thick $Al_{0.60}Ga_{0.40}N$ template layer that was designed to improve the subsequent device layers by limiting the defect density. Device layers were grown starting with a 20 nm-thick graded *n*-layer from $Al_{0.60}Ga_{0.40}N$ to $Al_{0.50}Ga_{0.50}N$. This was followed by a *p-i-n* structure consisting of a 200 nm-thick $Al_{0.50}Ga_{0.50}N$ *n*+-layer, a 150 nm-thick $Al_xGa_{1-x}N$ unintentionally doped (Nd ~ 10^{15} cm^{-3}) absorption region,

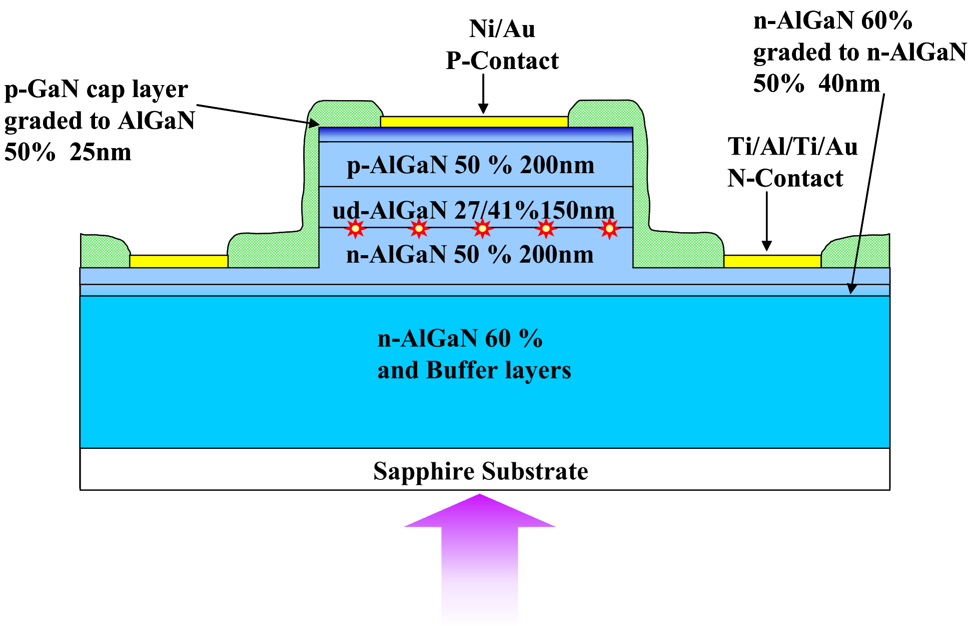

Figure 6.1: Schematic cross-section of both $Al_xGa_{1-x}N$ devices.

and a 200 nm-thick $Al_{0.50}Ga_{0.50}N$ *p*-layer. The first device grown had an $Al_{0.41}Ga_{0.59}N$ (solar-blind) absorption region while the second had an $Al_{0.27}Ga_{0.73}N$ (visible-blind) absorption region. To insure a good *p*-contact without cracking, a 10 nm-thick graded layer from the *p*- $Al_{0.50}Ga_{0.50}N$ to *p*-GaN was grown along with a 10 nm-thick *p*-GaN cap layer. An insitu-anneal was performed to activate the magnesium *p*-dopant. Standard processing, as described in Section 2.3, was used to define mesas and deposit Ti/Al/Ti/Au *n*+-contacts and Ni/Au *p*-contacts.

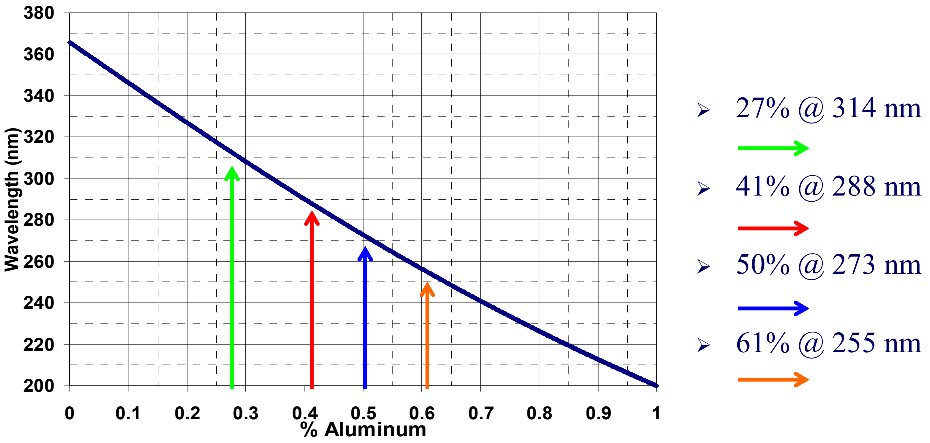

Figure 6.2: Wavelength vs. aluminum percentage for the $Al_xGa_{1-x}N$ material system.

Figure 6.2 shows a graph of the wavelength vs. aluminum percentage for the $Al_xGa_{1-x}N$ material system. The arrows indicate the position of the four $Al_xGa_{1-x}N$ device layers found in the two devices described above. To get the wavelength dependence, the band-gap (E_g) was first calculated using the relation:

$$E_g = x \cdot E_{AlN} + (1-x) \cdot E_{GaN} + b \cdot x(1-x) \qquad 6.1$$

where x is the aluminum percentage and b = -1 is the bowing parameter [75]. The band-gap was then converted to wavelength using the standard equation:

$$\lambda = \frac{h \cdot c}{E_g} \qquad 6.2$$

where h is Planck's constant, c is the speed of light, and λ is the corresponding wavelength. From this graph we can see that the solar-blind device, with an

$Al_{0.41}Ga_{0.59}N$ *i*-region, should have a peak response at ~ 288 nm, while the visible-blind device, with an $Al_{0.27}Ga_{0.73}N$ *i*-region, should have a peak response at ~ 314 nm. The "window" $Al_{0.60}Ga_{0.40}N$ template layer should transmit light with wavelengths > 255 nm, while the "window" $Al_{0.50}Ga_{0.50}N$ *n*-region should transmit wavelengths > 273 nm. Thus we expect the solar-blind detector to have a response from 273 – 288 nm, and the visible-blind detector to have a response from 273 – 314 nm.

6.3 ELECTRICAL CHARACTERIZATION

Figure 6.3 (a) and (b) show the reverse bias I-V characteristics for the solar-blind photodetector and visible-blind photodetector, respectively. Both devices showed leaky dark currents in excess of 1×10^{-8} A/cm^2 for a 250 µm-diameter device near zero bias. At 5 V reverse bias the dark current increased to 1×10^{-4} A/cm^2. The ultraviolet photocurrent showed a strong response at zero bias, but was quickly overtaken by the dark current with just a few volts reverse bias. Thus, only low reverse bias external quantum efficiency measurements were obtained.

6.4 EXTERNAL QUANTUM EFFICIENCY

In Chapter 5 solar-blind photodetectors with external quantum efficiency of ~ 35% at 280 nm at 60 V reverse bias were discussed [93,95]. As discussed earlier, this high bias was required because the *i*-region and *n*-region both had the same composition of aluminum and thus absorption occurred at the *n*-region/template layer interface instead of in the *i*-region. In order to achieve higher external quantum efficiency at low bias the aluminum composition of the

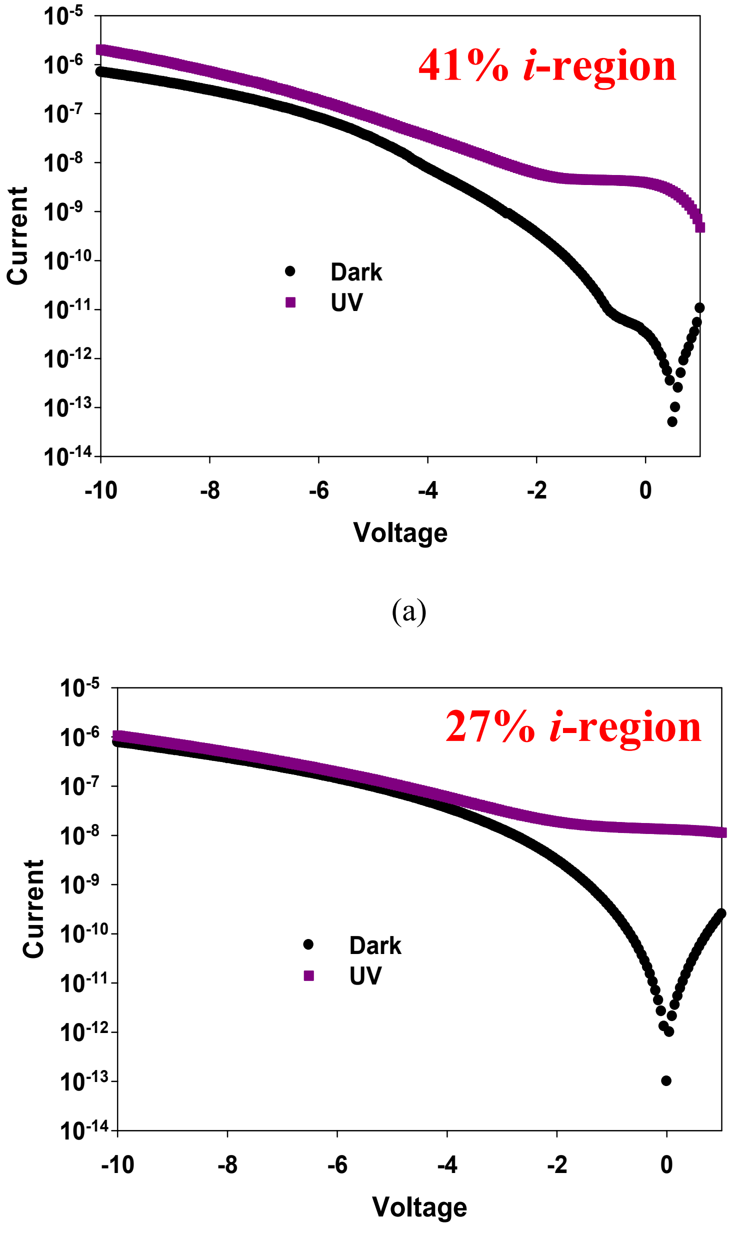

(a)

(b)

Figure 6.3: Dark current and UV photoresponse of : (a) $Al_{0.41}Ga_{0.59}N$ *i*-region solar-blind detector, (b) $Al_{0.27}Ga_{0.73}N$ *i*-region visible-blind detector.

n-region was increased to create a "window" *n*-region. Back-illuminated heterostructure *p-i-n* devices were previously reported by W. Yang et. al. [52] with $Al_{0.27}Ga_{0.73}N$ "window" *n*-regions and GaN *i* and *p*-regions. They achieved zero bias external quantum efficiencies of ~ 50% at 355 nm.

Dot contact devices were used for back-illuminated external quantum efficiency measurements using a procedure described previously in Section 2.5. By using an $Al_{0.27}Ga_{0.73}N$ absorption region visible-blind photodetectors with a broad band of high external quantum efficiency from 280 nm to 310 nm were achieved as seen in Figure 6.4 (b). At zero bias the peak external quantum efficiency was ~ 53% at λ = 290 nm and ~ 54% at λ = 302 nm. At 5 V reverse bias, the photodetector had peak external quantum efficiencies of ~ 64% at both λ = 290 nm and λ = 302 nm. The external quantum efficiency curves are plotted with transmission data taken through an unprocessed sample on a Perkin Elmer Lambda 9 spectrometer. Consistent with the external quantum efficiency measurements, steps in the transmission data were seen at 360 nm, due to the GaN cap layer, and at the absorbtion edge of the *i*-region. It is interesting to note that the zero bias external quantum efficiency of the $Al_{0.27}Ga_{0.73}N$ photodiodes is 44% at λ = 279 nm.

In order to achieve solar-blind photodetectors it was necessary to shift the long wavelength cutoff to 290 nm. This was accomplished by increasing the *i*-region aluminum percentage from $Al_{0.27}Ga_{0.73}N$ to $Al_{0.41}Ga_{0.59}N$, while still keeping the aluminum percentage less than the $Al_{0.50}Ga_{0.50}N$ "window" *n*-region. Solar-blind photodetectors were realized with a narrow peaked response shown in

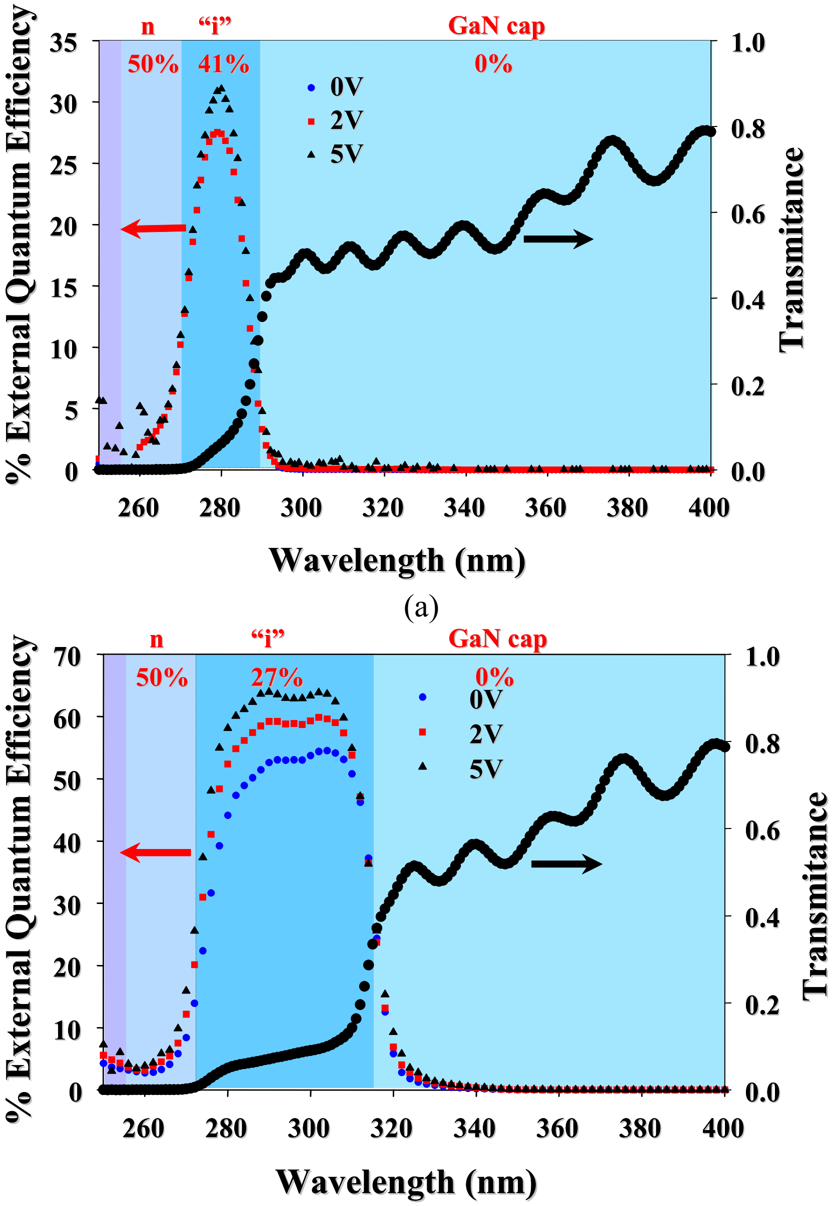

(a)

(b)

Figure 6.4: External quantum efficiency and transmission data for: (a) $Al_{0.41}Ga_{0.59}N$ *i*-region solar-blind detector, (b) $Al_{0.27}Ga_{0.73}N$ *i*-region visible-blind detector.

Figure 6.4 (a). A peak external quantum efficiency at zero bias of ~ 26% was achieved at λ = 279 nm. At 5 V reverse bias the external quantum efficiency increased to ~ 32%. This corresponds to reponsivities of R_λ = 0.058 A/W at zero bias and R_λ = 0.070 A/W at –5 V. The transmission data for this device also showed the 360 nm step due to the GaN cap layer and a lower wavelength step corresponding to the external quantum efficiency peak. The peak response of the solar-blind photodetector was much lower than the response of the visible-blind photodetector at the same wavelength. It was assumed that this was due to material quality degradation with the increased aluminum percentage.

6.5 MODELING OF THE EXTERNAL QUANTUM EFFICIENCY

Carriers generated in the *n*-region near the *n*-region/template layer interface are not seen in the external quantum efficiency results of Figure 6.4. It was assumed that this was due to the short diffusion length of holes in $Al_xGa_{1-x}N$, which leads to recombination of the photo-generated carriers in the *n*-region. The absence of *n*-region response supports the assumption that only photons that made it to the *i*-region were detected. To further investigate this assumption, we grew an identical sample to the photodetectors described above except that the growth was terminated after the $Al_{0.50}Ga_{0.50}N$ *n*-region. The transmission data of this sample was then compared to the zero bias external quantum efficiencies of the photodetectors as seen in Figure 6.5. The short wavelength cut-off of the detectors aligns well with the transmission data of the $Al_{0.50}Ga_{0.50}N$ *n*-region. This further supports the assumption that only photons that are transmitted through the $Al_{0.50}Ga_{0.50}N$ *n*-region, to the *i*-region, contribute to the photocurrent.

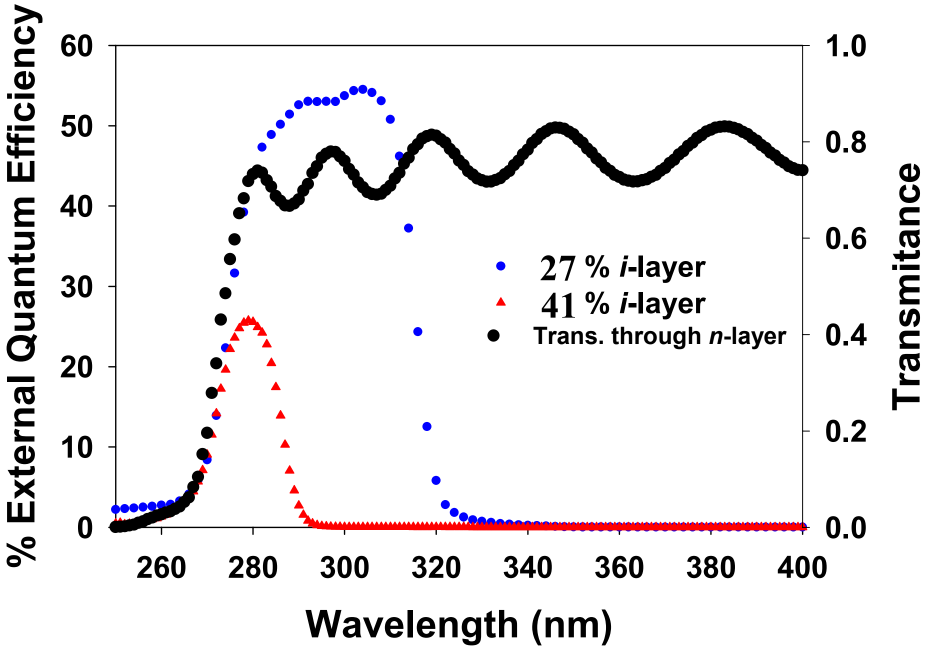

Figure 6.5: Zero bias external quantum efficiencies for both the solar-blind and visible-blind detector compared to the transmission data through an *n*-layer.

Standard models for external quantum efficiency of *p*-*i*-*n* structures assume a top-illuminated device structure with absorption and diffusion in both the *p* and *n*-regions, as well as absorption in the depleted *i*-region [96-98]. For a back-illuminated $Al_xGa_{1-x}N$ device structure, with a large absorption coefficient ($>10^5$), the majority of the absorption will be in the *n* and *i*-regions, and thus the *p*-layer absorption was assumed to be zero. In addition, it was assumed that the light absorbed in the *n*-region was lost due to recombination (as discussed above). Thus, only light that was transmitted through the *n*-region and absorbed in the *i*-region contributed to the external quantum efficiency. To model the external quantum efficiency, the transmission data of the $Al_{0.50}Ga_{0.50}N$ *n*-region (T_n) was used as an approximation of the light intensity reaching the *i*-layer. The absorption in the *i*-region was then modeled using:

$$\eta(\lambda) = T_n \cdot \eta_i (1 - e^{-\alpha(\lambda)\cdot x_i}) \qquad 6.3$$

where $\eta(\lambda)$ is the external quantum efficiency, T_n is the transmission data for the $Al_{0.50}Ga_{0.50}N$ *n*-region, η_i is the internal quantum efficiency, and x_i is the *i*-region thickness. The wavelength dependent absorption coefficient, $\alpha(\lambda)$ is given by:

$$\alpha(\lambda) = \alpha_O \cdot (E(\lambda) - E_g)^{1/2} \qquad 6.4$$

where α_O is the absorption constant (5×10^5), $E(\lambda)$ is the photon energy as a function of wavelength, and E_g is the band-gap of the *i*-layer as calculated from equation 6.1.

Using a Mathcad code with the above equations, the external quantum efficiencies were simulated. The internal quantum efficiency (η_i) was used to adjust the external quantum efficiency peak to fit the measured data. Figure 6.6 (a) and (b) show the external quantum efficiency with the modeled curve fit for the solar-blind and visible-blind photodetectors, respectively. The solar-blind photodetector is fit very well with this model using an internal quantum efficiency of η_i = 36%. The visible-blind detector is fit reasonably well, with an internal quantum efficiency of η_i = 70%. The oscillations in the modeled fit arise from the $Al_{0.50}Ga_{0.50}N$ *n*-region transmission data, and do not line up with the external

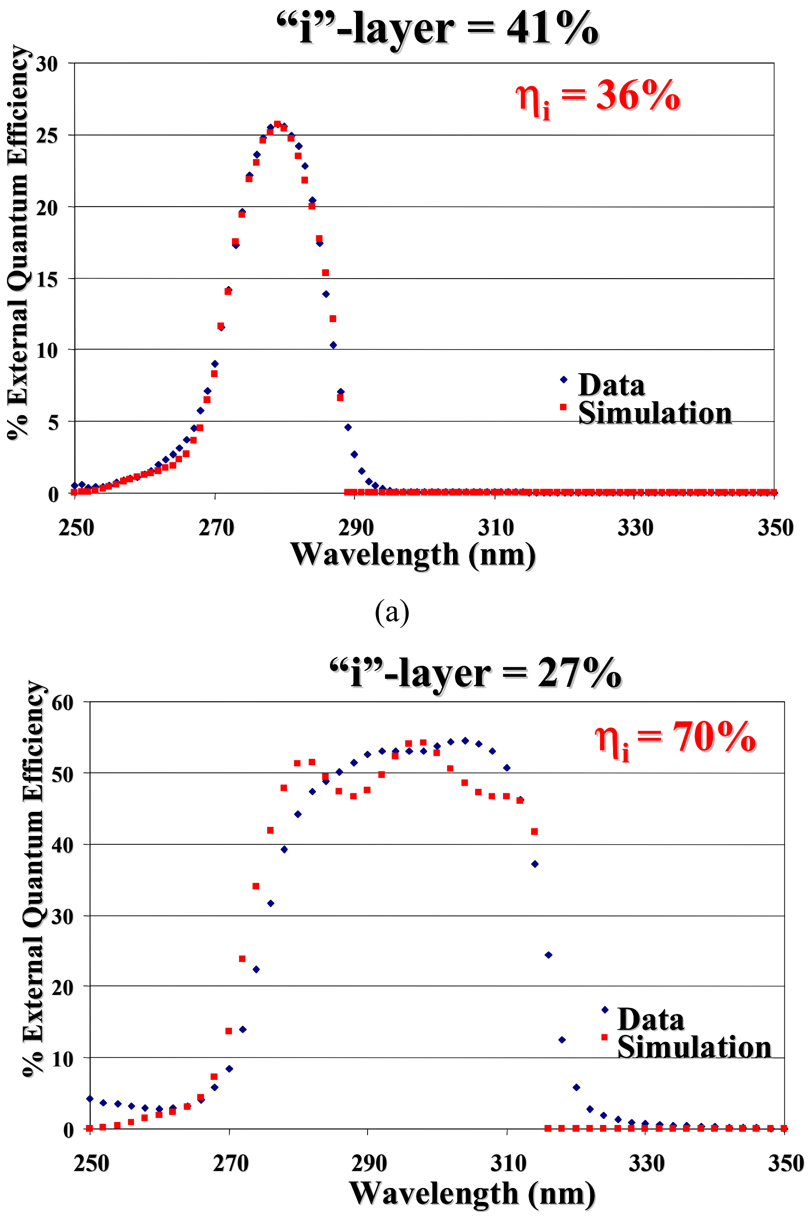

(a)

(b)

Figure 6.6: External quantum efficiency and model simulation for: (a) $Al_{0.41}Ga_{0.59}N$ *i*-region solar-blind detector, (b) $Al_{0.27}Ga_{0.73}N$ *i*-region visible-blind detector.

quantum efficiency due to thickness variations and the existence of a second air interface directly after the *n*-region in the transmission data.

The transmission data fits the short wavelength cut-off very well, while the long wavelength cut-off is fit well by the absorption of the *i*-region. It was realized at this point that since there is not a sharp transition in the transmission spectrum of the *n*-region, or the absorption spectrum of the *i*-region, the overlap of the two is very important. The external quantum efficiency of the solar-blind photodetectors was limited not only by the internal quantum efficiency, but also by the overlap of the *n*-region transmission curve and the *i*-region absorption curve. This overlap can be controlled by the difference in the aluminum percentage of the *n* and *i*-regions. If the percentages of the two layers are too close together, the rising transmission curve will be cut off by the falling absorption curve, which limits the external quantum efficiency. This issue is discussed more in depth in Chapter 7.

6.6 DETECTIVITY

High zero bias external quantum efficiency is desired not only for read-out circuit requirements but also for the low noise these wide-bandgap devices have near zero volts [93]. To further examine the current near zero bias, an HP 4156B parameter analyzer was used with low-noise probes. As discussed earlier in this chapter, these devices had large dark currents at low reverse bias that were not fit well with exponential curve fits. Instead, curve fitting was performed using a 5th order polynomial to fit both the forward and reverse bias curves near zero bias.

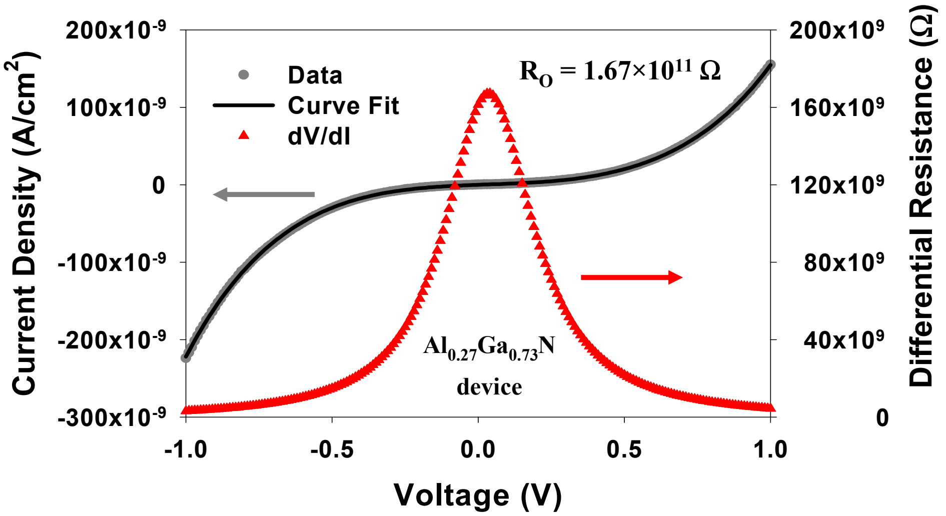

Figure 6.7: Linear plot of I-V data near zero bias, 5th order polynomial fit and differential resistance for the visible-blind $Al_{0.27}Ga_{0.73}N$ *i*-region device.

As described in Section 4.5, this method often gives poor results for photodiodes that have low dark currents. These photodiodes, however, had large dark currents, resulting in symmetric forward and reverse dark current characteristics near zero bias. Exponential curve fitting did not work well with the large dark current, and it was found that reliable curve fits could be obtained with a 5th order polynomial. The derivative of the equation obtained from curve fitting was then used to find the differential resistance, R_O, at zero bias [84].

Figure 6.7 shows this process for the $Al_{0.27}Ga_{0.73}N$ visible-blind device. For these fits $R_0 = 1.67\times10^{11}\ \Omega$ was obtained for the $Al_{0.27}Ga_{0.73}N$ visible-blind device and $R_0 = 2.98\times10^{11}\ \Omega$ was obtained for the $Al_{0.41}Ga_{0.59}N$ solar-blind device. Taking the device diameter to be 240 µm, R_0A was calculated to be $7.55\times10^7\ \Omega\cdot cm^2$ for the $Al_{0.27}Ga_{0.73}N$ device and $1.35\times10^8\ \Omega\cdot cm^2$ for the

$Al_{0.41}Ga_{0.59}N$ device. The responsivity was calculated using the zero bias external quantum efficiency at the peak wavelength. Using this and the device area, the detectivity, D^*, was estimated, assuming that the primary noise source was thermal noise as previously discussed in Section 4.5. For the $Al_{0.27}Ga_{0.73}N$ visible-blind device peak detectivities of $D^* = 8.40\times10^{12}$ $cm\cdot Hz^{1/2}\cdot W^{-1}$ at $\lambda = 290$ nm and $D^* = 9.05\times10^{12}$ $cm\cdot Hz^{1/2}\cdot W^{-1}$ at $\lambda = 302$ nm were found. For the $Al_{0.41}Ga_{0.59}N$ solar-blind device a peak detectivity of $D^* = 5.30\times10^{12}$ $cm\cdot Hz^{1/2}\cdot W^{-1}$ at $\lambda = 279$ nm was found.

This solar-blind detectivity is an order of magnitude less than was achieved for the first solar-blind detector described in Section 5.4. Even though the zero bias external quantum efficiency was doubled from 12% to 26 %, the differential resistance fell from $R_0 = 1.29 \times10^{14}\ \Omega$ for the first solar-blind device, to $R_0 = 2.98\times10^{11}\ \Omega$ for the current solar-blind photodetector. The differential resistance is greatly affected by the dark current, and since the current devices showed large dark currents near zero bias, they have a much lower differential resistance. Examining Equation 4.5 shows that the three order of magnitude drop in differential resistance reduced the overall detectivity more than the increase that resulted from doubling the external quantum efficiency. Thus, a low dark current is as important as an increased external quantum efficiency.

6.7 ULTRAVIOLET LIGHT EMITTING DIODE

There is a growing interest in compact ultraviolet light sources for possible applications such as chemical sensors, conversion to white light using a phosphor, and optical data storage [99-102]. It has been very difficult to achieve ultraviolet light emitters due to the material quality issues associated with increased aluminum percentage discussed at various points in this dissertation. The $Al_{0.27}Ga_{0.73}N$ *i*-region visible-blind photodetectors were forward biased and found to emit UV radiation.

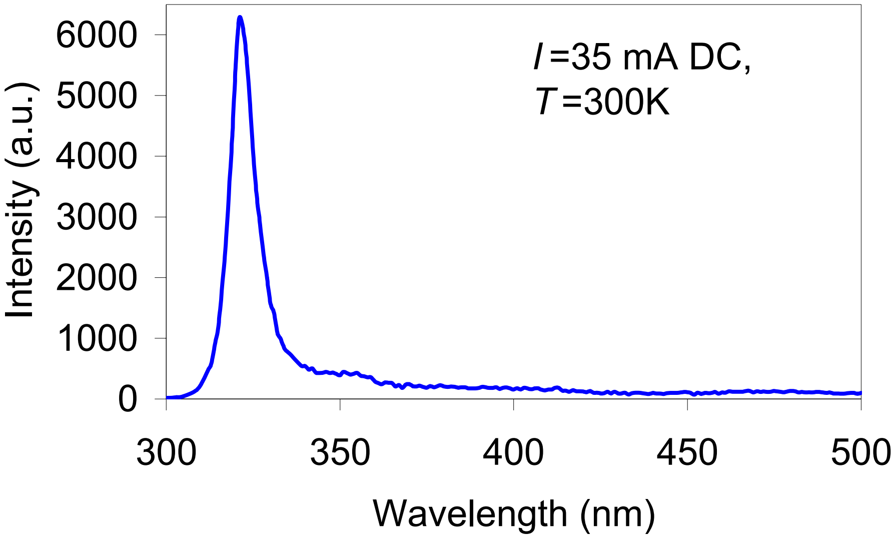

Figure 6.8: Electroluminescence spectrum at 300 K for a visible-blind photodetector.

Figure 6.8 shows the electroluminescence spectrum for a typical LED at I = 35 mA DC (65.4 A/cm^2) [103]. The electroluminescence of these photodiodes has a narrow line width (7.7 nm) peak at λ = 321 nm, which should correspond to an *i*-region with 21% aluminum. As described above, the visible-blind detector had an $Al_{0.27}Ga_{0.73}N$ *i*-region, which suggests a red shift in the LED output. This red shift can be due to heating in the LED from large contact and *p*-layer resistances or due to emission through defects in the band gap. The ultraviolet output power at 35 mA DC was measured to be ~ 39 nW using a calibrated UV-enhanced Si photodiode placed against the back-side of the double-polished sapphire substrate to collect as much light as possible. Several diodes produced output powers in this range. Due to the high series resistance, higher DC drive currents produced increased heating, with only a slight increase in light output.

6.8 SUMMARY

By decreasing the composition of aluminum in the absorption region, the "window" *n*-layer structure has been used to achieve high external quantum efficiencies at low bias. With an $Al_{0.27}Ga_{0.73}N$ absorption region, visible-blind photodetectors with high external quantum efficiency of 53% at $\lambda = 290$ nm and 54% at $\lambda = 302$ nm for zero bias and 64% at both $\lambda = 290$ nm and $\lambda = 302$ nm for 5 V reverse bias. Also designed was an $Al_{0.41}Ga_{0.59}N$ absorption region solar-blind detector with high external quantum efficiency of 26% at $\lambda = 279$ nm for zero bias and 32% at 5 V reverse bias. Fifth order polynomial curve-fits were used to calculate the differential resistance, R_0 (Ω). With R_0, the device area, and the external quantum efficiency at zero volts, the detectivity, D^*, was estimated. For the $Al_{0.27}Ga_{0.73}N$ visible-blind devices a detectivity of $D^* = 8.40\times10^{12}$ $cm\cdot Hz^{1/2}\cdot W^{-1}$ at $\lambda = 290$ nm and $D^* = 9.05\times10^{12}$ $cm\cdot Hz^{1/2}\cdot W^{-1}$ at $\lambda = 302$ nm was achieved. For the $Al_{0.41}Ga_{0.59}N$ solar-blind devices a detectivity of $D^* = 5.30\times10^{12}$ $cm\cdot Hz^{1/2}\cdot W^{-1}$ at $\lambda = 279$ nm was achieved. The drop in detectivity, compared to the first solar-blind detectors, is attributed to the large leakage current causing a significant decrease in the differential resistance.

7. High Detectivity $Al_xGa_{1-x}N$ Solar-Blind Photodetectors

7.1 INTRODUCTION

Back-illuminated GaN/$Al_xGa_{1-x}N$ *p-i-n* structures are typically grown with the *n*-side adjacent to the transparent sapphire substrate in order to limit Mg diffusion during *p*-layer growth [104-108]. As discussed in the previous chapter, the aluminum percentage in the template layer must be high enough to allow good transmission in the wavelength range of interest, but low enough to limit strain in the subsequent device layers. With proper design, the signal passes with little attenuation into the *n*-layer. The external quantum efficiency is affected by the overlap of the transmission spectrum of the *n*-region and the absorption spectrum of the *i*-region. If the aluminum percentages are too close together, then the transmission spectrum of the *n*-region will not reach its peak before it overlaps the absorption spectrum of the *i*-region. Thus, if significant absorption occurs in the *n*-layer, the external quantum efficiency at low bias will suffer even though the *i*-region may have high internal quantum efficiency. The aluminum percentage of the *i*-region cannot be decreased below 45% since it is determined by the solar-blind requirement. One approach to increase the intensity of UV radiation that reaches the *i*-region is to increase the aluminum percentage of the *n*-region creating a better “window”.

7.1 MATERIAL GROWTH AND DEVICE FABRICATION

For solar-blind photodetectors, in order to achieve adequate transmission into the *i*-region, $Al_xGa_{1-x}N$ *n*-type layers with $x \geq 0.6$ are required. However, initially it was difficult to achieve high *n*-type doping in $Al_xGa_{1-x}N$ window layers with $x > 0.5$ due to material quality issues [110-112]. Previously, we have achieved $Al_xGa_{1-x}N$ *n*-regions with $0.5 < x < 0.55$ that transmitted a limited spectrum of light into the *i*-region (Chapter 6), but these layers were very resistive. Recently, $Al_{0.6}Ga_{0.4}N$ *n*-regions have been achieved using an indium codoping technique. These *n*-regions allow increased transmission of photons into the depletion region, which results in higher zero bias external quantum efficiency.

The problem with growing a good "window" *n*-region arises when attempting to dope the high aluminum percentage *n*-regions with Si. As discussed in Sections 2.2 and 6.1, the Si dopant level gets deeper as the aluminum percentage is increased, thus decreasing the amount of activated carriers at room temperature. It has been seen from Hall measurements that there is a large drop in activated Si dopants as the aluminum percentage is increased above 50%. The Si dopant level alone cannot explain this effect.

To push the *n*-region aluminum percentage even higher a new approach was needed. The III-nitride crystal growers in Professor Dupuis' group (U. Chowdury, M. Wong) realized that it was possible to obtain $Al_{0.60}Ga_{0.40}N$ *n*-regions with good material qualities by codoping the *n*-region with both Si and In. This effect has been previously reported for $Al_xGa_{1-x}N$ with limited success [113], and was also a successful method when Si doping GaAs [114]. This allowed us to increase the aluminum percentage of the "window" *n*-region to $Al_{0.60}Ga_{0.40}N$ before the sudden drop off in carrier density was seen again for $x > 0.60$.

Oxygen levels in $Al_xGa_{1-x}N$ layers have always been important. For low aluminum concentration $Al_xGa_{1-x}N$, oxygen is a donor with a level deeper than Si, and contributes to the as-grown *n*-type nature of the $Al_xGa_{1-x}N$. Aluminum and oxygen react strongly, resulting in an increase in the oxygen level incorporated in the crystal with increased aluminum percentage. It has been suggested by C. Stampfl et. al. [115] that the oxygen impurity in $Al_xGa_{1-x}N$ undergoes a DX transition at x ~ 0.45, transforming the oxygen from a donor to an O^{3-} deep level. As this transition occurs, the triple acceptor oxygen deep level can compensate up to three Si dopants per oxygen atom. This leads to a sharp drop in the activated Si atoms, and thus a sudden drop in carrier concentration. To limit this effect the oxygen levels in the reactor and gas sources should be keep as low as possible. When using the codoping method, the In dopants may more readily bind to the oxygen deep levels, allowing the Si donor atoms to be activated.

Stampfl et. al. [115] also suggested that the formation energy of aluminum vacancies ($V^{3-}{}_{Al}$) and gallium vacancies ($V^{3-}{}_{Ga}$) becomes lower as the aluminum concentration is increased. At x ~ 0.4, both cation vacancies have very low formation energies in *n*-type material. The low formation energy of both cation vacancies, and the fact that each is a triple acceptor, suggests that these defects will increasingly compensate the *n*-type conductivity in $Al_xGa_{1-x}N$ with increasing x, especially for N-rich conditions. Thus, the In codoping could also be filling the aluminum ($V^{3-}{}_{Al}$) and gallium vacancies ($V^{3-}{}_{Ga}$) with In, which would reduce the compensation of Si dopants. In addition, the indium vacancy ($V^{3-}{}_{In}$) most likely also has a low formation energy, and could contribute to the doping barrier seen at x ~ 0.6. Further investigation is needed to determine the reason for increased doping efficiency with the In codoping technique and the observed doping barriers.

Two device structures were designed for improved solar-blind photodetectors. Figure 7.1 shows a schematic cross-section of a typical device. The first device structure has an $Al_{0.48}Ga_{0.52}N$ *i*-region, designed to have a true solar-blind response. For the second device structure, the aluminum percentage in the *i*-region was slightly decreased to $Al_{0.45}Ga_{0.55}N$. This should increase the separation in aluminum percentage of the *n* and *i*-regions, and thus improve the external quantum efficiency.

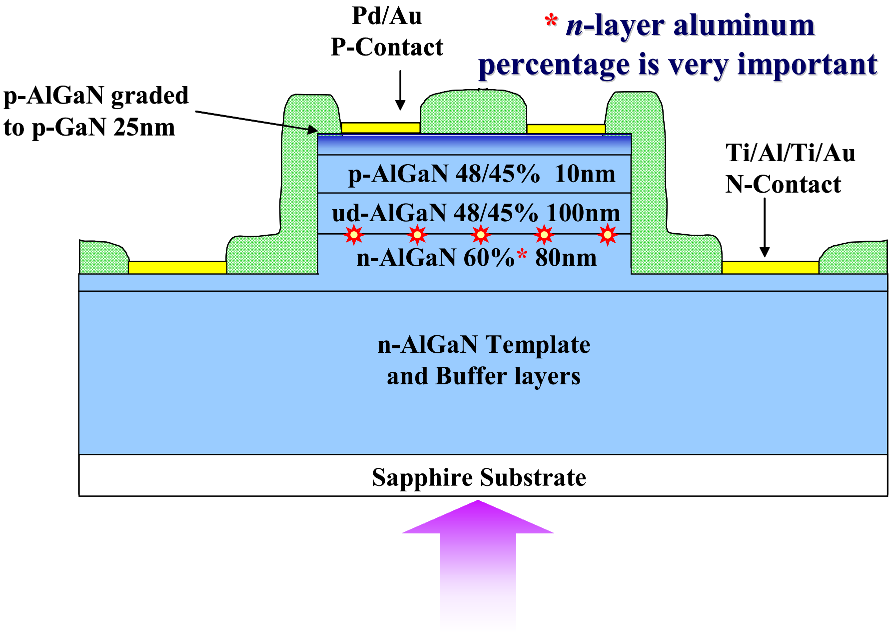

Figure 7.1: Schematic cross-section of a high detectivity solar-blind detector.

Growth began with an AlN low temperature buffer layer on which an n^--$Al_xGa_{1-x}N$ template layer was grown in order to reduce the defect density of subsequent layers. Device layers for the *p-i-n* structure were grown starting with an 80 nm-thick $Al_{0.60}Ga_{0.40}N$ Si and In codoped n^+-layer, a 16 nm-thick graded $Al_{0.60}Ga_{0.40}N$ to $Al_{0.48}Ga_{0.52}N$ ($Al_{0.45}Ga_{0.55}N$) Si and In codoped n^+-region, and a 150 nm-thick $Al_{0.48}Ga_{0.52}N$ ($Al_{0.45}Ga_{0.55}N$) unintentionally doped ($N_d \approx 10^{15}$ cm^{-3}) absorption region. This was followed by a 10 nm-thick $Al_{0.48}Ga_{0.52}N$ ($Al_{0.45}Ga_{0.55}N$) Mg doped *p*-layer, which was grown to pin the depletion region and keep it from extending into the cap layer. To insure a good *p*-contact and to avoid cracking, a 20 nm-thick graded $Al_{0.48}Ga_{0.52}N$ ($Al_{0.45}Ga_{0.55}N$) to GaN Mg doped *p*-layer was grown and terminated with a 25 nm-thick Mg doped *p*-GaN cap layer. An in situ-anneal was performed to activate the magnesium *p*-dopant. It should be noted that the $Al_xGa_{1-x}N$ *p*-layer thickness was reduced from ~ 200 nm, in previous solar-blind device designs, to 10 nm. It was found that the GaN cap layer was the *p*-layer of the *p-i-n* junction. It appears that the primary function of the $Al_xGa_{1-x}N$ *p*-layer is to pin the depletion layer and keep it from extending into the GaN layer. Devices with the GaN *p*-layer grown directly on the *i*-region showed a strong GaN response due to the depletion layer extending into the GaN layer. Standard processing, as described in Section 2.3, was used to define mesas and deposit Ti/Al/Ti/Au *n*+-contacts (annealed at 850°C for 30 sec.) and Pd/Au *p*-contacts (unannealed).

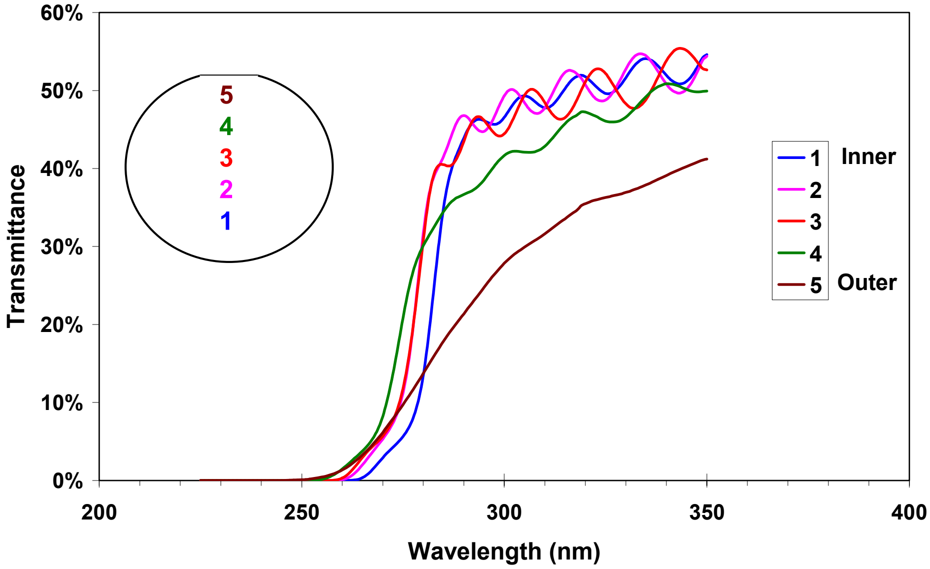

Figure 7.2: Transmission data for an In and Si codoped *n*-region solar-blind photodetector device structure.

Transmission measurements taken at various points through a device wafer showed large variations from the inner to the outer portions of the wafer. Figure 7.2 shows a set of transmission measurements for wafer M2510. Devices fabricated in sections 2 and 3 showed the best I-V and external quantum efficiency results. The sharp drop off at ~ 275 nm suggests good uniformity in the material composition. The elongated transmission slopes of sections 4 and 5 are most likely related to local variations in the In composition. This causes changes in the local band-gap which results in spreading of the absorption wavelength.

7.3 ELECTRICAL CHARACTERIZATION

The $Al_{0.48}Ga_{0.52}N$ *i*-region and $Al_{0.45}Ga_{0.55}N$ *i*-region devices showed excellent I-V characteristics. Both devices showed low dark currents, high forward currents, and a strong, flat UV photocurrent when back-illuminated with a broadband UV light source. The devices tested were both 250 μm-diameter ring devices from the C portion of the mask layout (see Appendix A).

Figure 7.3 (a) shows the dark current and UV photoresponse of an $Al_{0.48}Ga_{0.52}N$ *i*-region device of the type shown in Figure 7.1. The dark current density was 8.2×10^{-11} A/cm^2 at a reverse bias of 5 V and increased only slightly to 3.7×10^{-10} A/cm^2 at a reverse bias of 10 V. In forward bias, the current density was 2.2 A/cm^2 at 10 V. Figure 7.3 (b) shows the dark current and UV photoresponse of an $Al_{0.45}Ga_{0.55}N$ *i*-region device. The dark current density was almost the same as the $Al_{0.48}Ga_{0.52}N$ device with 8.2×10^{-11} A/cm^2 at a reverse bias of 5 V that increased only slightly to 1.5×10^{-9} A/cm^2 at 10 V. In forward bias, the current density was 17 A/cm^2 at 10 V. The increase in forward current was most likely due to a decrease in the resistivity of the *p*-GaN layer and the *p*-contact.

The junction quality of a diode is usually judged by its ideality factor, with a value ranging from 1(ideal) to 2. The low level injection regime of the dark current for both diodes was fit (dashed red line) using an exponential curve fit. The slope from this fit was then used to calculate an ideality factor of $n = 2.8$ and $n = 7.3$ for the $Al_{0.48}Ga_{0.52}N$ and $Al_{0.45}Ga_{0.55}N$ *i*-region devices, respectively. Although a lower ideality factor is usually desirable, it is important to have ohmic

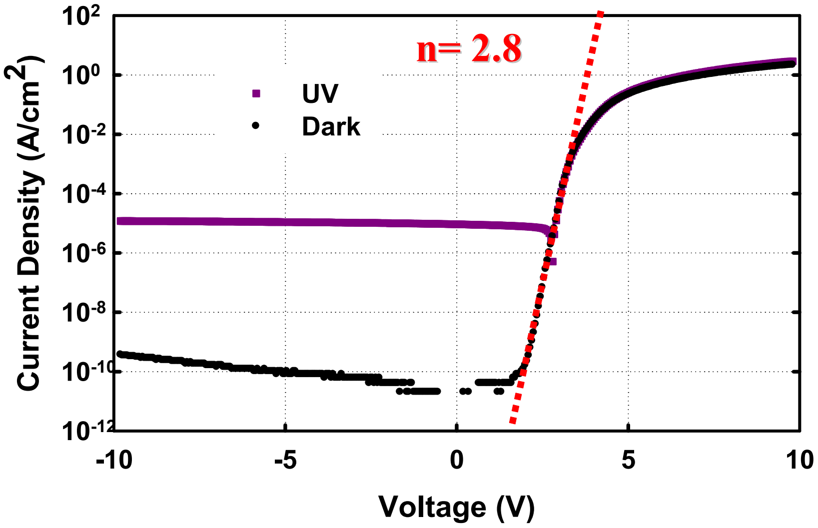

(a)

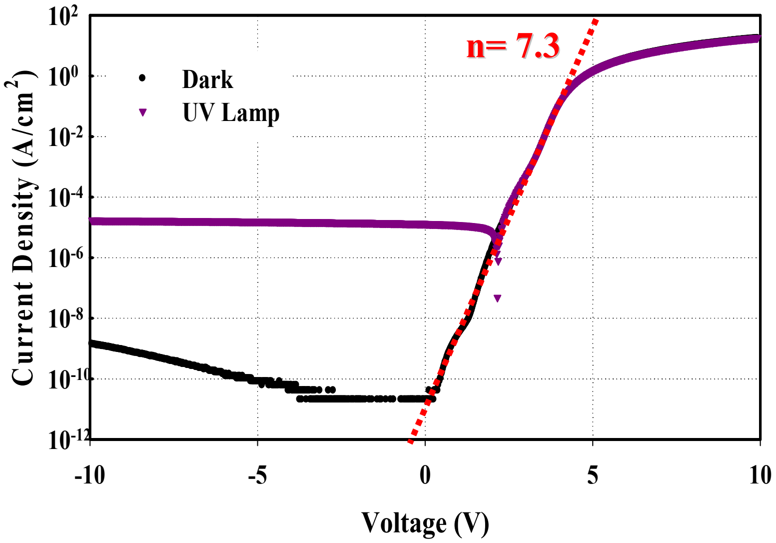

(b)

Figure 7.3: Dark current and UV photoresponse for: (a) $Al_{0.48}Ga_{0.52}N$ *i*-region, (b) $Al_{0.45}Ga_{0.55}N$ *i*-region, solar-blind photodetectors.

contacts when estimating the ideality factor by fitting the low level injection regime. The dark current of the $Al_{0.48}Ga_{0.52}N$ device does not turn on at low forward bias as the dark current of the $Al_{0.45}Ga_{0.55}N$ device does. This suggests that the $Al_{0.48}Ga_{0.52}N$ device does not have a good ohmic contact, and thus the calculated ideality factor is not a reliable number.

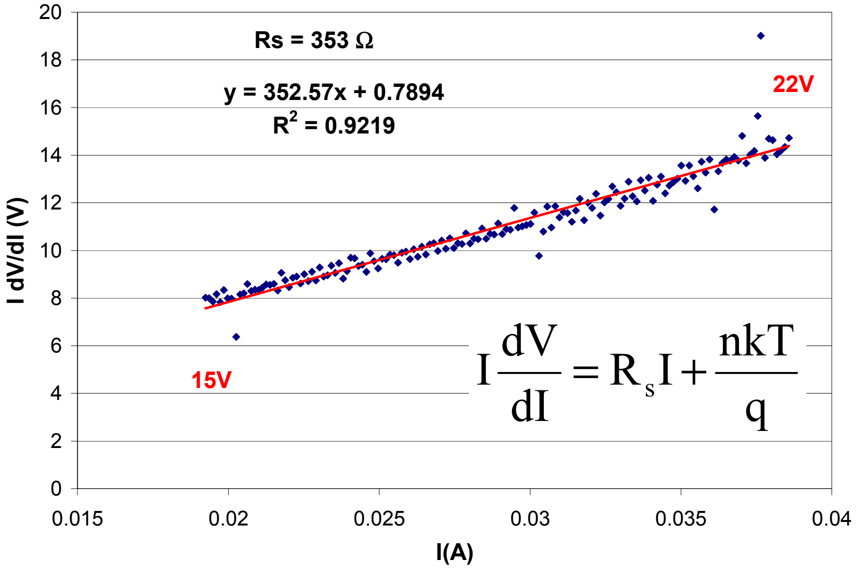

Figure 7.4: Plot of I·dV/dI vs I for the $Al_{0.45}Ga_{0.55}N$ *i*-region device. The slope of the linear curve fit gives a series resistance of ~353 Ω for a 250 μm device (0.173Ω·cm^2).

The series resistance for both devices was estimated using Equation 3.1. By rearranging the diode equation and ploting I·dV/dI vs I, the slope of the linear curve fit gives an estimate of the device's series resistance. The series resistance for the $Al_{0.48}Ga_{0.52}N$ *i*-region device was estimated to be R_S ~ 3.2 kΩ for a 250 μm-diameter device. The high forward resistance is most likely due to high GaN *p*-contact layer resistance. The series resistance for the $Al_{0.45}Ga_{0.55}N$ *i*-region device was estimated to be $R_S \sim 353\ \Omega$ for a 250 μm-diameter device as seen in Figure 7.4. The low forward resistance is attributed to good ohmic contacts and conductive *p*-type GaN, *p*-type $Al_{0.45}Ga_{0.55}N$, and *n*-type $Al_{0.6}Ga_{0.4}N$ layers.

As described in Section 2.5, the contact resistance (R_C) of a particular contact scheme, and the series resistance (R_S) of the epitaxial layer, can be calculated using a transmission line model (TLM). Figure 7.5 (a) shows the total resistance vs. contact spacing for an $Al_{0.60}Ga_{0.40}N$ Si doped *n*-type layer grown on single-polished sapphire for these measurements. The slope of the linear fit was used to calculate a series resistance of $R_S \sim 28.3\ k\Omega$, and the y-intercept ($= 2R_C$) was used to estimate the contact resistance $R_C \sim 15.5\ k\Omega$. In comparison, Figure 7.5 (b) shows the total resistance vs. contact spacing for an $Al_{0.60}Ga_{0.40}N$ In and Si codoped *n*-type layer. A series resistance of $R_S \sim 1.3\ k\Omega$, and a contact resistance $R_C \sim 640\ \Omega$, were estimated from the linear fit. The data variation from the linear fit was attributed to the non-ideal *n*-contacts, and thus the calculated series resistance and contact resistance numbers are probably over estimates. The low series resistance and low contact resistance of the $Al_{0.60}Ga_{0.40}N$ In and Si codoped *n*-type layer are attributed to a high free carrier concentration as a result of good Si activation from the codoping method. Hall measurements performed on the sample showed a high *n*-type doping of $N_d \approx 1 \times 10^{19}\ cm^{-3}$, consistent with the low series and contact resistances.

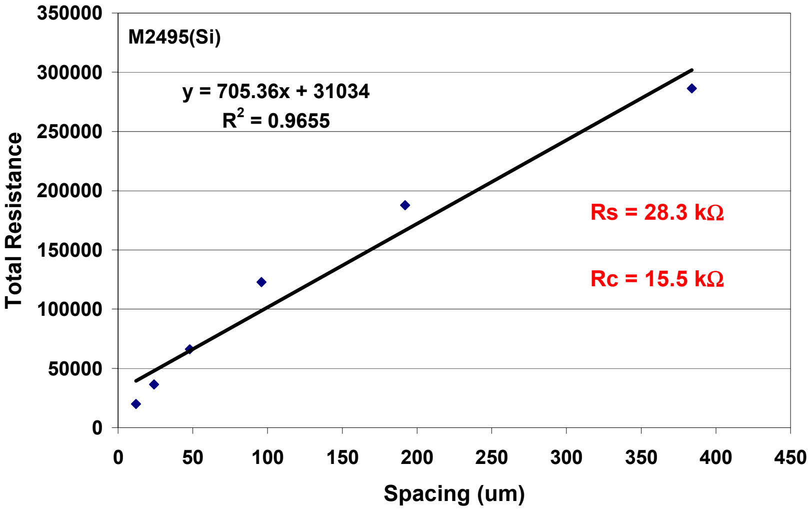

(a)

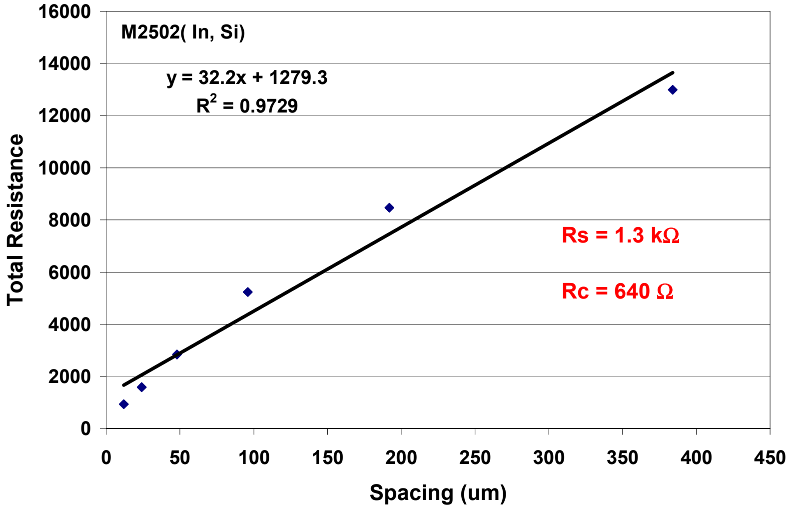

(b)

Figure 7.5: Experimental data for Ti/Al/Ti/Au to *n*- $Al_{0.60}Ga_{0.40}N$ annealed at 850°C for 30 sec: (a) Si doped, (b) In and Si codoped. Linear fit is used to extrapolate R_S, and ρ_c.

Figure 7.6 displays a two-dimensional representation of a reciprocal space map (RSM) obtained from x-ray diffraction (XRD) measurements on the $Al_{0.45}Ga_{0.55}N$ *i*-region solar-blind photodetector structure. The x-axis represents the “h” $Al_xGa_{1-x}N$ Miller index of the (hkl) notation, and the z-axis represents the “l” $Al_xGa_{1-x}N$ Miller index. The green dashed line represents the $Al_{0.60}Ga_{0.40}N$ lattice parameter. The relaxed $Al_{0.60}Ga_{0.40}N$ template layer is seen along with the fully strained $Al_{0.45}Ga_{0.55}N$ device layers. The GaN cap layer is partially relaxed seen by its shift slightly to the left.

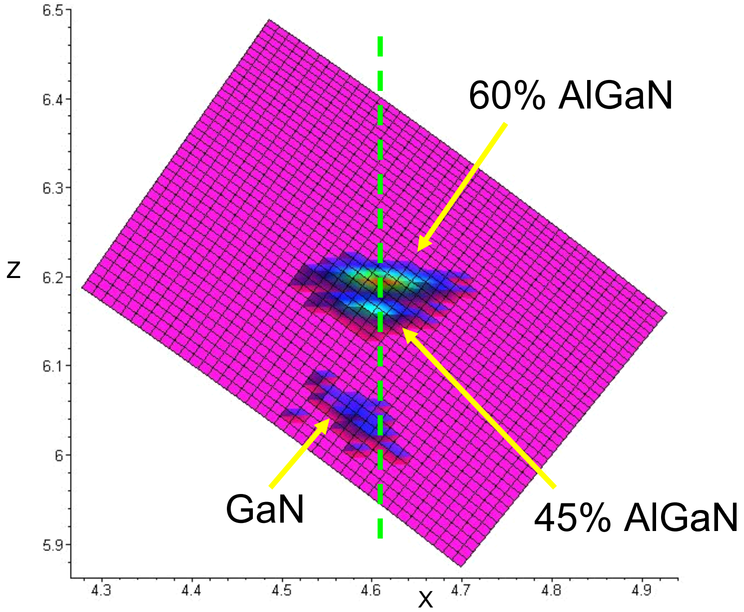

Figure 7.6: X-ray reciprocal space map of strained $Al_{0.45}Ga_{0.55}N$ device layers to $Al_{0.60}Ga_{0.40}N$ template layer. The GaN cap layer is partially relaxed.

7.4 EXTERNAL QUANTUM EFFICIENCY

Figure 7.7 shows the external quantum efficiencies and corresponding responsivity for a typical $Al_{0.48}Ga_{0.52}N$ *i*-region device. These devices were designed to have a true solar-blind response with a clear cut-off before 290 nm. The FWHM of 15 nm is determined, to a great extent, by the difference in aluminum content in the *n*- and *i*-layers. The peak zero bias external quantum efficiency was ~ 42% at 269 nm and increases to ~ 46% at a reverse bias of 5 V, corresponding to peak responsivities of 0.09 A/W and 0.11 A/W, respectively. The external quantum efficiency reached a plateau at a value of ~ 48% at a reverse bias of 10 V. Figure 7.7 (b) shows that the responsivity droped by two orders of magnitude from its peak value by 285 nm, but had a long-wavelength response out to 360 nm. This small long-wavelength response was out of phase with the peak response when measured with a lock-in amplifier, which indicated a photocurrent with opposite flow. The absolute value of the responsivity was taken in order to graph the data on a log plot. The origin of the long-wavelength response is a *p*-contact with Schottky-like behavior, which attracts photogenerated electrons in the GaN layer [93,121]. This effect decreased with an increase in reverse bias and increased with contact area. It was seen that the negative response greatly increased as the beam spot was moved from the center of a ring contact device to directly under the ring contact. The assumption of a Schottky-like *p*-contact correlates well with the delay in the forward turn on, seen in Figure 7.3 (a), and the subsequent low ideality factor.

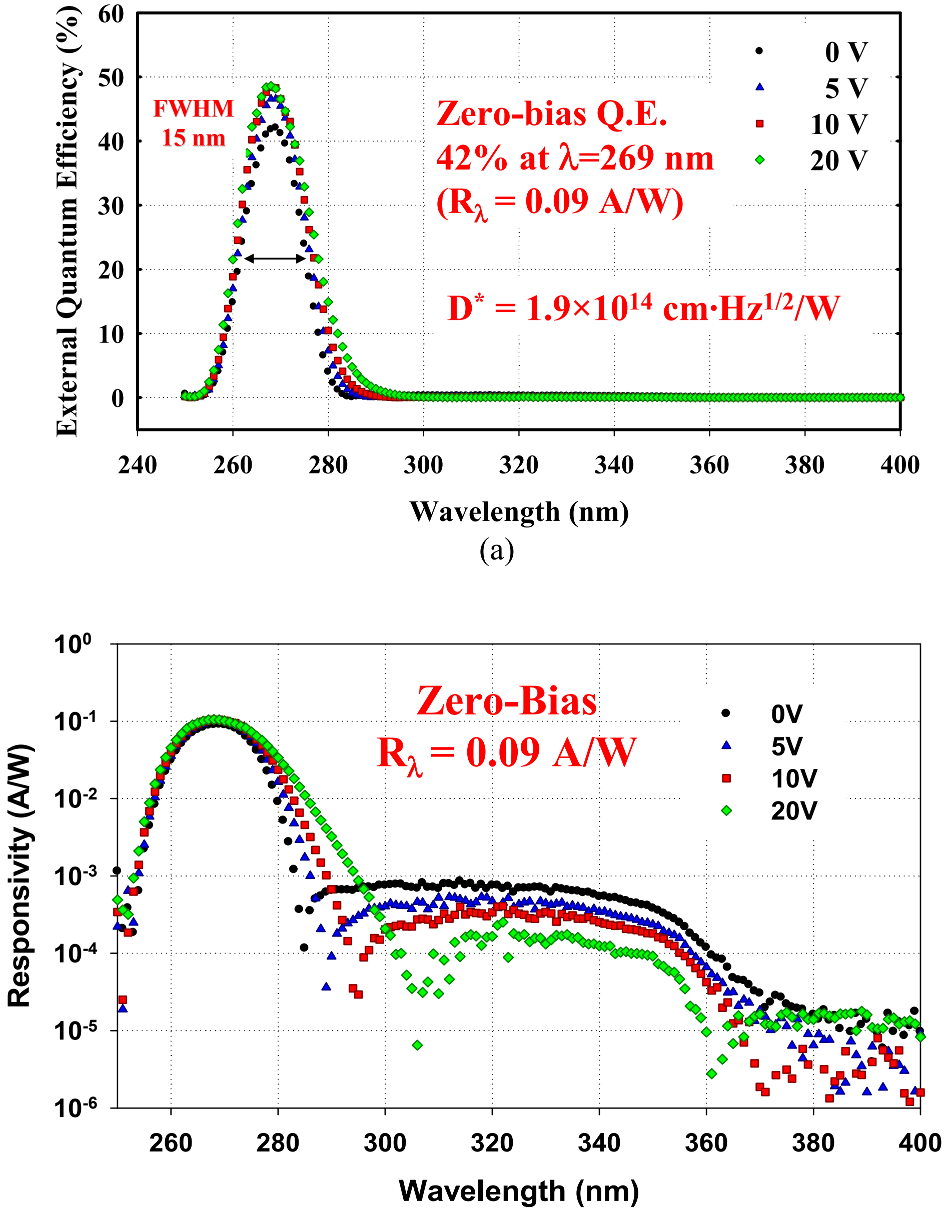

(a)

(b)

Figure 7.7: External quantum efficiency of a $Al_{0.48}Ga_{0.52}N$ *i*-region back-illuminated solar-blind photodetector, (b) Corresponding responsivity data on a semi-log scale.

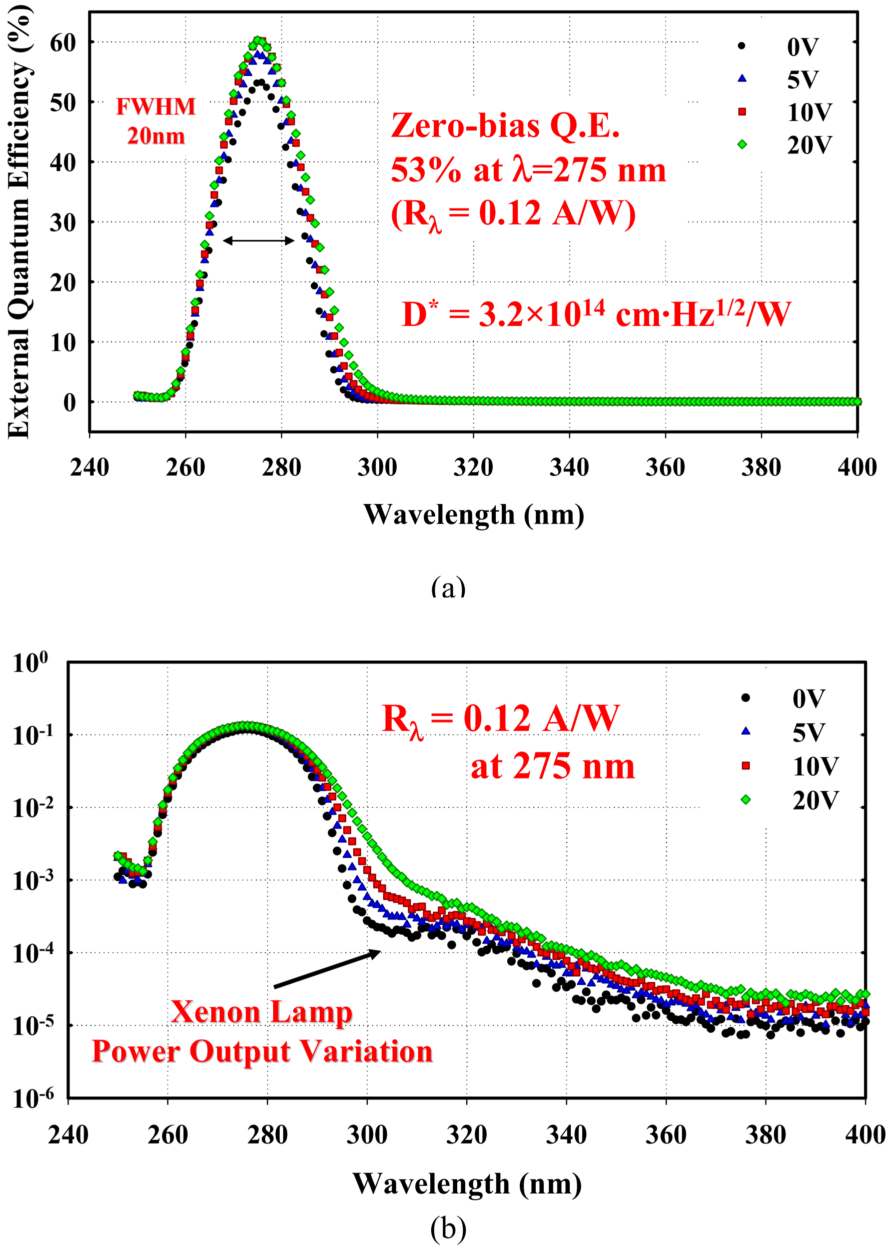

(a)

(b)

Figure 7.8: External quantum efficiency of a Al$_{0.45}$Ga$_{0.55}$N *i*-region back-illuminated solar-blind photodetector, (b) Corresponding responsivity data on a semi-log scale

Figure 7.8 shows the external quantum efficiencies and corresponding responsivity for a typical $Al_{0.48}Ga_{0.52}N$ *i*-region device. The difference in the aluminum percentage of the *n*-layer and *i*-layer was kept as large as possible while still maintaining a solar-blind response. This aluminum percentage difference insures good transmission to the *i*-layer resulting in a spectral response with 20 nm FWHM. The peak zero bias external quantum efficiency was ~ 53% at 275 nm which increased to ~ 58% at a reverse bias of 5 V, corresponding to peak responsivities of 0.12 A/W and 0.13 A/W, respectively. The external quantum efficiency reached a plateau at a value of ~ 60% at a reverse bias of 10 V. Figure 7.8 (b) shows that by 300 nm the responsivity had dropped by three orders of magnitude from its peak value. The long-wavelength response that was seen in the $Al_{0.48}Ga_{0.52}N$ *i*-region devices was greatly reduced. This was attributed to an improved *p*-GaN layer and better ohmic *p*-contacts. The plateau between 300 and 320 nm was due to the intensity of the xenon lamp source and was not a characteristic of the device. The noise floor for responsivity measurements depends on the intensity of the light source. As seen in Figure 7.8 (b), the noise floor of the measurement dropped as the lamp intensity increased above 320 nm.

7.5 HIGH DETECTIVITY

In previous chapters solar-blind devices have been described with zero bias external quantum efficiencies of 12% at $\lambda = 278$ nm (Chapter 5) and 26% at $\lambda = 279$ nm (Chapter 6). The improvement in external quantum efficiency of Chapter 6, however, did not correspond to an improvement in the detectivity. To understand this we must examine the procedure for calculating detectivity. To date it has not been possible to directly measure the noise of a solar-blind photodetector near zero bias [48,50,51] because the noise is below the detection limits of commercially available test apparatus. As a result, the noise has been estimated from the differential resistance that has been obtained from fits to the *I-V* curves (Section 4.5). The differential resistance R_0, is related to the dark current and increases as the dark current decreases. Since these devices operate in the solar-blind region where the background radiation is very low, it is assumed that thermal noise is dominant. For this case the specific detectivity is given by Equation 4.5.

Figure 7.9 (a) shows a semi-log plot of the I-V characteristics of an $Al_{0.45}Ga_{0.55}N$ *i*-region solar-blind photodetector with exponential curve fits. The parameters of the curve fits were used to estimate the current of the actual device with the equation at the top of Figure 7.9 (a). Figure 7.9 (b) shows a linear plot of the I-V data compared to the estimated current equation. The estimated equation fits the data well, and was used to calculate the differential resistance at zero bias, $R_0 = 2.51 \times 10^{14}\ \Omega$. This corresponds to an R_0A value of $1.23 \times 10^{11}\ \Omega \cdot cm^2$ for a 250 μm-diameter device. Using this R_0A value in Equation 4.5, with the zero bias responsivity, $R_\lambda = 0.12$ A/W, a detectivity of $D^* = 3.2 \times 10^{14}$ cm·Hz$^{1/2}$·W^{-1} was calculated. Repeating this technique for the $Al_{0.48}Ga_{0.52}N$ *i*-region device, a differential resistance of $R_0 = 1.47\times10^{14}$ W was calculated corresponding to a R_0A value of $7.24 \times 10^{10}\ \Omega \cdot cm^2$. With the zero bias responsivity, $R_\lambda = 0.09$ A/W, a

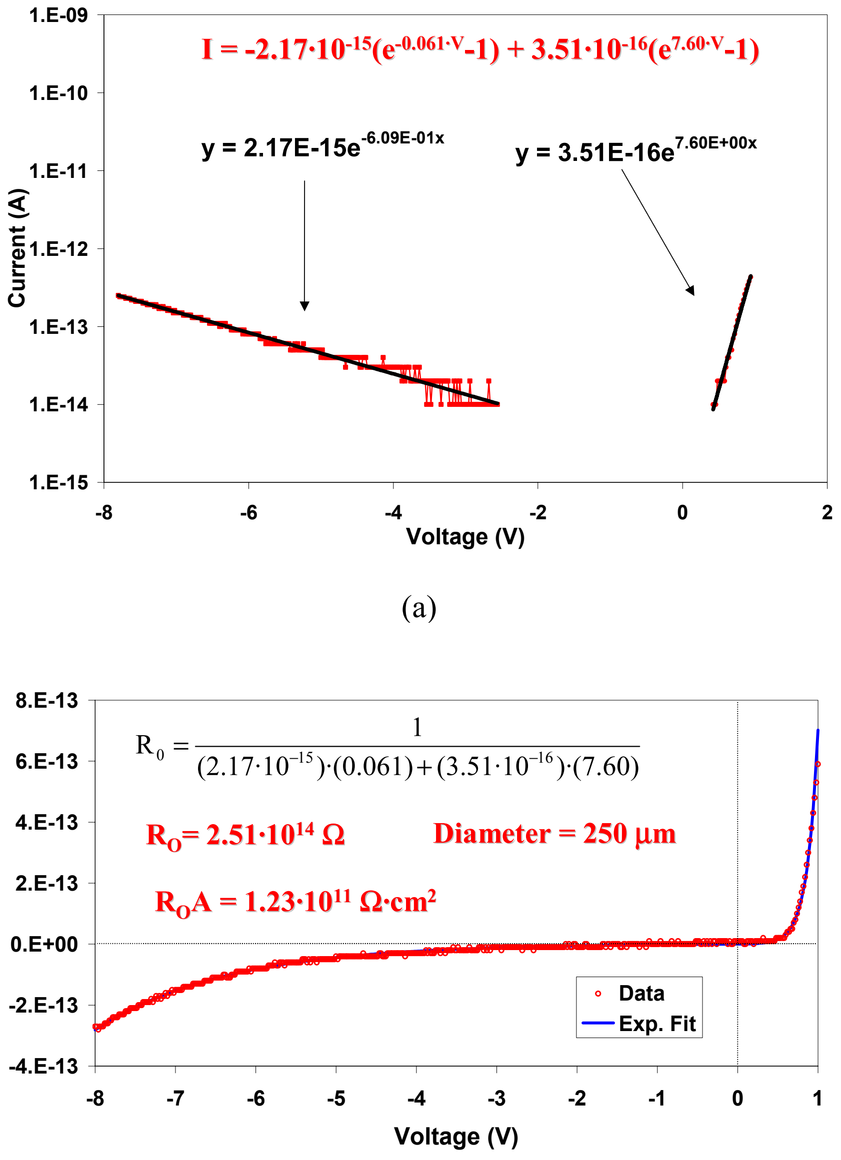

(a)

(b)

Figure 7.9: (a)Semi-log plot of I-V characteristics of a $Al_{0.45}Ga_{0.55}N$ *i*-region solar blind photodetector with exponential curve fits, (b) Linear plot of the same data compared to curve fit. Dirivative of fit at zero bias give $R_0 = 2.51 \times 10^{14}\ \Omega$.

detectivity of $D^* = 1.9 \times 10^{14}$ cm·Hz$^{1/2}$·W^{-1} was calculated. This value was slightly lower than the $Al_{0.45}Ga_{0.55}N$ *i*-region device, due to the lower responsivity.

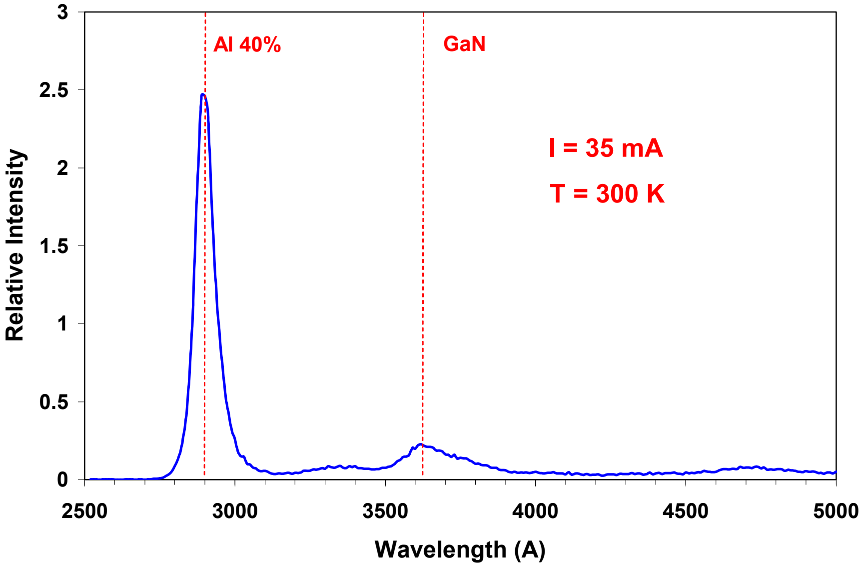

Figure 7.11: Electroluminescence spectrum at 300 K for the $Al_{0.45}Ga_{0.55}N$ *i*-region solar-blind photodetector.

7.6 ULTRAVIOLET LIGHT EMITTING DIODE

As seen in Section 6.7, ultraviolet photodetectors occasionally emit measurable amounts of UV radiation when forward biased. The $Al_{0.45}Ga_{0.55}N$ *i*-region detector was forward biased as a light emitting diode. Figure 7.11 shows the electroluminescence spectrum for a typical LED at I = 30 mA DC (56.1 A/cm^2). The electroluminescence of these photodiodes had a narrow FWHM of 7.0 nm peaked at λ = 289 nm, which should correspond to an $Al_{0.4}Ga_{0.60}N$ *i*-region. As described above, the solar-blind detector had an $Al_{0.45}Ga_{0.55}N$ *i*-region, suggesting a red shift in the LED output. This red shift can be due to heating in the LED at the high current level, from large contact and *p*-layer resistances, or to emission through defects in the band gap. The ultraviolet output power at 30 mA DC was measured to be ~ 72 nW using a calibrated UV-enhanced Si photodiode placed against the back-side of the double-polished sapphire substrate to collect as much light as possible.

7.8 SUMMARY

By increasing the composition of aluminum in the “window” *n*-layer, an improved structure has been used to achieve high external quantum efficiencies at low bias. We report a zero bias external quantum efficiency of ~ 42% at 269 nm which rises to ~ 46% with a reverse bias of 5 V for the $Al_{0.48}Ga_{0.52}N$ *i*-region device. By slightly decreasing the aluminum percentage in the *i*-region to $Al_{0.45}Ga_{0.55}N$, the zero bias external quantum efficiency was increased to ~ 53% at 275 nm with ~ 58% at a reverse bias of 5 V. The low leakage currents of these devices lead to large differential resistances, which when combined with the high external quantum efficiency at zero bias, gave solar-blind detectivities of $D^* = 1.9\times10^{14}$ cm-Hz$^{1/2}$-W^{-1} at $\lambda = 269$ nm and $D^* = 3.2\times10^{14}$ cm-Hz$^{1/2}$-W^{-1} at $\lambda = 275$ nm for the $Al_{0.48}Ga_{0.52}N$ and $Al_{0.45}Ga_{0.55}N$ *i*-region devices, respectively. These devices approach the sensitivity of photomultiplier tubes.

8. Summary of Research

8.1 GOALS, PROBLEMS, AND SOLUTIONS

The goal of this research project was to design, fabricate, and characterize back-illuminated solar-blind photodetectors suitable for flip-chip mounting to silicon readout circuits (Section 5.1). These photodetectors were to have high zero bias external quantum efficiencies and corresponding large detectivities for use in detecting very low signal levels.

This research started with Dr. Carrano and Dr. Li's top-illuminated $Al_xGa_{1-x}N$/GaN heterojunction recessed window devices described in Section 3.2. By using an $Al_xGa_{1-x}N$ "window" *p*-layer, light near the band gap of GaN could pass to the *i*-region with minimal attenuation. Due to difficulties in making ohmic contact to *p*-$Al_xGa_{1-x}N$, a thin GaN cap layer was used. To avoid absorption in this GaN cap layer a recessed window was used in the center of the ring contact. The recessed window created a field-crowding problem under the ring *p*-contacts due to the large lateral resistance of the *p*-$Al_xGa_{1-x}N$ layer. One of my first projects was to design a semi-transparent *p*-contact to cover the recessed window and spread out the field profile. This resulted in devices with ~ 77% at $\lambda = 357$ nm external quantum efficiency at zero bias (Section 3.5). This value was used as a goal for the back-illuminated solar-blind devices.

To shift the peak external quantum efficiency from 357 nm toward the solar-blind goal of 280nm, it was necessary to increase the aluminum percentage of the absorption region. As $Al_xGa_{1-x}N$ layers with increased aluminum percentage were grown on the available GaN template layers, cracking problems were seen due to their lattice mismatch. To try and minimize this strain induced cracking, selective-area regrowth was used to define the device mesas, resulting in 74 μm-diameter crack free devices (Section 4.1). These top-illuminated photodiodes had peak external quantum efficiencies of ~ 20% at λ = 314 nm. This peak was shifted ~ 45 nm toward the solar-blind from the above mentioned GaN peak.

By working closely with Dr. Lambert of Professor Dupuis' group, the group's first back-illuminated solar-blind detectors were fabricated with a "window" $Al_{0.60}Ga_{0.40}N$ template layer and $Al_{0.40}Ga_{0.60}N$ device layers (Section 5.2). The majority of the incident light that passed through the template layer was absorbed in the *n*-region, which limited the zero bias external quantum efficiency to ~ 12% at λ = 280 nm. These diodes had low dark currents, which lead to a detectivity of $D^* = 5.3 \times 10^{13}$ $cm \cdot Hz^{1/2} \cdot W^{-1}$ (Section 5.4).

To improve the zero bias external quantum efficiency, the aluminum percentage of the *n*-layer was increased to create a "window" to the *i*-region. These photodiodes had an $Al_{0.60}Ga_{0.40}N$ template layer, an $Al_{0.50}Ga_{0.50}N$ "window" *n*-region and an $Al_{0.41}Ga_{0.59}N$ absorption region (Section 6.1). The zero bias external quantum efficiency was increased to ~ 26% at λ = 279 nm. The detectivity, however, decreased with a value of $D^* = 5.0 \times 10^{12}$ $cm \cdot Hz^{1/2} \cdot W^{-1}$. This decrease was due to large dark currents near zero bias (Section 6.6). Modeling of the external quantum efficiency was used to determine that the limiting factor was the difference of the aluminum percentage between the "window" *n*-region and the absorbing *i*-region.

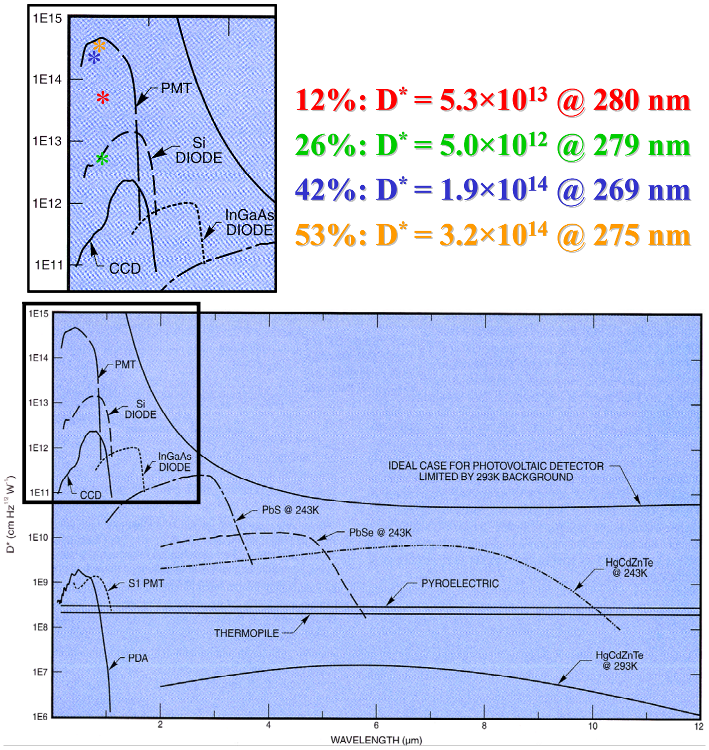

Figure 8.1: D* values for common photodetectors. The inset shows the four solar-blind detectors discussed in this dissertation.

To further increase the external quantum efficiency, the aluminum percentage of the *n*-region needed to be increased even further. U. Chowdury and M. Wong from Professor Dupuis' group achieved this by codoping the *n*-region with In and Si (Section 7.1). By using this codoping method, solar-blind photodetectors were achieved with $Al_{0.60}Ga_{0.40}N$ template and "window" *n*-regions. The first photodetector with this codoped *n*-region had an $Al_{0.48}Ga_{0.52}N$

i-region designed to push it further into the solar-blind region. This device had a zero bias external quantum efficiency of ~ 42% at λ = 269 nm, and low dark current resulting in a detectivity of $D^* = 1.9 \times 10^{14}$ cm·Hz$^{1/2}$·W^{-1}. By slightly decreasing the aluminum percentage of the *i*-region to $Al_{0.45}Ga_{0.55}N$, the zero bias external quantum efficiency was increased to ~ 53% at λ = 275 nm, with a detectivity of $D^* = 3.2 \times 10^{14}$ cm·Hz$^{1/2}$·W^{-1}. This is the highest detectivity reported for a back-illuminated $Al_xGa_{1-x}N$ solar-blind photodetector.

Figure 8.1 shows a graph of the detectivities of many of the most common photodetectors. The inset shows an enlarged view of the solar-blind region, with the colored markers indicating the four solar-blind detectors described in this dissertation. The $Al_{0.45}Ga_{0.55}N$ *i*-region device has the largest detectivity; it is comparable to the detectivity of a photomultiplier tube (PMT). This indicates that we have achieved our goals of both high zero bias external quantum efficiency and large detectivity back-illuminated solar-blind photodetectors.

Appendix A

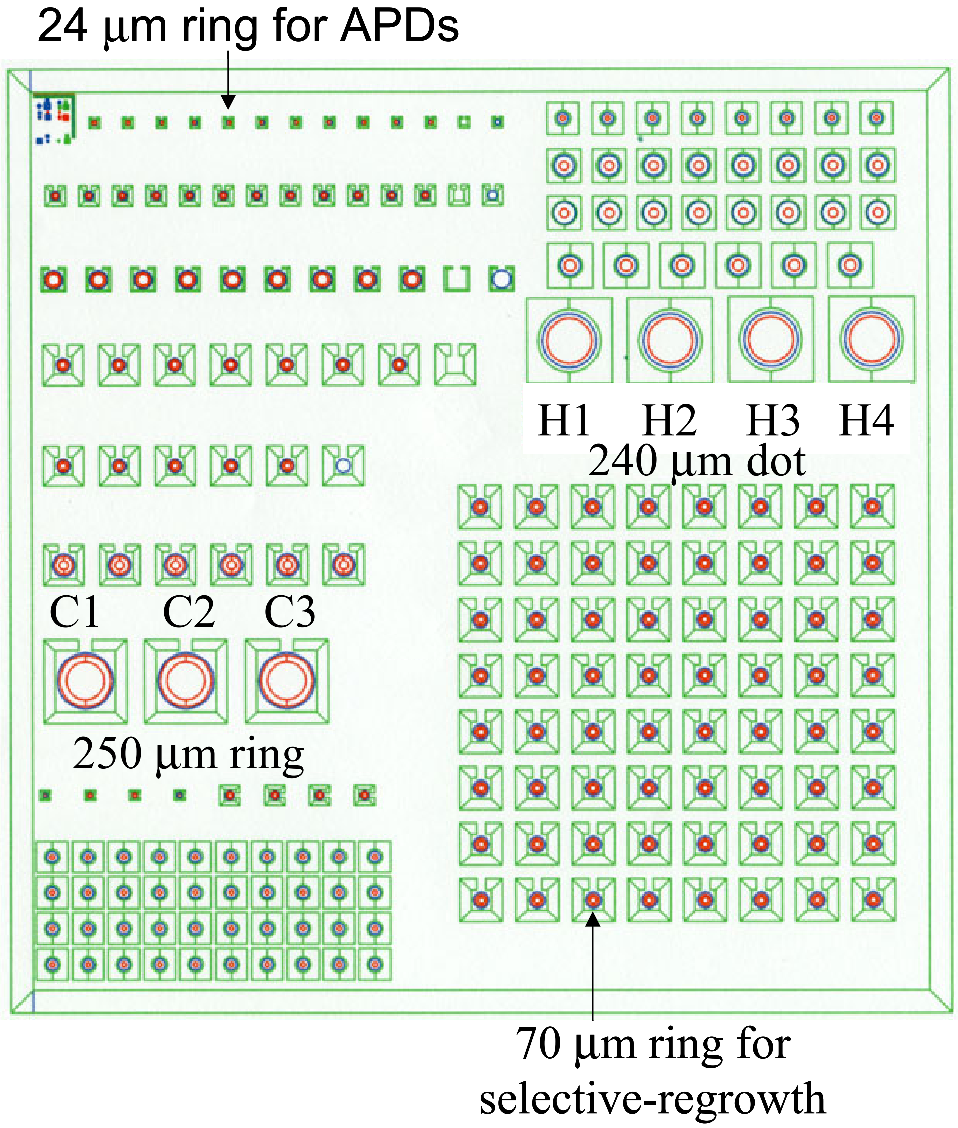
24 µm ring for APDs
H1
H2
H3
H4
240 µm dot
C1
C2
C3
250 µm ring
70 µm ring for selective-regrowth

Appendix B

PUBLICATIONS

1. C. J. Collins, U. Chowdhury, M .M. Wong, B. Yang, A. L. Beck, R. D. Dupuis, and J. C. Campbell, "High Zero-Bias External Quantum Efficiency Solar-Blind Heterojunction *p-i-n* Photodiode", *submitted to Elec. Lett.* April 2002.

2. C. J. Collins, U. Chowdhury, M .M. Wong, B. Yang, A. L. Beck, R. D. Dupuis, and J. C. Campbell, "Improved Solar Blind Detectivity using an $Al_xGa_{1-x}N$ Heterojunction *p-i-n* Photodiode", *Appl. Phys. Lett.*, vol. 80, pp. 3754, 2002.

3. C. J. Collins, T. Li, D. J. H. Lambert, M. M. Wong, R. D. Dupuis, and J. C. Campbell, "Selective Regrowth of $Al_{0.30}Ga_{0.70}N$ *p-i-n* Photodiodes", *Appl. Phys. Lett.*, vol. 77, pp. 2810, 2000.

4. C. J. Collins, T. Li, A. L. Beck, J. C. Carrano, M. J. Schurman, I. A. Ferguson, R. D. Dupuis, and J. C. Campbell, "Improved device performance using a semi-transparent *p*-contact AlGaN/GaN heterojunction *p-i-n* photodiode", *Appl. Phys. Lett.*, vol. 75, pp. 2139, 1999.

5. U. Chowdhury, M. M. Wong, C. J. Collins, B. Yang, J. C. Denyszyn, J. C. Campbell, and R. D. Dupuis, "High-Performance Solar-Blind Photodetector Using an $Al_{0.60}Ga_{0.40}N$ *n*-type Window Layer" *submitted to J. Cryst. Grow.*, 2002.

6. M. M. Wong, J. C. Denyszyn, C. J. Collins, U. Chowdury, T. G. Zhu, K. S. Kim, and R. D. Dupuis, "AlGaN/AlGaN Double-heterojunction Ultraviolet Light-emitting Diodes Grown by Metal Organic Chemical Vapor Deposition", *Electron. Lett.*, vol. 37, pp. 1188, 2001.

7. J. C. Campbell, C. J. Collins, M. M. Wong, U. Chowdhury, A. L. Beck, and R. D. Dupuis, "High Quantum Efficiency at Low Bias $Al_xGa_{1-x}N$ *p-i-n* Photodiodes", *phys. stat. sol. (a)*, vol. 188, pp. 283, 2001.

8. T. Li, D. J. H. Lambert, M. M. Wong, C. J. Collins, B. Yang, A. L. Beck, U. Chowdhury, R. D. Dupuis, and J. C. Campbell, "Low-Noise Back-Illuminated $Al_xGa_{1-x}N$-Based Solar-Blind Ultraviolet Photodetectors", *IEEE J. Quantum Electron,* vol. 37, pp. 538, 2001.

9. D. J. H. Lambert, M. M. Wong, U. Chowdhury, C. Collins, T. Li, H. K. Kwon, B. S. Shelton, T. G. Zhu, J. C. Campbell, and R. D. Dupuis, “Back Illuminated AlGaN Solar-Blind Photodetectors”, *Appl. Phys. Lett.*, vol. 77, pp. 1900, 2000.

10. B. Yang, D.J.H. Lambert, T. Li, C.J. Collins, M.M. Wong, U. Chowdhury, R.D. Dupuis and J.C. Campbell, “High-performance back-illuminated solar-blind AlGaN metal-semiconductor-metal photodetectors”, *Electron. Lett.*, vol. 36, No. 22, 2000.

11. B. Yang, T. Li, K. Heng, C. Collins, S. Wang, J. C. Carrano, R. D. Dupuis, J. C. Campbell, M. J. Schurman, and I. T. Ferguson, “Low Dark Current GaN Avalanche Photodiodes”, *IEEE J. Quantum Electron*., vol. 36, pp. 1389, 2000.

12. B. Yang, K. Heng, T. Li, C. J. Collins, S. Wang, R. D. Dupuis, J. C. Campbell, M. J. Schurman, and I.T. Ferguson, “32×32 Ultraviolet $Al_{0.1}Ga_{0.9}N$/GaN *p-i-n* Photodetector Array”, *IEEE J. Quantum Electron.*, vol. 36, pp. 1229, 2000.

13. S. Wang, T. Li, J. M. Reifsnider, B. Yang, C. Collins, A. L. Holmes, Jr., and J. C. Campbell, “Schottky Metal-Semiconductor-Metal Photodetectors on GaN Films Grown on Sapphire by Molecular Beam Epitaxy”, IEEE J. Quantum Electron, vol. 36, pp. 1262, 2000.

14. T. Li, S. Wang, A. L. Beck, C. J. Collins, B. Yang, R. D. Dupuis, J. C. Carrano, M. J. Schurman, I. T. Ferguson, and J. C. Campbell, “High quantum efficiency $Al_xGa_{1-x}N$/GaN-based ultraviolet *p-i-n* photodetectors with a recessed window structure”, *Proc. SPIE*, vol. 3948, pp. 304, 2000.

15. J. C. Carrano, D. J. H. Lambert, C. J. Eiting, C. J. Collins, T. Li, S. Wang, B. Yang, A. L. Beck, R. D. Dupuis, and J. C. Campbell, “GaN avalanche photodiodes”, *Appl. Phys. Lett.*, 76, pp. 924, 1999.

16. J. C. Carrano, T. Li, P. A. Grudowski, C. J. Eiting, D. H. Lambert, C. J. Collins, A. L. Beck, S. Wang, B. Yang, M. Schurman, I. Ferguson, R. D. Dupuis, and J. C. Campbell, “Improved detection of the invisible”, *IEEE Circuit & Devices*, vol. 15, pp. 15, 1999.

17. T. Li, A. L. Beck, C. Collins, J. C. Carrano, M. J. Schurman, I. A. Ferguson, R. D. Dupuis, and J. C. Campbell, “Improved ultraviolet quantum efficiency using a semitransparent recessed window AlGaN/GaN heterojunction *p-i-n* photodiode”, *Appl. Phys. Lett.*, vol. 75, 2421, 1999.

CONFERENCES

1. C. J. Collins, U. Chowdhury, M .M. Wong, B. Yang, A. L. Beck, R. D. Dupuis, and J. C. Campbell, "High Detectivity Solar-Blind AlGaN Photodetectors" 7th Wide Bandgap III-Nitride Workshop, (March 2002).

2. C. J. Collins, T. Li, D. J. Lambert, M. M. Wong, B. Yang, A. L. Beck, R. D. Dupuis, and J. C. Campbell, " Back-Illuminated Solar-Blind Photodetectors", LEOS, (2000).

3. C. J. Collins, T. Li, A. L. Beck, J. C. Carrano, M. J. Schurman, I. A. Ferguson, R. D. Dupuis, and J. C. Campbell, "Improved device performance using a semi-transparent p-contact AlGaN/GaN heterojunction p-i-n photodiode", LEOS, (1999).

4. U. Chowdhury, M. M. Wong, C. J. Collins, B. Yang, J. C. Denyszyn, J. C. Campbell, R. D. Dupuis, "High-Performance AlGaN/GaN Solar-Blind Detectors Grown by MOCVD" WOCSEMMAD, (February 2002).

5. J. C. Campbell, C. J. Collins, M. M. Wong, U. Chowdhury, A. L. Beck, and R. D. Dupuis, "High Quantum Efficiency at Low Bias $Al_xGa_{1-x}N$ *p-i-n* Photodiodes", LEOS,(2001).

6. U. Chowdhury, M. M. Wong; C. J. Collins; B. Yang; T. G. Zhu; A. L. Beck; J. C. Campbell; and R. D. Dupuis, "High Quantum Efficiency AlGaN/GaN Solar-Blind Photodetectors Grown by Metalorganic Chemical Vapor Deposition," Proceedings of Symposium I, 2001 Fall MRS Meeting, (2001).

7. M. M. Wong, U. Chowdhury, C. Collins, B. Yang, J. C. Denyszyn, K. S. Kim, J. C. Campbell, and R. D. Dupuis, "High Quantum Efficiency of AlGaN/GaN Solar-Blind Photodetectors Grown by Metalorganic Chemical Vapor Deposition," Fourth International Conference on Nitride Semiconductors, (July 2001).

8. M. Wraback. H. Shen, J. C. Carrano, C. J. Collins, J. C. Campbell, C. J. Eiting, D. J. H. Lambert, U. Chowdhury, M. M. Wong, R. D. Dupuis, M. J. Schurman, and I. Ferguson, "Measurement of Carrier Transport in GaN Using GaN Homojunction and AlGaN/GaN Heterojunction *p-i-n* Diodes," 43rd EMC, Notre Dame, Indiana (June 2001).

9. D. J. H. Lambert, B. Yang, T. Li, C. J. Collins, M. M. Wong, U. Chowdhury, J. C. Campbell, and R. D. Dupuis, “High-performance Back-illuminated Solar-blind AlGaN Photodetectors Grown by Metalorganic Chemical Vapor Deposition,” 199th Electrochemical Society Meeting, Washington DC (March 2001).

10. U. Chowdhury, D. J. H. Lambert, B. Yang, C. J. Collins, T. Li, M. M. Wong. B. S. Shelton, J. C. Campbell, and R. D. Dupuis, “Structural Optimization of AlGaN Back-Illuminated Solar-Blind MSMs Grown by Metalorganic Chemical Vapor Deposition,”, WOCSEMMAD, (February 2001).

11. R. D. Dupuis, J. C. Campbell, D. J. H. Lambert, B. Yang, T. Li, C. J. Collins, M. M. Wong, and U. Chowdhury, “High-performance Back-illuminated Solar-blind AlGaN Metal-Semiconductor-metal Photodetectors”, DARPA/MTO Optoelectronics Review, (October 2000).

12. D. J. H. Lambert, B. Yang, T. Li, C. J. Collins, M. M. Wong, U. Chowdhury, B. Shelton, A. L. Beck, J. C. Campbell, and R. D. Dupuis, “Back-illuminated Solar-blind AlGaN Metal-Semiconductor-Metal Photodetectors”, 27th International Symposium on Compound Semiconductors,” (October 2000).

13. D. J. H. Lambert, M. M. Wong, U. Chowdhury, C. Collins, B. Yang, T. Li, H. K. Kwon, B. S. Shelton, T. G. Zhu, J. C. Campbell, and R. D. Dupuis, “High Performance AlGaN and GaN Photodetectors Grown by Metalorganic Chemical Vapor Deposition,” 42nd EMC, (June 2000).

14. D. J. H. Lambert, C. J. Eiting, M. M. Wong, U. Chowdhury, T. Li, B. Yang, C. J. Collins, J. C. Campbell, and R. D. Dupuis, “Performance of $Al_xGa_{1-x}N$/GaN *p-i-n* Photodiodes Grown by MOCVD,” 6th Wide Bandgap III-Nitride Workshop (March 2000).

15. D. J. H. Lambert, M. M. Wong, U. Chowdhury, C. Collins, J. C. Carrano, B. Yang, T. Li, J. C. Campbell, and R. D. Dupuis, “AlGaN/GaN Solar-Blind Detectors Grown by MOCVD,” WOCSEMMAD, (February 2000).

16. J. C. Carrano, T. Li, A. L. Beck, C. Collins, R. D. Dupuis, J. C. Campbell, M. J. Schurman, and I. A. Ferguson, “Improved Ultraviolet Quantum Efficiency Using a Transparent Recessed Window AlGaN/GaN Heterojunction *p-i-n* Photodiode”, IEDM, (1999).

Bibliography

[1] Ting Li, Dissertation, Aug. 2000.

[2] Damien Lambert, Dissertation, Dec. 2000.

[3] J. P. Basrur, F. S. Choa, P. L. Liu, J. Sipor, G. Rao, G. M. Carter, and Y. J. Chen, *Appl. Phys. Lett.*, vol. 71, pp. 1385, 1997.

[4] M. Osinski, J. Zeller, P. C. Chiu, B. S. Phollops, and D. L. Barton, *Appl. Phys. Lett.*, vol. 69, pp. 898, 1996.

[5] S. Nakamura, T. Mukai, and M. Senoh, *Jpn. J. Appl. Phys. Part 2*, vol. 30, pp. L1998, 1991.

[6] S. Nakamura, M. Senoh, and T. Mukai, *Appl. Phys. Lett.*, vol. 62, pp. 2390, 1993.

[7] S. Nakamura, M. Senoh, S. Nagahama, N. Iwasa, T. Yamada, T. Matsushita, H. Kiyoku, and Y. Sugimoto, *Jpn. J. Appl. Phys. Part 2*, vol. 35, pp. L74, 1996.

[8] T. Kashima, R. Nakamura, M. Iwaya, H. Katoh, S. Yamaguchi, H. Amano, and I. Akasaki, *Jpn. J. Appl. Phys. Part 2*, vol. 38, pp. L1515, 1999.

[9] R. D. Dupuis, and J. C. Campbell, Book Chapter, to be submitted.

[10] E. C. Weatherhead, G. C. Tiao, G. C. Reinsel, J. E. Frederick, J. J. DeLuisi, D. Choi, and W. K. Tam, *J. Geophys. Res.*, vol. 102, pp. 8737, 1997.

[11] D. Walker, V. Kumar, K. Mi, P. Kung, X. H. Zhang, and M. Razeghi, *Appl. Phys. Lett.*, vol. 76, pp. 403, 2000.

[12] T. Detchprohm, K. Hiramatsu, K. Itoh, and I, Akasaki, *Jpn. J. Appl. Phys.*, vol. 31, pp. L1454, 1992.

[13] M. Tanaka, S. Nakahata, K. Sogabe, H. Nakata, and M. Tabioka, *Jpn. J. Appl. Phys.*, vol. 36, pp. L1062, 1997.

[14] B. J. Skromme, *Appl. Phys. Lett.*, vol. 71, pp. 829, 1997.

[15] P. B. Perry and R. F. Rutz, *Appl. Phys. Lett.*, vol. 33, pp. 319, 1978.

[16] M. C. Benjamin, M. D. Bremser, T. W. Weeks Jr., S. W. King, R. F. Davis, and R. J. Nemanich, *Appl. Surf. Sci.*, vol. 104, pp. 455, 1996.

[17] D. Brunner, H. Angerer, E. Bustarret, F. Freudenberg, R. Hopler, R. Dimitrov, O. Ambacher, and M. Stutzmann, *J. Appl. Phys.*, vol. 82, pp. 5090, 1997.

[18] G. A. Cox, D. O. Cummins, K. Kawabe, and R. H. Tredgold, *J. Phys. Chem. Solids*, vol. 28, pp. 543, 1967.

[19] M. A. Khan, J. N. Kuznia, D. T. Olson, J. M. Van Hove, M. Blasingame, and L. F. Reitz, *Appl. Phys. Lett.*, vol. 60, pp. 2917, 1992.

[20] K. S. Stevens, M. Kinniburgh, and R. Beresford, *Appl. Phys. Lett.*, vol. 66, pp. 3518, 1995.

[21] M. Misra, T. D. Moustakas, R. P. Vaudo, R. Singh, and K. S. Shah, *Proc. SPIE*, vol. 2519, pp. 78, 1995.

[22] B. W. Lim, Q. C. Chen, J. Y. Yang, and M. Asif Khan, *Appl. Phys. Lett.*, vol. 68, pp. 3761, 1996.

[23] L. B. Flannery, I. Harrison, D. E. Lacklison, R. I. Dykeman, and T. S. Cheng, *Mater. Sci. Engr. B*, vol. 50, pp. 307, 1997.

[24] D. Walker, X. Zhang, P. Kung, A. Saxler, S. Javadpour, J. Xu, and M. Razeghi, *Appl. Phys. Lett.*, vol. 68, pp. 2100, 1996.

[25] Q. Chen, J. W. Yang, A. Osinsky, S. Gangopadhyay, B. Lim, M. Z. Anwar, M. Asif Kahn, D. Kuksenkov, and H. Temkin, *Appl. Phys. Lett.*, vol. 70, pp. 2277, 1997.

[26] A. Osinsky, S. Gangopadhyay, B. Lim, M. Z. Anwar, M. Asif Kahn, D. Kuksenkov, and H. Temkin, *Appl. Phys. Lett.*, vol. 72, pp. 742, 1998.

[27] S. Liang, W. Cai, Y. Liu, C. A. Tran, R. F. Karlicek, and I. Ferguson, *III-V Nitrides Symposium*, pp. 1221, 1997.

[28] E. Monroy, F. Calle, E. Munoz, and F. Omnes, *Appl. Phys. Lett.*, vol. 74, pp. 3401, 1999.

[29] G. Smith, M. J. Estes, J. Van Nostrand, T. Dang, P. J. Screiber, H. Temkin, and J. Hoelscher, *Proc. SPIE*, vol. 3629, pp. 184, 1999.

[30] A. Osinsky, S. Gangopadhyay, J. W. Yang, R. Gaska, D. Kuksenkov, H. Temkin, I. K. Shmagin, Y. C. Chang, J. F. Muth, and R. M. Kolbas, *Appl. Phys. Lett.*, vol. 72, pp. 551, 1998.

[31] E. Monroy, F. Calle, E. Munoz, F. Omnes, P. Gilbart, and J. A. Munoz, *Appl. Phys. Lett.*, vol. 73, pp. 2146, 1998.

[32] F. Binet, J. Y. Duboz, N. Laurent, E. Rosencher, O. Briot, and R. L. Aulombard, *J. Appl. Phys.*, vol. 81, pp. 6449, 1997.

[33] S. Wang, T. Li, J. M. Reifsnider, B. Yang, C. Collins, A. L. Holmes Jr., and J. C. Campbell, *IEEE J. Quantum Electron.*, vol. 36, pp. 1262, 2000.

[34] D. Walker, E. Monroy, P. Kung, J. Wu, M. Hamilton, F. J. Sanchez, J. Diaz, and M. Razeghi, *Appl. Phys. Lett.*, vol. 74, pp. 762, 1999.

[35] J. C. Carrano, T. Li, P. A. Grudowski, C. J. Eiting, R. D. Dupuis, and J. C. Campbell, *J. Appl. Phys.*, vol. 83, pp. 6148, 1998.

[36] J. C. Carrano, T. Li, D. L. Brown, P. A. Grudowski, C. J. Eiting, R. D. Dupuis, and J. C. Campbell, *Appl. Phys. Lett.*, vol. 73, pp. 2405, 1998.

[37] J. C. Carrano, T. Li, P. A. Grudowski, C. J. Eiting, R. D. Dupuis, and J. C. Campbell, *Appl. Phys. Lett.*, vol. 72, pp. 542, 1998.

[38] J. C. Carrano, T. Li, P. A. Grudowski, C. J. Eiting, D. Lambert, J. D. Schaub, R. D. Dupuis, and J. C. Campbell, *Electron. Lett.*, vol. 34, pp. 692, 1998.

[39] J. C. Carrano, P. A. Grudowski, C. J. Eiting, R. D. Dupuis, and J. C. Campbell, *Appl. Phys. Lett.*, vol. 70, pp. 1992, 1997.

[40] J. C. Carrano, T. Li, P. A. Grudowski, C. J. Eiting, R. D. Dupuis, and J. C. Campbell, *Electron. Lett.*, vol. 33, pp. 1980, 1997.

[41] T. Li, S. Wang, A. L. Beck, C. J. Collins, B. Yang, R. D. Dupuis, J. C. Carrano, M. J. Schurman, I. T. Ferguson, and J. C. Campbell, *Proc. SPIE*, vol. 3948, pp. 304, 2000.

[42] T. Li, J. C. Carrano, M. Schurman, I. Ferguson, and J. C. Campbell, *IEEE J. Quantum Electron.*, vol. 35, pp. 1203, 1999.

[43] D. Walker, A. Saxler, P. Kung, X. Zhang, M. Hamilton, J. Diaz, and M. Razeghi, *Appl. Phys. Lett.*, vol. 72, pp. 3303, 1998.

[44] J. C. Carrano, T. Li, D. L. Brown, P. A. Grudowski, C. J. Eiting, R. D. Dupuis, and J. C. Campbell, *Electron. Lett.*, vol. 34, pp. 1779, 1998.

[45] A. Osinsky, S. Gangopadhyay, R. Gaska, B. Williams, M. A. Khan, D. Kuksenkov, and H. Temkin, *Appl. Phys. Lett.*, vol. 71, pp. 2334, 1997.

[46] J. M. Van Hove, R. Hickman, J. J. Klaassen, P. P. Chow, and P. P. Ruden, *Appl. Phys. Lett.*, vol. 70, pp. 2282, 1997.

[47] G. Y. Xu, A. Salvador, W. Kim, Z. Fan, C. Lu, H. Tang, H. Morkoc, G. Smith, M. Estes, B. Goldenberg, W. Yang, and S. Krishnankutty, *Appl. Phys. Lett.*, vol. 71, pp. 2154, 1997.

[48] D. V. Kuksenkov, H. Temkin, A. Osinsky, R. Gaska, and M. A. Khan, *J. Appl. Phys.*, vol. 83, pp. 742, 1998.

[49] Q. Chen, M. A. Khan, C. J. Sun, and J. W. Yang, *Electron. Lett.*, vol. 31, pp. 1781, 1995.

[50] V. V. Kuryatkov, H. Temkin, J. C. Campbell, and R. D. Dupuis, *Appl. Phys. Lett.*, vol. 78, pp. 3340, 2001.

[51] D. V. Kuksenkov, H. Temkin, A. Osinsky, R. Gaska, and M. A. Kan, *J. Appl. Phys.*, vol. 83, pp. 2142, 1998.

[52] W. Yang, T. Nohova, S. Krishnankutty, R. Torreano, S. McPherson, and H. Marsh, *Appl. Phys. Lett.*, vol. 73, pp. 1086, 1998.

[53] B. Yang, K. Heng, T. Li, C. J. Collins, S. Wang, R. D. Dupuis, J. C. Campbell, M. J. Schurman, and I. T. Ferguson, *IEEE J. Quantum Electron.*, vol. 36 , pp. 1229 , 2000.

[54] J. D. Brown, Z. Yu, J. Matthews, S. Harney, J. Boney, J. F. Schetzina, J. D. Benson, K. W. Dang, C. Terill, T. Nohava, W. Yang, and S. Krishnankutty, *MRS Internet J. Nitride Semicond. Res.*, vol. 4 (9), 1999.

[55] K. A. McIntosh, R. J. Molnar, L. J. Mahoney, K. M. Molvar, N. Efremow Jr., and S. Verghese, *Appl. Phys. Lett.*, vol. 76, pp. 3938, 2000.

[56] B. Yang, T. Li, K. Heng, C. J. Collins, S. Wang, J. C. Carrano, R. D. Dupuis, J. C. Campbell, M. J. Schurman, and I. T. Ferguson, *IEEE J. Quantum Electron.*, vol. , pp. , 2000.

[57] J. C. Carrano, D. J. H. Lambert, C. J. Eiting, C. J. Collins, T. Li, S. Wang, B. Yang, A. L. Beck, R. D. Dupuis, and J. C. Campbell, *Appl. Phys. Lett.*, vol. 76, pp. 924, 2000.

[58] K. A. McIntosh, R. J. Molnar, L. J. Mahoney, A. Lightfoot, M. W. Geis, K. M. Molvar, I. Melngailis, R. L. Aggarwal, W. D. Goodhue, S. S. Choi, D. L. Spears, and S. Verghese, *Appl. Phys. Lett.*, vol. 75, pp. 3485, 1999.

[59] W. Goetz, S. Kern, and J. Rosner, unpublished data.

[60] I. Akasaki, H. Amano, M. Kito, and Hiramatsu, *J. Lumin.*, vol. 48, pp. 666, 1991.

[61] S. Nakamura, T. Mukai, M. Senoh, N. Iwasa, *Jpn. J. Appl. Phys.*, vol. 31, pp. L139, 1992.

[62] S. Nakamura, *Jap. J. Appl. Phys.*, vol. 30, pp. L1705, 1991.

[63] J. F. Chen, N. C. Chen, W. Y. Huang, W. I. Lee, and M. S. Feng, *Jap. J. Appl. Phys.*, vol. 35, pp. L810, 1996.

[64] S. J. Cai, R. Li, Y. L. Chen, L. Wong, W. G. Wu, S. G. Thomas, and K. L. Wang, Electron. Lett., vol. 34, pp. 2354, 1998.

[65] B. P. Luther, J. M. DeLucca, S. E. Mohney, and R. F. Karlicek Jr., *Appl. Phys. Lett.*, vol. 71, pp. 3859, 1997.

[66] E. F. Chor, D. Zhang, H. Gong, G. L. Chen, and T. Y. F. Liew, *J. Appl. Phys.*, vol. 90, pp. 1242, 2001.

[67] S. Ruvimov, Z. Liliental-Weber, J. Washburn, K. J. Duxstad, E. E. Haller, Z. F. Fan, S. N. Mohammad, W. Kim, A. E. Botcharev, and H. Morkoc, *Appl. Phys. Lett.*, vol. 69, pp. 1556, 1996.

[68] K. Kumakura, T. Makimoto, and N. Kobayashi, *Appl. Phys. Lett.*, vol. 79, pp. 2588, 2001.

[69] C. C. Kim, J. K. Kim, J. L. Lee, J. H. Je, M. S. Yi, D. Y. Noh, Y. Hwu, and P. Ruterana, *Appl. Phys. Lett.*, vol. 78, pp. 3773, 2001.

[70] J. K. Kim, J. L. Lee, J. W. Lee, H. E. Shin, Y. J. Park, and T. Kim, *Appl. Phys. Lett.*, vol. 73, pp. 2953, 1998.

[71] C. F. Chu, C. C. Yu, Y. K. Wang, J. Y. Tsai, F. I. Lai, and S. C. Wang, *Appl. Phys. Lett.*, vol. 77, pp. 3423, 2000.

[72] H. W. Jang, K. H. Kim, J. K. Kim, S. W. Hwang, J. J. Yang, K. J. Lee, S. J. Son, and J. L. Lee, *Appl. Phys. Lett.*, vol. 79, pp. 1822, 2001.

[73] M. R. Park, W. A. Anderson, and S. J. Park, *MRS Internet J. Nitride Semicond. Res.*, F99W11.77, 1999.

[74] S. S. Cohen and G. S. Gildenblat, *VLSI Electronics Microstructure Science*, vol. 13, pp. 87-133, Academic Press, 1986.

[75] J. J. Kuek, M. A. Wong, T. A. Fisher, B. D. Nener, and D. L. Pulfrey, *IEEE J. Quantum Electron.*, vol. , pp. 407, 1999.

[76] C. J. Collins, T. Li, A. L. Beck, R. D. Dupuis, J. C. Campbell, J. C. Carrano, M. J. Schurman, and I. A. Ferguson, *Appl. Phys. Lett.*, vol. 75, pp. 2138, 1999.

[77] J. Han, M. H. Crawford, R. J. Shul, S. J. Hearne, E. Chason, J. J. Figiel, and M. Banas, *MRS Internet J. Nitride Semicond. Res.*, 4S1, G7.7, 1999.

[78] W. G. Perry, M. B. Bremser, T. Zheleva, K. J. Linthicum, and R. F. Davis, *Thin Solid Films*, vol. 324, pp. 107, 1998.

[79] S. Nakamura, M. Senoh, S. Nagahama, N. Iwasa, T. Yamada, T. Matsushita, H. Kiyoku, Y. Sugimoto, T. Kozaki, H. Umemoto, M. Sano, and K. Chocho, *Appl. Phys. Lett.*, vol. 72, pp. 211, 1998.

[80] J. Qu, J. Li, and G. Zhang, *Solid State Commun.*, vol. 107, pp. 467, 1998.

[81] S. J. Hearne, J. Han, S. R. Lee, J. A. Floro, D. M. Follaedt, E. Chason, and I. S. T. Tsong, *Appl. Phys. Lett.*, vol. 76, pp. 1534, 2000.

[82] S. Einfeldt, K. Vogeler, V. Kirchner, T. Boettcher, H. Heinke, D. Hommel, D. Rudloff, and J. Christen, *41st Electronic Materials Conference*, Santa Barbara, CA, 1999.

[83] D. Marx, Z. Kawazu, T. Nakayama, Y. Mihashi, T. Takami, M. Nunoshita, and T. Ozeki, *J. Cryst. Growth*, vol. 189, pp. 87, 1998.

[84] C. J. Collins, T. Li, D. J. H. Lambert, M. M. Wong, R. D. Dupuis, and J. C. Campbell, *Appl. Phys. Lett.*, vol. 77, pp. 2810, 2000.

[85] W. I. Park, G. C. Yi, and H. M. Jang, *Appl. Phys. Lett.*, vol. 79, pp. 2022, 2001.

[86] J. F. Muth, C. W. Teng, A. K. Sharma, A. Kvit, R. M. Kolbas, and J. Narayan, *Mat. Res. Soc. Symp.*, vol. 617, J6.7.1, 2000.

[87] C. W. Teng, J. F. Muth, U. Ozgur, M. J. Bergmann, H. O. Everitt, A. K. Sharma, C. Jin, and J. Narayan, *Appl. Phys. Lett.*, vol. 76, pp. 979, 2000.

[88] J. A. Majewski, M. Stadele, and P. Volg, *III-V Nitrides Symposium Mater. Res. Soc.*, pp. 887, 1997.

[89] W. Franz, *Z. Naturforschg.*, vol. 13 a, pp. 484, 1958.

[90] L. V. Keldysh, *Soviet Phys. JETP*, vol. 34, pp. 788, 1958.

[91] K. Noba and Y. Kayanuma, *Phys. Rev. B*, vol. 60, pp. 4418, 1999.

[92] F. Urbach, *Phys. Rev.*, vol. 92, pp. 1324, 1953.

[93] T. Li, D. J. H. Lambert, M. M. Wong, C. J. Collins, B. Yang, A. L. Beck, U. Chowdhury, R. D. Dupuis, and J. C. Campbell, *IEEE J. Quantum Electron.*, vol. 37 , pp. 538 , 2001.

[94] E. J. Tarsa, P. Kozodoy, J. Ibbetson, B. P. Keller, G> Parish, and U. Mishra, *Appl. Phys. Lett.*, vol. 77, pp. 316, 2000.

[95] D. J. H. Lambert, M. M. Wong, U. Chowdhury, C. J. Collins, T. Li, H. K. Kwon, B. S. Shelton, T. G. Zhu, J. C. Campbell, and R. D. Dupuis, *Appl. Phys. Lett.*, vol. 77, pp. 1900, 2000.

[96] S. M. Sze, *Physics of Semiconductor Devices*, John Wiley & Sons Inc., New York, 1981.

[97] P. Bhattacharya, *Semiconductor Optoelectronic Devices*, Prentice-Hall Inc., New Jersey, 1997.

[98] B. G. Streetman, *Solid State Electronic Devices*, Prentice-Hall Inc., New Jersey, 1995.

[99] T. Asano, M. Takeya, T. Tojyo, T. Mizuno, S. Ikeda, K. Shibuya, T. Hino, S. Uchida, and M. Ikeda, *Appl. Phys. Lett.*, vol. 80, pp. 3497, 2002.

[100] M. Diagne, Y. He, H. Zhou, E. Makarona, A. V. Nurmikko, J. Han, K. E. Waldrip, J. J. Figiel, T. Takeuchi, and M. Krames, *Appl. Phys. Lett.*, vol. 79, pp. 3720, 2001.

[101] J. J. Wierer, D. A. Steigerwald, M. R. Krames, J. J. O'Shea, M. J. Ludowise, G. Christenson, Y. C. Shen, C. Lowery, P. S. Martin, S. Subramanya, W. Gotz, N. F. Gardner, R. S. Kern, and S. A. Stockman, *Appl. Phys. Lett.*, vol. 78, pp. 3379, 2001.

[102] Y. K. Song, H. Zhou, M. Diagne, I. Ozden, A. Vertikov, A. V. Nurmikko, C. Carter-Coman, R. S. Kern, F. A. Kish, and M. R. Krames, *Appl. Phys. Lett.*, vol. 74, pp. 3441, 1999.

[103] M. M. Wong, J. C. Denyszyn, C. J. Collins, U. Chowdhury, T. G. Zhu, K. S. Kim, and R. D. Dupuis, *Elec. Lett.*, vol. 37, pp. 1188, 2001.

[104] D. Walker, V. Kumar, K. Mi, P. Sandvik, P. Kung, X. H. Zhang, and M. Razeghi, *Appl. Phys. Lett.*, vol. 76, pp. 403, 2000.

[105] G. Parish, S. Keller, P. Kozodoy, J. P. Ibbetson, H. Marchand, P.T. Fini, S. B. Fleicher, S. P. DenBaars, U. K. Mishra and E. J. Tarsa, *Appl. Phys. Lett.*, vol. 75, pp. 247, 1999.

[106] C. Pernot, A. Hirano, M. Iwaya, T. Detchprohm, H. Amano, and I. Akasaki, *Jpn. J. Appl. Phys. Part 2*, vol 39, ppL387, 2000.

[107] P. Sandvik, K. Mi, F. Shahedipour, R. McClintock, A. Yasan, P. Kung, M. Razeghi, J. Cryst. Grow., vol. 231, pp. 366, 2001.

[108] G. Parish, M. Hansen, B. Moran, S. Keller, S. P. DenBaars, and U. K. Mishra, Phys. Stat. Sol., vol. 188, pp. 297, 2001.

[109] J. C. Campbell, C. J. Collins, M. M. Wong, U. Chowdhury, A. L. Beck, and R. D. Dupuis, *Phys. Sat. Sol. a*, vol. 188, pp. 283, 2001.

[110] M. A. Khan, R. A. Skogman, R. G. Schulze, and M. Gershenzon, *Appl. Phys. Lett.*, vol. 43, pp. 492, 1983.

[111] H. G. Lee, M. Gerhenzon, and B. L. Goldenberg, *J. Electron. Mater.*, vol. 20, pp. 621, 1991.

[112] M. D. Bremser, W, G, Perry, T. Zheleva, N. V. Edwards, O. H. Nam, N. Parikh, D. E. Aspnes, and R. F. Davis, *MRS Internet J. Nitride Semicond. Res.*, vol.1, pp. 8, 1996.

[113] V. Adivarahan, G. Simin, G. Tamulaitis, R. Srinivasan, J. Yang, M. Asif Khan, M. S. Shur, and R. Gaska, *Appl. Phys. Lett.*, vol. 79, pp. 1903, 2001.

[114] I. Yonenaga, and K. Sumino, *J. Appl. Phys.*, vol. 62, pp. 1212, 1987.

[115] C. Stampfl, and C. G. Van de Walle, *Appl. Phys. Lett.*, vol. 72, pp. 495, 1998.

[116] C. G. Van de Walle, *Phys. Rev. B*, vol. 57, pp. R2033, 1998.

[117] S. B. Zhang, S. H. Wei, and A. Zunger, *Phys. Rev. Lett.*, vol. 84, pp. 1232, 2000.

[118] C. H. Park and D. J. Chadi, *Phys. Rev. B*, vol. 55, pp. 12995, 1997.

[119] C. Skierbiszewski, T. Suski, M Leszczynski, M. Shin, M. Skowronski, M. D. Bremser, and R. F. Davis, *Appl. Phys. Lett.*, vol. 74, pp. 3833, 1999.

[120] J. Li, K. B. Nam, J. Y. Lin, and H. X. Jiang, *Appl. Phys. Lett.*, vol. 79, pp. 3245, 2001.

[121] C. J. Collins, U. Chowdhury, M. M. Wong, B. Yang, A. L. Beck, R. D. Dupuis, and J. C. Campbell, *Appl. Phys. Lett.*, vol. , pp. , 2002.

[122] C. J. Collins, U. Chowdhury, M. M. Wong, B. Yang, A. L. Beck, R. D. Dupuis, and J. C. Campbell, submitted to *Elec. Lett.*, 2002.

[123] U. Chowdhury, M. M. Wong, C. J. Collins, B. Yang, J. C. Denyszyn, J. C. Campbell, and R. D. Dupuis, *submitted to J. Cryst. Grow.*, 2002.

Vita

Charles Joseph Collins was born in Anaheim, California on April 7, 1979, the first child of Gary James Collins and Carol Jean Collins. After graduating in 1994 from McCullough High School in The Woodlands, Texas, he attendend Trinity University in San Antonio, Texas and majored in Engineering. After receiving his B.S. degree in Engineering Science in 1998, he attended graduate school at the University of Texas at Austin. In December of 2001 he received his Master of Science in Electrical Engineering.

Permanent address: 8 Dewthread Ct., The Woodlands, Texas, 77380
This dissertation was typed by Charles Joseph Collins.